Flow Synthesis of Silver Nanowires

Thomas William Phillips

Submitted for the degree of Doctor of Philosophy

Department of Physics
Imperial College London

September 2016

Abstract

This thesis reports the development of a droplet-based flow synthesis of silver nanowires. Using traditional batch methods of production it can be difficult to achieve the consistent reaction conditions needed to obtain nanocrystals with the desired properties. Microfluidic reactors offer superior control over reaction conditions and enable the scalable and continuous production of consistent and monodisperse nanoparticles. Silver nanowires are typically synthesised using the polyol reaction, where silver nitrate is reduced in hot ethylene glycol. Previous reports describing the synthesis of silver nanowires have come to contradictory conclusions about the conditions needed for growth. In this thesis a hot-injection polyol synthesis was adapted to a straightforward heat-up procedure for the production of silver nanowires. The success of the reaction was found to be dependent on the batch of ethylene glycol used. The modified synthesis enabled the development of a flow process using a polytetrafluoroethylene tubing-based droplet-based flow reactor. The reactor produced consistent silver nanowires over an eight hour period with no sign of reactor fouling. The reactor was used to investigate the effect of varying the reaction temperature, residence time, and concentration of iron nitrate and sodium chloride additives on the length of the silver nanowires produced.

This thesis finishes with the development of an inline liquid-liquid separator based on the selective wetting and permeation of a porous capillary by one of the liquids. Efficient separation of aqueous-organic, aqueous-fluorous, and organic-fluorous flows was achieved over a wide range of flow rates. The separator was successfully applied to the inline aqueous-organic extraction of the pH indicator 2,6-dichloroindophenol. The organic extract and aqueous raffinate were separated using a porous capillary. UV-visible absorption spectroscopy showed the concentration of indicator in the aqueous raffinate to be less than one percent of its original value, confirming the efficacy of the extraction and separation process.

Declaration of Originality

Except where specific reference is made, the contents of this thesis is my own work.

Thomas William Phillips

Copyright Declaration

The copyright of this thesis rests with the author and is made available under a Creative Commons Attribution Non-Commercial No Derivatives licence. Researchers are free to copy, distribute or transmit the thesis on the condition that they attribute it, that they do not use it for commercial purposes and that they do not alter, transform or build upon it. For any reuse or redistribution, researchers must make clear to others the licence terms of this work.

Contents

Acknowledgements **9**

List of Publications **10**

List of Figures **12**

List of Tables **19**

Abbreviations **21**

1 Nanocrystal Synthesis in Microfluidic Reactors **23**

1.1 Note . . . 23
1.2 Introduction . . . 23
1.3 Microreactor types and flow regimes . . . 28
1.4 Inline analysis and optimisation . . . 36
1.5 Large scale production . . . 36
1.6 Beyond batch techniques . . . 41
1.7 Summary . . . 43

2 Introduction to Silver Nanowire Synthesis **44**

2.1 Polyol synthesis . . . 44
2.2 Growth mechanism . . . 47
2.3 Ionic additives . . . 53
2.3.1 Fe-mediated method . . . 53
2.3.2 $CuCl_2$-mediated method . . . 55
2.4 Other batch routes . . . 56

2.5 Continuous flow routes 61
2.6 Challenges 63
2.6.1 Contaminants in ethylene glycol 63
2.6.2 Glycolaldehyde as a reducing agent 64
2.6.3 Nanowire purification 65
2.7 Summary 65

3 Batch Synthesis of Silver Nanowires 67
3.1 Introduction 67
3.2 Heat-up versus hot-injection 70
3.2.1 Analysis using dark field optical microscopy 71
3.2.2 Temperature profile comparison 76
3.2.3 Conclusions 76
3.3 Irreproducibility of batch synthesis 77
3.3.1 Pipetting errors 80
3.3.2 Minimisation of pipetting errors 81
3.3.3 Testing the modified method 84
3.3.4 Effect of ethylene glycol lot number 86
3.3.5 Electron microscopy analysis 89
3.3.6 Losses due to washing 94
3.4 Chemical analysis of ethylene glycol 96
3.5 Conclusions & further work 99

4 Flow Synthesis of Silver Nanowires 102
4.1 Introduction 102
4.2 Preliminary tests 102
4.3 Dual-precursor flow reactor 104
4.4 Stability testing 112
4.5 Effect of varying reaction temperature and residence time . . . 116
4.6 Varying concentration of ionic additives 120
4.6.1 Sodium chloride 120
4.6.2 Iron nitrate 126
4.6.3 Ionic species in ethylene glycol 128

4.7 Conclusions . . . 130
4.8 Further work . . . 131
4.8.1 Other reaction parameters . . . 131
4.8.2 Extinction spectra and inline analysis . . . 132
4.8.3 Adsorption of AgNWs at the EG-PFPE interface . . . 133
4.8.4 Multiple temperature zone flow reactor . . . 134

5 Experimental Methods 136
5.1 Reagents and materials . . . 136
5.2 Batch syntheses . . . 136
5.2.1 General procedures . . . 136
5.2.2 Comparison of heat-up and hot-injection methods . . . 136
5.2.3 Modified heat-up method . . . 137
5.3 Flow syntheses . . . 138
5.3.1 General procedures . . . 138
5.3.2 Three-in-one-out junction . . . 138
5.3.3 Single-precursor preparation . . . 139
5.3.4 Dual-precursor preparation . . . 139
5.3.5 Stability testing . . . 140
5.3.6 Varying concentration of ionic additives . . . 140
5.4 Techniques . . . 141
5.4.1 Forward and reverse pipetting . . . 141
5.4.2 Washing of crude samples . . . 141
5.4.3 Dark field optical microscopy . . . 142
5.4.4 Scanning electron microscopy . . . 144
5.4.5 Nuclear magnetic resonance spectroscopy . . . 144
5.4.6 UV-visible spectroscopy . . . 145

6 Microscale Extraction and Phase Separation Using a Porous Capillary 146
6.1 Note . . . 146
6.2 Introduction . . . 146
6.2.1 Gravity-based separators . . . 147

6.2.2 Wetting-based separators . . . 149
6.3 Development of a versatile liquid–liquid separator . . . 162
6.4 Results and Discussion . . . 164
6.4.1 Operating principle . . . 164
6.4.2 Inline liquid–liquid separation . . . 167
6.4.3 Inline liquid–liquid extraction . . . 174
6.5 Conclusions . . . 176
6.6 Experimental Methods . . . 177
6.6.1 Two-in-one-out junction . . . 177
6.6.2 Fabrication of separator . . . 178
6.6.3 Testing of separator . . . 178
6.6.4 Inline extraction . . . 179
6.6.5 Scanning electron microscopy . . . 180

Bibliography **181**

A Silver nanowires **191**
A.1 Box and whisker plots . . . 191
A.2 Certificates of analysis for ethylene glycol . . . 193
A.3 COSY NMR . . . 198

B Reproduction permissions **200**

Acknowledgements

First and foremost I would like to thank Professor John de Mello. It has been a privilege to carry out research under his supervision. I am tremendously grateful for all of his time, guidance, and interest in my work, and for so many opportunities over the last four years.

Several people made the experiments in this thesis possible. Simon Turner built essential pieces of laboratory apparatus and was always willing to help me get out of a pickle in the lab. Lee Tooley made droplet generators and Stephen Atkins helped with electronics. I am thankful to all three of them for their expertise.

My PhD would not have been anywhere near as productive or fun without the de Mello group. A huge thank you to James Bannock for so many helpful discussions and ideas. I hope we get to work together again. Thank you to Adrian Nightingale, who showed me how to make my first batch of nanoparticles back in 2010 and from whom I learned so much in the laboratory, and also to Siva Krishnadasan for his help tinkering with kit. It has been a pleasure to work with Barnaby Walker, Kirsty Roy, and Wenmin Xu and I want to thank them for their help and friendship.

I thank my parents for all their encouragement over the years. Finally, thank you to Kelly Oakes for everything. Now that my thesis is finished I can't wait for our adventures together.

List of Publications

First author

Microscale extraction and phase separation using a porous capillary
T. W. Phillips, J. H. Bannock and J. C. de Mello, *Lab on a Chip*, 2015, **15**, 2960–2967. DOI: 10.1039/C5LC00430F

Nanocrystal synthesis in microfluidic reactors: where next?
T. W. Phillips, I. G. Lignos, R. M. Maceiczyk, A. J. de Mello and J. C. de Mello, *Lab on a Chip*, 2014, **14**, 3172–3180. DOI: 10.1039/C4LC00429A

New Materials for Transparent Conducting Electrodes
T. W. Phillips and J. C. de Mello (eds. F. Cicoira and C. Santato), in *Organic Electronics: Emerging Concepts and Technologies*, Wiley, 2013. DOI: 10.1002/9783527650965.ch06

Contributing author

Photostable phosphorescent polymer nanospheres for high sensitivity detection
A. N. Edwards, M. Yamazaki, S. H. Krishnadasan, T. W. Phillips, L. Rowlands, R. Jourdain, A. M. Nightingale and J. C. de Mello, *Journal of Materials Chemistry C*, 2015, **3**, 6565–6572. DOI: 10.1039/C5TC00933B

Controlled multistep synthesis in a three-phase droplet reactor
A. M. Nightingale, T. W. Phillips, J. H. Bannock and J. C. de Mello, *Nature Communications*, 2014, **5**, 3777. DOI: 10.1038/ncomms4777

Microscale separation of immiscible liquids using a porous capillary
J. H. Bannock, T. W. Phillips, A. M. Nightingale and J. C. de Mello, *Analytical Methods*, 2013, **5**, 4991–4998. DOI: 10.1039/C3AY41251B

List of Figures

1.1 Cartoon showing solute concentration against time during nucleation and growth of nanoparticles 24
1.2 Cartoon illustrating laminar and turbulent flow in a channel . 26
1.3 SEM image of the micromixer chip used by Edel *et al.* for the microscale synthesis of CdS nanocrystals 27
1.4 Photograph of a simple glass "two-in-one-out" microfluidic chip for nanocrystal synthesis 29
1.5 Diagram showing three types of fluid flow in a microfluidic channel 30
1.6 Photograph of a blocked two-in-one-out glass chip used for InP nanocrystal synthesis 31
1.7 Micrographs of microfluidic chips used by Shestopolov *et al.* for continuous and segmented flow synthesis of CdS nanocrystals 33
1.8 Emission spectra of CdSe nanocrystals produced by Nightingale *et al.* using a droplet-based capillary reactor 34
1.9 Photograph showing the early stages of titania synthesis in the droplet reactor developed by Nightingale *et al.* 35
1.10 Schematic of a microfluidic system developed by Toyota *et al.* for the rapid combinatorial synthesis CdSe quantum dots . . . 37
1.11 Schematic of microfluidic reactors to illustrate the concept of scale out 38
1.12 Schematic of a scaled-out five-channel droplet flow reactor developed by Nightingale *et al.* 40

1.13 Diagram of the high-pressure, high-temperature microreactor developed by Marre, Park *et al.* 42

2.1 Chemical structure of polyvinylpyrrolidone 45
2.2 TEM and SEM images of four crude samples of Ag nanoparticles and nanowires synthesised by Sun *et al.* 46
2.3 Schematic of the mechanism proposed by Sun *et al.* for the growth of AgNWs 48
2.4 Diagram showing a plan view of the close-packed layers in a hcp and fcc crystal structure 50
2.5 Diagrams illustrating the stacking sequence in a fcc crystal, a hcp crystal, and a twin defect 50
2.6 Drawing of a decahedral seed and a five-fold twinned nanoparticle 51
2.7 SEM image of AgNWs that have been broken using sonication 52
2.8 TEM and SEM images of nanoparticles and AgNWs produced using the Fe-mediated method 54
2.9 Illustration of the mechanism by which Fe^{2+} removes atomic oxygen from the surface of Ag nanostructures 55
2.10 TEM images of Ag seeds produced using the $CuCl_2$-mediated method 57
2.11 Graph showing the effect of reaction time and temperature on the length of AgNWs produced by Bergin *et al.* 59
2.12 SEM images of products obtained by Lim *et al.* using the heat-up and hot-injection method 60
2.13 Schematic of the reactor used by Gottesman *et al.* for the continuous flow synthesis of AgNWs 61
2.14 Schematic of the continuous flow glass millifluidic reactor used by Chou *et al.* to synthesis AgNWs 62

3.1 Schematic of a hypothetical flow reactor that closely follows the batch synthesis of AgNWs described by Bergin *et al.* . . . 68
3.2 Schematic of a simple flow reactor for AgNW synthesis where the reagents are combined into single reaction mixture 69

3.3 DFOM images of samples removed from the hot-injection and heat-up reactions 72
3.4 Histograms showing the frequency of AgNW lengths measured from the DFOM images of samples removed from the hot-injection and heat-up reactions 74
3.5 Graph showing the temperature of the reaction mixtures over time for the hot-injection and heat-up methods 75
3.6 DFOM images of samples taken at $t = 15$ min from two repeats of the hot-injection and heat-up syntheses 77
3.7 Cause-and-effect diagram showing factors that might affect the product of the AgNW synthesis 79
3.8 Box and whisker plots of the lengths of AgNWs removed from repeat heat-up reactions 84
3.9 DFOM images of samples removed at $t = 20$ min from reactions (a) and (f) 85
3.10 Box and whisker plots showing the length of AgNWs removed from the reaction mixture at $t = 13$ min, 16 min, and 20 min for reactions (g–j) 88
3.11 Box and whisker plots showing the length of AgNWs measured in the sample removed at $t = 20$ min from reactions (a–j), grouped by lot A and lot B. 88
3.12 Photograph of a vial of AgNWs dispersed in water 89
3.13 SEM images of samples of AgNWs grown in EG from lot A and lot B 91
3.14 DFOM images of washed AgNWs from lot A and lot B 92
3.15 Histograms showing the diameter of AgNWs synthesised in EG from lot A and lot B 92
3.16 Histograms showing the lengths of washed AgNWs synthesised in EG from lot A and lot B 93
3.17 Histograms showing the length of AgNWs measured using DFOM for crude and washed samples synthesised in EG from lot A and lot B 95
3.18 ^{1}H NMR spectra of EG from lot A and lot B 97

3.19 Chemical structure of diethylene glycol and triethylene glycol . 98

4.1 Schematic of the reactor used for the first attempt at synthesising AgNWs in flow 103
4.2 Photograph of a PFPE-EG segmented flow from the outlet of the Y-mixer 104
4.3 Schematic of the dual-precursor flow reactor for producing AgNWs in flow 105
4.4 Photograph of a three-in-one-out junction 106
4.5 Photograph of the metal frame used to mount the reactor tubing in a horizontal plane 107
4.6 Photograph of the typical dual-precursor reactor configuration 109
4.7 DFOM images of samples produced in flow 110
4.8 Box and whisker plots showing the length of 30 AgNWs for residence times of 13 min, 16 min, and 20 min 111
4.9 Schematic of the flow reactor used to assess the consistency of the product during operation 113
4.10 Photograph of the segmented flow after it exited the oil bath . 114
4.11 Box and whisker and scatter plots showing the length of AgNWs over 8 h continuous operation 115
4.12 DFOM images of product from the first and last fractions produced during the stability testing of the reactor. 116
4.13 Graphs showing AgNW length against residence time for temperatures between 150 °C and 170 °C 117
4.14 DFOM images of AgNWs produced at $T = 165\,°C$ and $t_R = 13\,min$ and $T = 170\,°C$ and $t_R = 25\,min$ 119
4.15 Schematic of the reactor used to vary the concentration of NaCl in the droplets 121
4.16 Graph showing the median AgNW length versus the concentration of NaCl after the three-in-one-out junction 123
4.17 DFOM images of samples produced using different concentrations of NaCl 125

4.18 Schematic of the reactor used to vary the concentration of $Fe(NO_3)_3$ in the droplets 126
4.19 Box and whisker plots showing the length of AgNWs produced at $Fe(NO_3)_3$ concentrations from 0 to 20 µM 128
4.20 DFOM images of samples produced using different concentrations of $Fe(NO_3)_3$, from 0 to 20.1 µM 129
4.21 Normalised extinction spectra of crude samples produced at 150 °C and 165 °C using residence times from 13 to 25 min . . 133
4.22 Schematic of the continuous flow reactor used for preliminary investigation into the effect of multiple temperature zones . . . 134
4.23 SEM images of product obtained from constant and progressively increasing temperatures across four consecutive oil baths 135

5.1 Diagram showing the cross-section of the three-in-one-out junction 139
5.2 Diagram showing the position of the pipette plunger when dispensing liquids using the forward and reverse pipetting techniques 142
5.3 Diagrams showing the light path through an optical microscope in bright field and dark field modes 143
5.4 Graph showing the mean and median length for 1 to 60 AgNW measurements 145

6.1 Schematic of a flow reactor developed by O'Brien *et al.* for the synthesis of hydrazones, incorporating a gravity-based liquid-liquid separator 148
6.2 Schematic showing an improved gravity-based liquid-liquid separator developed by Hu *et al.* for the continuous aqueous diazotization of amino acids and subsequent sequential liquid–liquid extraction of the α-hydroxyacid product into ethyl acetate . . 150
6.3 Photograph and schematic of a wetting-based separator developed by Kashid *et al.* 151
6.4 Schematic and photograph of a plate-type separator developed by Kolehmainen *et al.* 152

6.5 Schematic of a phase separator developed by Scheiff *et al.* . . 153
6.6 Diagram of the liquid-gas (air) interface for a wetting and a non-wetting liquid in a cylindrical capillary channel of radius r 154
6.7 Cross-sectional view of the slit-based separator developed by Gaakeer *et al.* 156
6.8 Schematic and cartoon of the microfluidic chip channel layout of the separator developed by Castell *et al.* 157
6.9 Schematic of the membrane separator developed by Nord and Karlberg 159
6.10 Schematic and photograph of the standalone separator developed by Kralj *et al.* 161
6.11 Drawing of the phase separator developed by Yamamoto *et al.* 163
6.12 Cartoon showing operation of the separator 165
6.13 SEM image of the porous PTFE capillary 166
6.14 Schematic of the separator in use 168
6.15 Graphs showing the volumetric collection rate at the outlet versus volumetric injection rate of solvent at the inlet for aqueous–fluorous, organic–fluorous, and aqueous–organic systems 169
6.16 Photographs showing vials containing liquid collected through the separator walls and from the outlet of the separator 170
6.17 Graph showing the volumetric collection rate at the outlet versus the volumetric injection rate of solvent at the inlet for organic–fluorous separation using different length flow restrictions 173
6.18 Schematic of experimental set-up used for aqueous–organic extraction followed by inline separation 175
6.19 Photographs and UV-visible absorption spectra of NaA (aq.), HA (aq.), extract HA ($CHCl_3$), and raffinate NaCl (aq.) . . . 176
6.20 Diagram of a two-in-one-out junction machined from PTFE round stock. 177

A.1 Histogram and box and whisker plot showing the probability density function for a normal distribution 192
A.2 COSY NMR spectra of EG from lot A and lot B 199

List of Tables

3.1 Table showing the results of the gravimetric analysis of the pipetting used in the heat-up and hot-injection syntheses . . . 80
3.2 Table concentration of the stock solutions c and corresponding volume V added to the reaction mixture for the original and modified batch procedure. 82
3.3 Table showing the results of the gravimetric analysis of the pipetting used in the modified AgNW synthesis 83
3.4 Table showing for reactions (a–k) the lot number of the EG used to prepare the PVP and $AgNO_3$ solutions and the median length and SD at $t = 20\,\text{min}$. 87
3.5 Table showing the median, mean, and SD of the length of AgNWs measured using SEM and DFOM for washed samples from lot A and lot B 94
3.6 Table showing the concentration of Cl, Cu, and Fe in the EG according to the manufacturer certificates of analysis in Appendix A.2 98

4.1 Flow rates used to vary the residence time t_R for the dual-precursor flow reactor shown in Figure 4.3 108
4.2 Table showing the residence time t_R and flow rates for experiments to investigate the effect of temperature and residence time on the synthesis of AgNWs 118
4.3 Table showing the flow rates for values of P between 0 and 1 and the corresponding concentration of NaCl for two pairs of concentrations of NaCl 122

4.4 Table showing the flow rates for values of P between 0 and 1 and the corresponding concentration of $Fe(NO_3)_3$ 127

Abbreviations

AgNW silver nanowire

CNC computer numerical control

COSY correlation spectroscopy

CV coefficient of variation

DFOM dark field optical microscopy

EG ethylene glycol

fcc face-centred cubic

GA glycolaldehyde

hcp hexagonal close-packed

ID internal diameter

IQR interquartile range

MTP multiply twinned particle

NMR nuclear magnetic resonance

OD outer diameter

PEEK polyether ether ketone

PFPE perfluorinated polyether

PTFE polytetrafluoroethylene

PVP polyvinylpyrrolidone

RBF round-bottomed flask

RCF relative centrifugal force

rpm revolutions per minute

SD standard deviation

SEM scanning electron microscopy

TEM transmission electron microscopy

TFR total flow rate

Chapter 1

Nanocrystal Synthesis in Microfluidic Reactors

1.1 Note

This chapter has been expanded and adapted from the review cited in Ref. 1.

1.2 Introduction

The availability of high quality nanometre-sized colloidal crystals is of critical importance in many fields of applied science, including optoelectronics,[2] catalysis,[3] and nanomedicine.[4] In each of these fields, the size-controlled physical and chemical properties of nanocrystals can be exploited to improve on conventional bulk materials in terms of chemical reactivity, bioavailability, or magnetic, optical, or electronic behaviour. In all cases, this requires tightly specified nanocrystals of well-defined size, shape, composition, and crystallinity.

Since Michael Faraday accidentally prepared gold colloids in the basement of the Royal Institution in 1856—which are remarkably still stable and on display in the Faraday Museum—a multitude of synthetic strategies have been reported for producing high quality nanocrystals.[5] The solution-phase

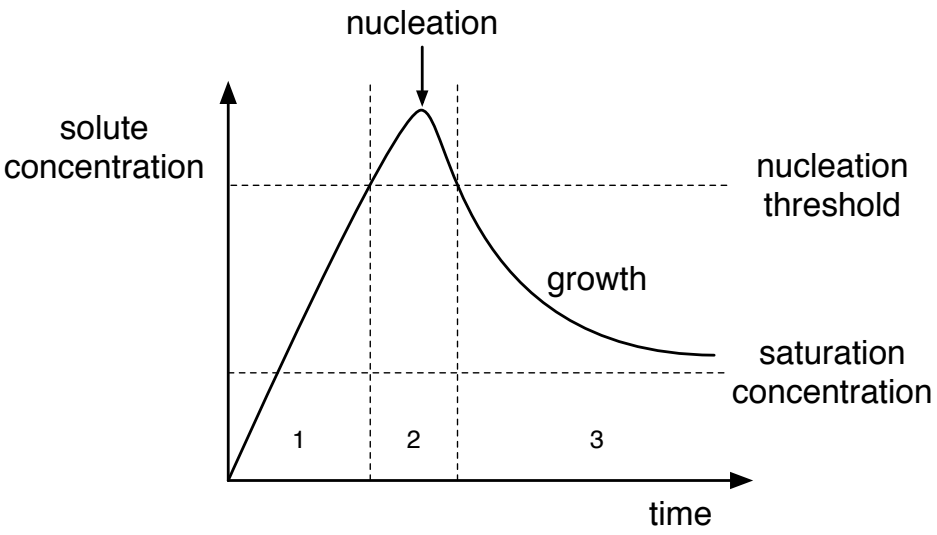


Figure 1.1 – Cartoon showing solute concentration against time during nucleation and growth of nanoparticles. In stage 1, the concentration of solute (produced by a chemical reaction) steadily increases to produce a supersaturated solution. In stage 2, the concentration of solute is high enough for thermal excitation to overcome the energetic barrier to precipitation, leading to a burst of nucleation. In stage 3, nuclei accumulate solute and grow into nanoparticles (and potentially beyond). The concentration drops below the nucleation threshold, stopping nucleation.

synthesis of nanocrystals is typically understood using the nucleation and growth model, which was proposed in 1950 by LaMer and Dinegar to describe the synthesis of sulfur colloids.[6,7] The model consists of three stages, illustrated in Figure 1.1. In the first stage, solute is produced by a chemical reaction. The energy barrier to homogeneous nucleation is initially high, so the solute does not precipitate, but the energy barrier decreases as the solute concentration rises. In the second stage, the concentration is high enough that the solution is supersaturated. The energy barrier to nucleation eventually becomes sufficiently low to be overcome by thermal excitation, leading to a burst of nucleation through the formation of small clusters of atoms. In the third stage, the nuclei accumulate solute and grow to form nanoparticles (or larger crystals). The model assumes that the rate of solute production is less than the rate of consumption by nucleation and growth, and consequently the solute concentration drops below the nucleation threshold, bringing nucleation to a halt. Uninhibited, growth continues until all the solute has been consumed. Nanocrystals are only obtained if growth and aggregation are prevented by electrostatic repulsion (in aqueous systems) or the attachment of stabilising additives such as surfactants, ligands, or polymers to the surface of the nanocrystal.[8,9]

Unfortunately many nanocrystal syntheses suffer from poor reproducibility, require a high level of skill, intuition, and extensive experimentation to achieve high quality size-controlled particles.[10] When syntheses are carried out in traditional laboratory flasks and tanks—*i.e.* when employing *batch processes*—it can be difficult to ensure consistent reaction conditions from one time to the next, especially when reactions are carried out manually. Minor variations in the times and rates of precursor addition can have a strong influence on the product, meaning the quality of the nanocrystals obtained can vary greatly from one batch to the next.[11–13] Furthermore inhomogeneities in the temperature or chemical composition of the reaction mixture due to uneven heating or inadequate mixing can be an unwanted source of polydispersity.[1,14,15]

To address these issues, Edel *et al.* proposed in 2002 the use of microscale reactors as an alternative to traditional batch processes for nanocrystal syn-

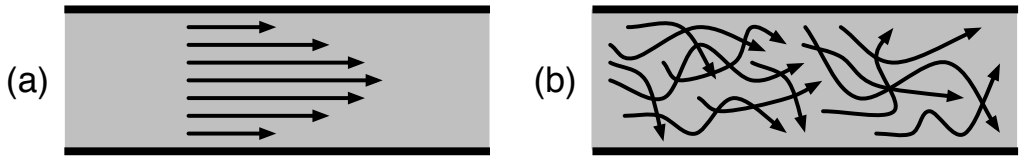


Figure 1.2 – Cartoon illustrating (a) laminar and (b) turbulent flow in a channel. In laminar flow, the fluid flows in orderly layers. In turbulent flow, the fluid flow is disordered.

thesis.[16] In a microscale reactor, the reactant-product mixture is pumped through a narrow channel that is typically 10 to 1000 µm in diameter. Confinement in such a channel has two key effects on the fluid behaviour.[17]

Firstly, fluid flow through a microchannel is dominated by viscous forces (rather than inertial forces), which causes the fluid to flow in orderly layers called laminae. Individual fluid molecules follow paths that rarely cross those of neighbouring molecules. This regime is called *laminar flow* in contrast to chaotic *turbulent flow* that occurs in most natural and engineered systems (Figure 1.2). The Reynolds number is a dimensionless number that quantifies the ratio of inertial to viscous forces in a fluid flow:

$$Re = \frac{\rho V D}{\mu} \tag{1.1}$$

where ρ is the density of the fluid, V is the velocity of the fluid, D is the diameter of the channel, and μ is the dynamic viscosity of the fluid. From observation laminar flow generally occurs at $Re < 2300$, with the flow becoming unstable and turbulent at substantially higher numbers.[18] An important feature of laminar flow is that mixing occurs relatively slowly by diffusion across the layers of fluid for reactions that require fast mixing. Microfluidic devices called micromixers, which use complex channel geometries (passive micromixers) or external fields (active micromixers), are required to mix fluids quickly.[19]

Secondly, the high surface-area-to-volume ratio of microchannels means that heat transfer with the reactor walls is much faster than it is in a macroscale vessel.[20] Therefore exothermic or high temperature (and pres-

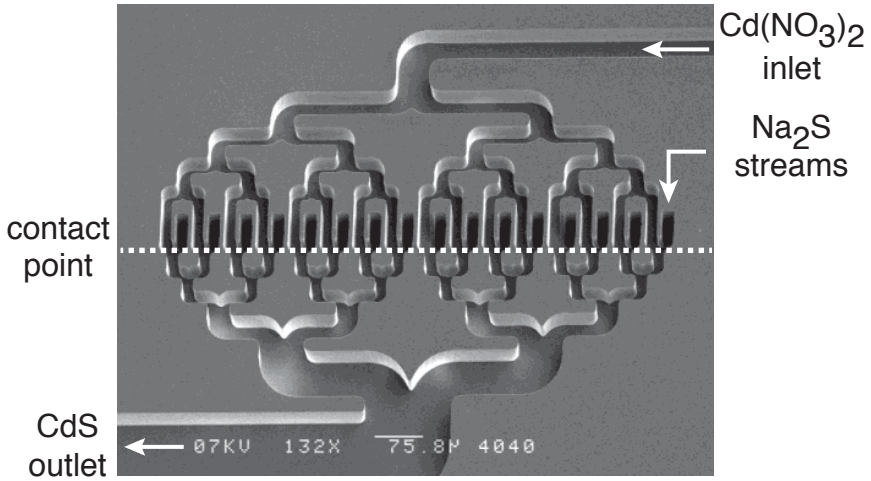


Figure 1.3 – SEM image of the micromixer chip (12 nL volume, top layer shown) used by Edel *et al.* for the microscale synthesis of CdS nanocrystals. Two inlet flows of cadmium nitrate and sodium sulphide solution are split into 16 partial flows and then brought into into contact (marked by the dotted line). After mixing by diffusion the channels are then recombined into one broad outlet channel. Adapted from Ref. 16 with permission of The Royal Society of Chemistry.

sure) reactions can be carried out in a safe, isothermal manner.[21–23]

Edel *et al.* reasoned that controlled mixing and fast heat transfer would ensure better uniformity in the thermal and chemical environment, which in turn would lead to improved product control. In particular, they reasoned that miniaturisation would reduce polydispersity as the nanocrystals would have all grown in the same environment. A simple demonstration of the idea was provided, using the reaction of cadmium nitrate and sodium sulphide (with sodium polyphosphate as a capping agent) to form cadmium sulphide nanocrystals of tuneable band gap. To mix the precursor solutions quickly, the researchers used the passive micromixer shown in Figure 1.3. The two inlet flows were split into a series of 16 streams, which were then brought into contact with one another, where they mix by diffusion, before being recombined into a single outlet stream.

This demonstrated the feasibility of adapting a conventional batch synthesis route to flow, and in particular demonstrated the ease with which

reaction conditions could be systematically varied in a flow environment. However it did not at the time improve upon the quality of nanocrystals achievable in batch. In the ensuing years, there have been numerous reports of nanocrystal syntheses in microfluidic reactors, ranging widely in sophistication and complexity with regards to the microfluidic network employed, the synthetic strategy, and the nature of the particles produced. The rest of this chapter outlines the state-of-the-art in the field.

1.3 Microreactor types and flow regimes

Microreactors for nanocrystal synthesis fall into two broad categories: capillary- and chip-based systems. Capillary reactors are generally simpler in structure and more easily fabricated, using appropriate lengths of tubing connected together using simple fluidic components. Chips are typically fabricated from a plastic, glass or silicon substrate, using soft-lithography, wet etching or micromachining techniques, and can be precisely tailored to the individual requirements of the reaction; multiple chemical processes (e.g. heating, mixing, cooling, reagent addition) can be integrated into a single, small-footprint device.[24] Figure 1.4 is a photograph of a simple glass "two-in-one-out" microfluidic chip. It features two inlets and one outlet joined by a Y-junction, and a long serpentine channel along which a reaction takes place. Both types of reactor have been applied to good effect in nanocrystal synthesis.[25–29]

On a different level, microfluidic reactors can be categorised as single-phase and two-phase reactors.[31] (Three-phase reactors have also been reported but are less common).[32–35] Most research to date has focused on single-phase reactors, in which miscible streams of reagents are injected into a channel or capillary where they mix and react (Figure 1.5 (a)). Single-phase reactors offer a high degree of synthetic flexibility, tolerating a wide range of flow rates and solvents. In addition, they facilitate the easy injection of additional reagents in a controlled manner through the use of downstream inlets along the reaction channel, making it straightforward to conduct multistep reactions and produce more complex structures.[36]

Two issues, however, limit the performance of single-phase reactors. Firstly,

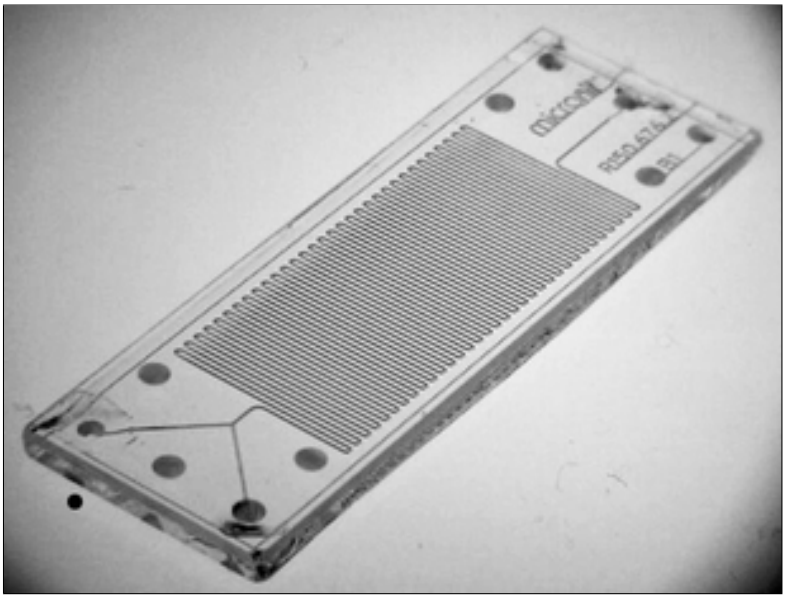


Figure 1.4 – A photograph of a simple glass "two-in-one-out" microfluidic chip for nanocrystal synthesis. The chip, which can be placed on a hot plate, features two inlets and one outlet joined by a Y-shaped junction and a ($150\,\mu m \times 150\,\mu m \times 67\,cm$) serpentine channel, along which nucleation and growth take place. Reproduced from Ref. 30 with permission of The Royal Society of Chemistry.

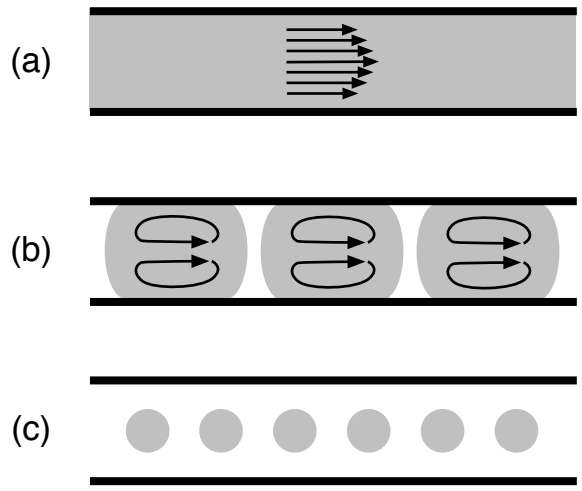


Figure 1.5 – Diagram showing three types of fluid flow in a microfluidic channel: (a) single-phase continuous flow, where contact with the channel walls leads to a parabolic flow profile; (b) segmented or "slug" flow where the reaction mixture is divided up into discrete units by an immiscible fluid; and (c) droplet flow where the reaction mixture is completely isolated from the channel walls by the immiscible fluid.

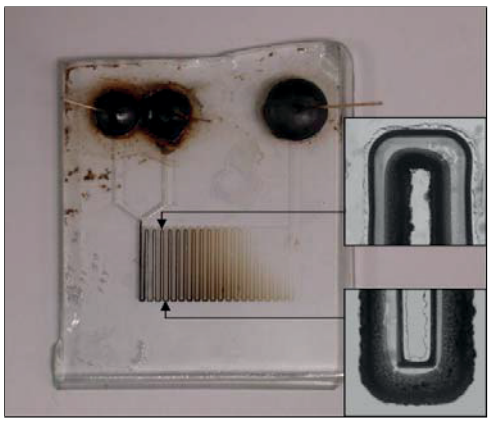


Figure 1.6 – Photograph of a blocked two-in-one-out glass chip used for InP nanocrystal synthesis. The left inlet corresponded to the In precursor and the right to the P precursor. Inset are images of the channels taken with an optical microscope. Reproduced from Ref. 38 with permission.

the flowing liquid drags against the channel walls inducing a parabolic velocity profile across the flow path, with the fluid moving fastest at the channel centre; this in turn generates a distribution of residence times within the reactor, leading to undesirable dispersion in nanoparticle properties.[37] Secondly, precursor and/or product deposition on the walls can lead to fouling, which affects the flow and ages the reactor. Left unchecked this can, and frequently does, lead to eventual failure through blockage. Figure 1.6 shows a photograph of a blocked two-in-one-out glass microfluidic chip used for InP nanocrystal synthesis in continuous flow. In and P precursors were injected into the two inlets located at the top left corner of the chip. It is clear that the channel walls began to foul immediately after the confluence of the precursor streams. The inset optical micrographs show that fouling is predominantly on the left side of the channel. By virtue of the laminar flow in the channel this fouling can be attributed to the In precursor.

Two-phase reactors elegantly overcome the drawbacks of single-phase reactors. Injection of an additional immiscible fluid (which can be a gas or a liquid) into the channel divides the reaction mixture into a succession of discrete "slugs" or "droplets" (Figure 1.5 (b) and (c)) that pass through the reactor at a common speed, eliminating velocity dispersion. In the case of slug flow,

the reaction mixture still makes contact with the channel wall, but abrasion from the second phase can help to reduce or even eliminate fouling, prolonging reactor lifetimes. Yen *et al.* were the first to use gas-liquid segmented flow reactors for high temperature nanocrystal synthesis, reporting the synthesis of CdSe from cadmium 2,4-pentanedionate and tri-*n*-octylphosphine selenide at 260 °C.[39] They achieved good size control by tuning the injection rates of the cadmium and selenium precursor solutions and reported significantly narrower emission spectra than an equivalent single-phase synthesis, consistent with the non-dispersive motion of the reagent slugs.

In the case of droplet flow, the reaction mixture is fully isolated from the wall by the immiscible liquid, thereby preventing reagent deposition from happening in the first place. Furthermore, if the droplets are large enough to fill the cross-section of the channel, they are forced to move in a direction parallel to the channel and cannot take unguided off-axis routes that would induce velocity dispersion. The use of droplet reactors for nanocrystal synthesis was first demonstrated by Shestopalov *et al.*[40] They used chip-based oil-water droplet reactors operating at room temperature to prepare cadmium sulphide quantum dots from ionic cadmium and sulphur precursor solutions. Figure 1.7 (a) shows how the microfluidic chip begins to foul within just 6 min of operation in continuous flow. In contrast, Figure 1.7 (b) shows that using segmented flow to isolate the reaction phase results in clean channel walls even after 30 min.

Chan and co-workers subsequently developed a high temperature chip-based droplet reactor in glass, using octadecene as the droplet phase, a high boiling point perfluorinated polyether (PFPE) as the carrier fluid, and a surface coating of perfluoralkylsilane to ensure preferential wetting of the channel walls by the carrier phase.[41] They were able to controllably synthesise high quality CdSe by reacting cadmium oxide and elemental selenium in the presence of oleic acid and trioctylphosphine at 300 °C, achieving good stable operation for up to five hours of continuous use.

Nightingale *et al.* later developed a capillary-based droplet reactor, using polytetrafluoroethylene (PTFE) tubing, capable of operating at temperatures of up to 250 °C.[27] Using the same carrier fluid and reagents as Chan

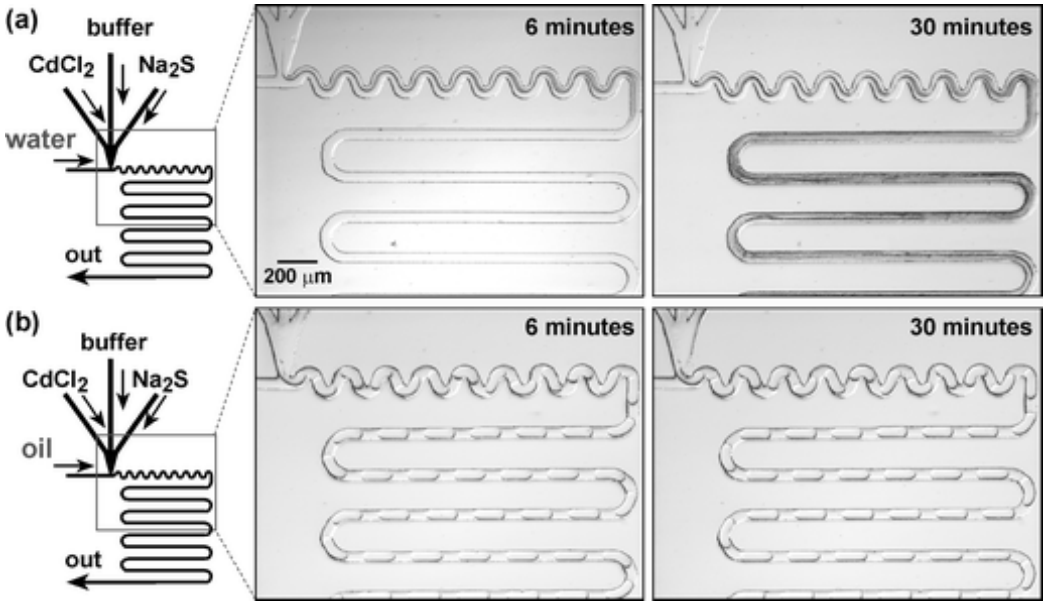


Figure 1.7 – Micrographs of microfluidic chips used by Shestopolov *et al.* for (a) continuous and (b) segmented flow synthesis of CdS nanocrystals. The micrographs show accumulation of solid CdS on the walls of the channels after 6 min and 30 min of operation in continuous flow. In contrast the walls remained clean after 30 min using droplet flow, as the reaction phase was confined to the droplets by the immiscible oil. Reproduced from Ref. 40 with permission of The Royal Society of Chemistry.

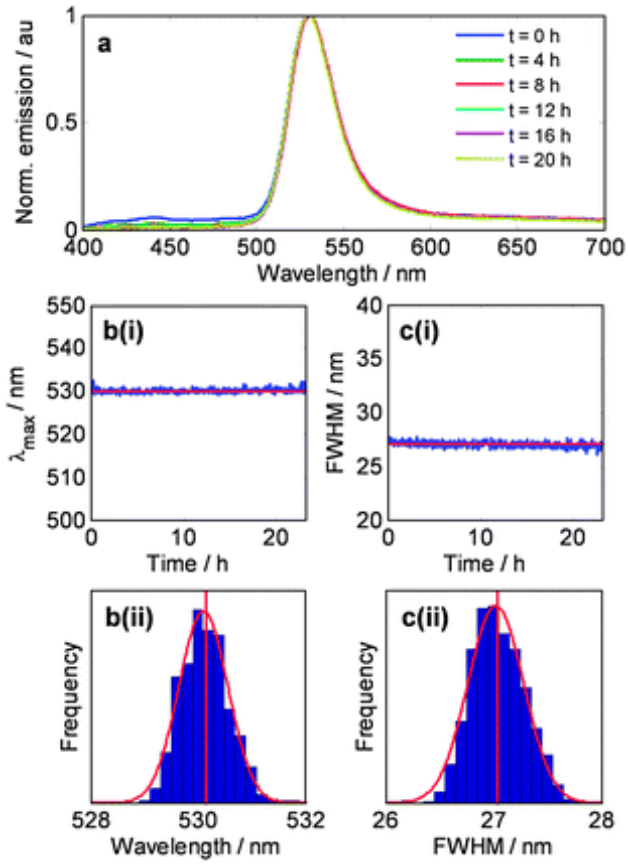


Figure 1.8 – Emission spectra of CdSe nanocrystals produced by Nightingale *et al.* using a droplet-based capillary reactor. (a) Time evolution of the emission spectra of droplet-synthesised CdSe nanocrystals under fixed reaction conditions. (b(i)) The peak wavelength of the band-edge emission versus time and (b(ii)) histogram of the same data. (c(i)) The full-width-half-maximum of the band-edge emission versus time and (c(ii)) histogram of the same data. Reproduced from Ref. 27 with permission of The Royal Society of Chemistry.

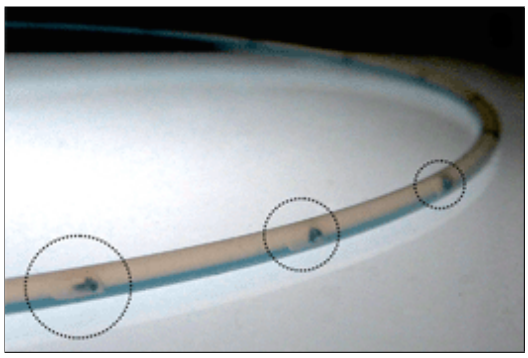


Figure 1.9 – Photograph showing the early stages of titania synthesis in the droplet reactor developed by Nightingale *et al.* Blue clouds of titanium oxide hydrate intermediates are clearly visible inside and entirely contained within the aqueous droplets. Adapted from Ref. 27 with permission of The Royal Society of Chemistry.

et al. they synthesized CdSe nanocrystals continuously over a 24 h period. Figure 1.8 shows emission spectra of the product obtained over one day. There is no discernible change in the emission spectra over time, implying consistent product over the duration of the experiment. They applied the same reactor to the synthesis of nanocrystalline silver, titania, and (in later work) superparamagnetic iron oxide,[42] reporting good operational stability in all cases. Indeed, the titania synthesis involved the formation of insoluble titanium oxide hydrate intermediates, clearly visible as blue clouds inside the droplets, yet did not cause reactor fouling (Figure 1.9). The authors noted anecdotally that during six months of testing with a wide variety of materials systems and synthesis routes they had yet to experience a single instance of reactor fouling, confirming the effectiveness of the droplet regime in preventing reactor fouling.

Each flow regime has advantages and disadvantages, and one must consider the chemistry at hand in order to determine the best flow regime to use. When single-phase flow can be used, it is the simplest method to implement. However, there are few (if any) situations where single-phase flow can be expected to offer a clear performance advantage over two-phase flow, and the circumstances in which it can be reliably applied are limited. High temperature reactions in organic solvents—particularly reactions that produce

colloidal nanocrystals or poorly soluble products—invariably cause single-phase reactors to foul and, for these, two-phase reactors must be used if consistent and reliable production is desired.

1.4 Inline analysis and optimisation

One of the key advantages of microfluidic syntheses is the ability to obtain real-time information about the progression of the reaction using "inline" sensors. These allow appropriate changes to be made to the reaction conditions to optimise yield, size-distributions, or physico-chemical properties. Optical techniques can be readily integrated with microfluidic devices due to their non-invasive nature, and can generate useful and immediate information about the nanocrystal properties.[43] Absorption and fluorescence methods are routinely used to extract information about size distributions and surface uniformity. This information can be used to manually tweak the reaction conditions to obtain a better product. However, by coupling both the sensor(s) and reactor to real-time control algorithms, the entire process of nanocrystal synthesis can be automated, with the control algorithm repeatedly and systematically updating the reaction conditions until a desired end-point is achieved. This approach was used by Krishnadasan *et al.* to develop a fully automated system for synthesizing CdSe quantum dots of a desired emission wavelength.[44] Toyota *et al.* later reported a rapid screening system for CdSe quantum dots, using five parallel microreactors and inline fluorescence spectroscopy to rapidly trawl through multiple reaction conditions with a view to obtaining improved particle characteristics and uncovering new mechanistic information (Figure 1.10).[45]

1.5 Large scale production

To date there has been little interest in microreactors as a potential production technology for nanocrystals due to a widespread perception that microreactors cannot satisfy industrial demand. This perception is certainly

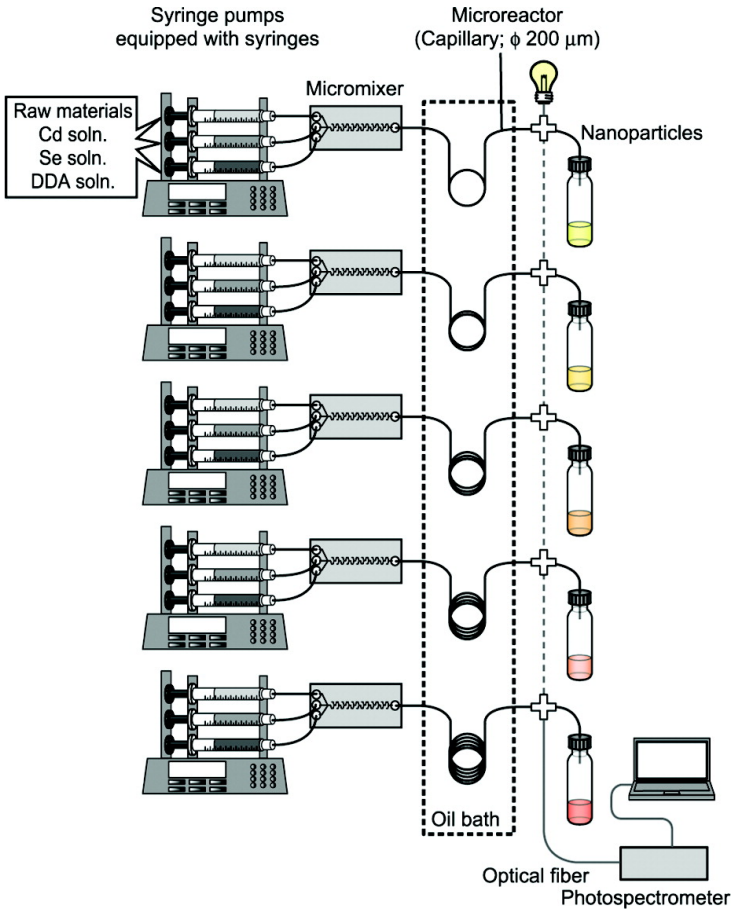


Figure 1.10 – Schematic of a microfluidic system developed by Toyota *et al.* for the rapid combinatorial synthesis CdSe quantum dots. Reprinted with permission from Ref. 45. Copyright 2010 American Chemical Society.

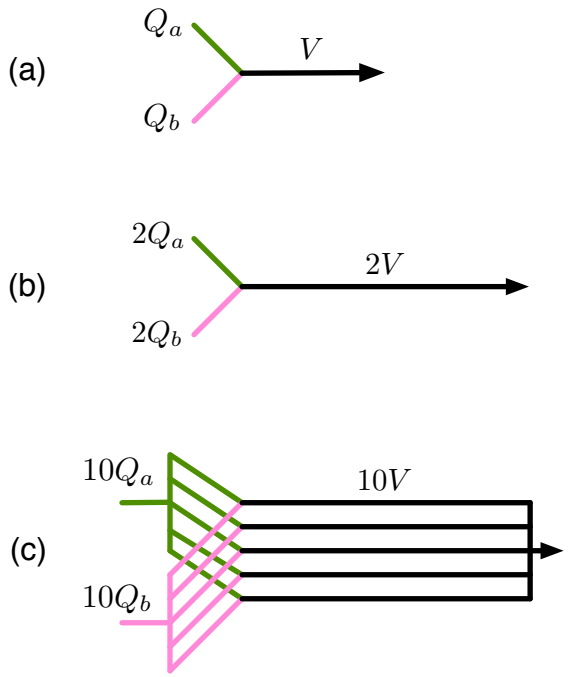


Figure 1.11 – Schematic of microfluidic reactors to illustrate the concept of scale out. In reactor (a) two precursors are pumped into a single channel at volumetric flow rates Q_a and Q_b. The precursors react as they flow through a channel of volume V. Product is collected at the outlet. In reactor (b), production rates are doubled by doubling both the flow rate of the precursors and the length (and hence volume) of the channel. In reactor (c), the reactor is *scaled out* by running five double-length channels in parallel to give a total reactor volume of $10V$. Precursors are fed from common pumps at $10Q_a$ and $10Q_b$, resulting in a production rate ten and five times greater than that obtained from reactors (a) and (b), respectively.

reinforced by the literature, where virtually all reports of materials synthesis in microreactors—nanocrystalline or otherwise—have involved small sub-gram levels of production. Throughput may be raised substantially by upping reagent concentrations, increasing flow rates (in combination with a proportionate increase in the length of the reactor) and *scaling out*, i.e. operating N identical reaction channels in parallel to achieve an N-fold increase in output relative to a single-channel reactor (Figure 1.11). Note that the diameter of the channel is not increased as this would result in the loss of the benefits of miniaturisation. Scaling out is an especially attractive approach since it requires no changes to the reactor geometry, and so allows materials throughput to be increased without any changes to the underlying process chemistry. Hence, in contrast to the scaling up of batch reactions, scaling out can in principle be implemented without any detriment to product quality or yield.

Despite its obvious importance, scale out has been a rather neglected aspect of microreactor technology, with only a handful of reports describing its application to large-scale materials production. The most notable success in this area was reported by Chambers and co-workers, who developed a thirty-channel device for the direct fluorination of organic molecules using fluorine gas.[47] They noted that twenty such reactors would have a combined throughput of approximately 3 kg/day, comparable to many fine-chemical processes. The extension of this approach to nanocrystals is appealing, but nanocrystal synthesis raises additional challenges due to the substantial risk of reactor fouling and the need to maintain identical conditions in all channels at all times (so as to ensure product consistency). In recent work Nightingale and co-workers reported a five-channel droplet-based microfluidic reactor for CdTe synthesis designed specifically to address these issues (Figure 1.12).[46] The precursor solution and carrier fluids were drawn from separate reservoirs, and split five ways using passive flow dividers. Individual streams of the precursor solution and carrier fluid were then merged on a pairwise basis in five separate junctions, creating parallel droplet streams in five intertwined capillaries. The capillaries were passed into a heated oil bath to initiate nucleation and growth, and the entire droplet stream from each one was

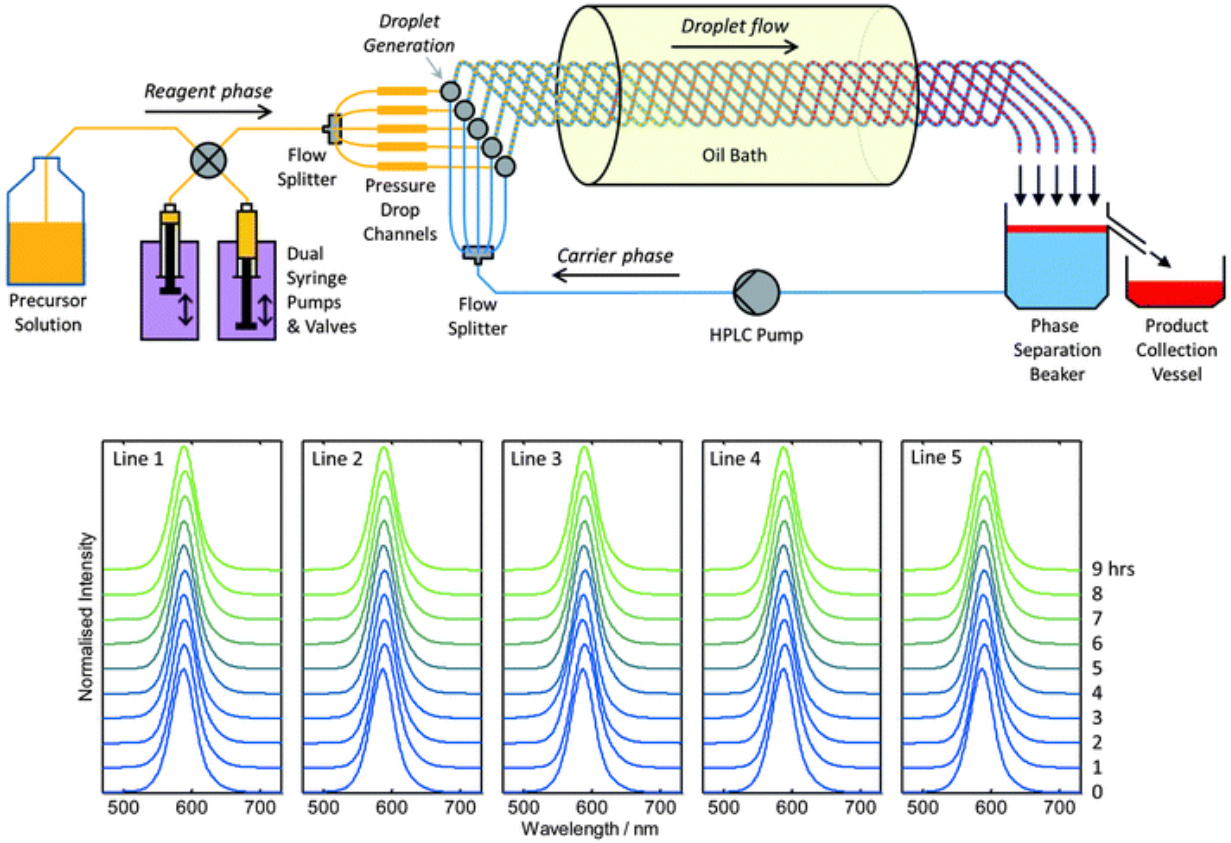


Figure 1.12 – Top: schematic of a scaled-out five-channel droplet flow reactor developed by Nightingale *et al.* for the synthesis of CdTe quantum dots at a rate of 145 g/day. Bottom: normalised solution-phase emission spectra of CdTe collected at hourly intervals from each of the five reaction lines over a period of nine hours. Adapted from Ref. 46 with permission from The Royal Society of Chemistry.

then collected in a single beaker. The carrier fluid sank to the bottom of the beaker, leaving the product as a discrete layer on top. (The carrier fluid was recycled in a closed-loop manner to minimise usage). During a nine hour production run, 54.4 g of material was produced corresponding to a production rate of 145 g/day. Absorption and fluorescence spectroscopy showed no change in product properties between channels and over time, confirming the stability of the multichannel droplet reactor.

1.6 Beyond batch techniques

Most reports of nanoparticle synthesis in microreactors have involved simple—albeit well controlled—adaptations of conventional macroscale synthesis procedures. However, microfluidics offers the chance to rethink the entire approach to nanoparticle synthesis by using techniques that are not available in batch chemistry. There have already been some efforts to exploit these advantages.[48] For instance Erdem *et al.* reported a silicon-based segmented flow microreactor for the synthesis of TiO_2 nanoparticles, incorporating separate hot and cool temperature zones to define a short period of nucleation followed by a longer period of slow, controlled growth—processes that are hard to separate in a batch system due to the difficulty of changing temperatures quickly.[49]

Many batch syntheses perform best under reflux conditions that cannot be used in flow. As an effective alternative, however, flow reactions can be readily performed under supercritical conditions through the use of a back-pressure regulator that permits fluid flow only after a target pressure has been reached. In this way the boiling point of the solvent can be increased above its standard value, allowing higher reaction temperatures to be accessed. Early work by Marre, Park, and co-workers confirmed the importance of supercritical reactions for nanocrystal synthesis.[50] They developed a pressurized high-temperature microreactor to synthesise quantum dots under supercritical conditions (Figure 1.13), showing that synthesis in supercritical hexane led to narrower emission line-widths and size distributions than the equivalent reaction in non-supercritical squalane. Their work highlights an

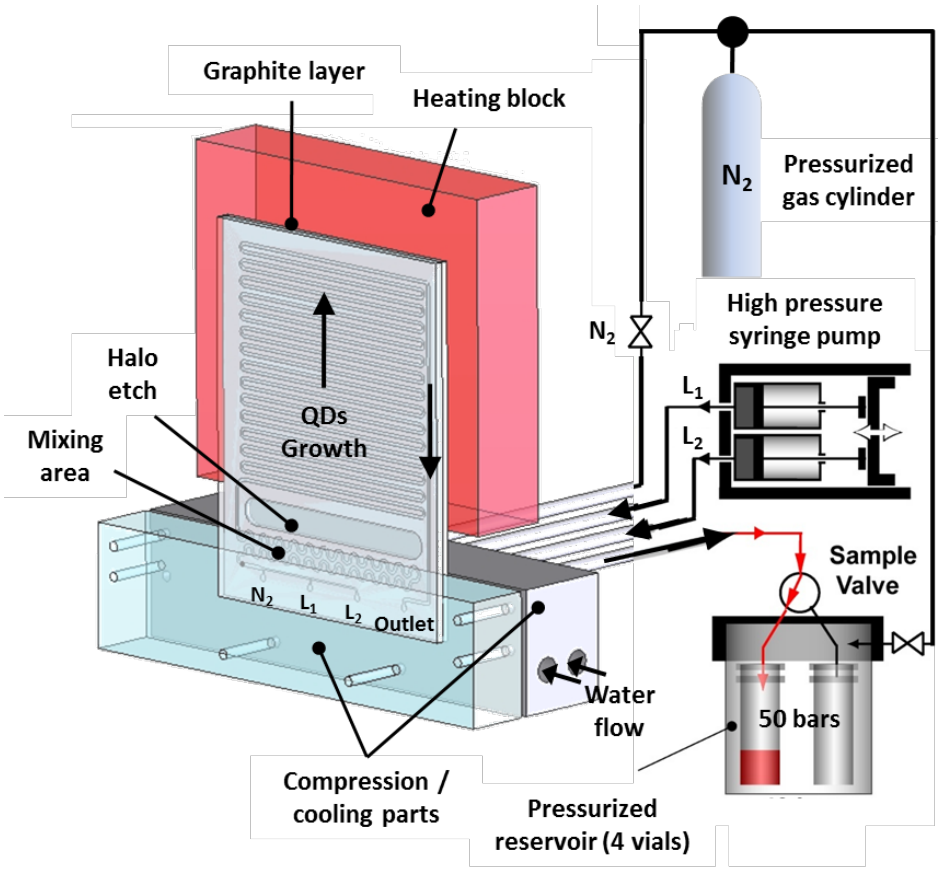


Figure 1.13 – High-pressure, high-temperature microreactor developed by Marre, Park *et al.*, comprising a compression-cooling aluminium part, a high-pressure syringe pump, a five-way high-pressure valve, and a high-pressure reservoir containing four vials. Reproduced from Ref. 50 with permission from John Wiley and Sons.

opportunity to explore and exploit the wider chemical parameter space that supercritical conditions unlock.

1.7 Summary

Since the first report in 2002 there have been some significant advances in the application of microreactors to nanocrystal synthesis. Key innovations include the transition from single-phase to two-phase flow reactors for improved reactor stability, the use of supercritical reaction conditions, the integration of sensor technology for real-time product evaluation, the use of control algorithms to optimise nanocrystal properties, and the demonstration of scale out as a viable means of increasing production volumes.

The vast majority of nanocrystal syntheses in microfluidic reactors use the strategy of adapting simple one- and two-step batch procedures to flow. Furthermore, most reports have involved syntheses of relatively simple nanocrystals. It is my view that the full benefits of microscale synthesis will likely only be realised when nanocrystal synthesis starts to be addressed from a flow-first perspective, using reaction schemes that have been designed from the ground-up for multistep synthesis in flow.

The following chapter introduces the synthesis of an anisotropic silver nanoparticle called a silver nanowire (AgNW). AgNWs are particularly challenging to synthesise—especially at large scale—using conventional batch processes. To my knowledge there have been only two reports of the continuous production of AgNWs and these have been with limited success. The objective of this work is to develop a reliable and scalable flow synthesis of AgNWs.

Chapter 2

Introduction to Silver Nanowire Synthesis

2.1 Polyol synthesis

The first solution phase synthesis of AgNWs was reported by Sun *et al.* at the University of Washington in 2002.[51] They adapted the polyol process, a reaction previously described by Fievet *et al.* in 1989 to prepare metal colloids,[52] in which a metal compound is dissolved in a polyol, such as ethylene glycol (EG) or diethyleneglycol, and heated to (or near to) reflux. The metal compound is reduced and forms colloidal metal via the nucleation and growth process outlined in Section 1.2.

Sun and co-workers produced Pt seeds by injecting $PtCl_2$ dissolved in EG into a heated sample of pure EG at 160 °C. They then added solutions of $AgNO_3$ and polyvinylpyrrolidone (PVP) in EG (Figure 2.1) to the Pt seeds, and continued heating at 160 °C for up to 60 min. After ∼20 min the reaction mixture turned turbid and grey. When an aliquot was removed and viewed using dark field optical microscopy (DFOM) nanorods could be observed.

Figure 2.2 shows SEM and transmission electron microscopy (TEM) images of crude samples removed from the reaction mixture and quenched between 10 min and 60 min after the addition of $AgNO_3$ and PVP. After 10 min (a), they saw Ag nanoparticles with a bimodal distribution of diam-

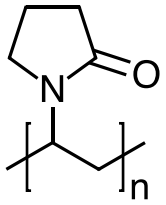


Figure 2.1 – Chemical structure of polyvinylpyrrolidone.

eters. Some nanoparticles were <5 nm and some were larger, around 20 to 30 nm. They suggested that the smaller particles formed through homogeneous nucleation of Ag atoms formed by the reduction of $AgNO_3$ while the larger nanoparticles formed through heterogeneous nucleation of Ag on the Pt seeds. After 20 min (b), some of the smaller particles had disappeared and the larger particles had grown, which they attributed to Ostwald ripening. A mixture of rods and spherical nanoparticles could be observed at this stage. After 40 min (c) and 60 min (d), the nanorods had grown into nanowires up to 50 µm long. Most of the small nanoparticles had dissolved. The authors added an excess of acetone to precipitate out the nanowires and then separated them from the nanoparticles by centrifugation. This procedure was repeated several times to yield nanowires with a mean diameter of around 38 nm and a standard deviation of 5 nm.

The researchers found that the yield and aspect ratio of the nanowires produced depended on the reaction conditions. In particular, the presence of PVP was essential to promote anisotropic growth, and if the reaction temperature deviated substantially from 160 °C, then the length of the nanowires decreased from around 50 to 2 µm. A ten-fold increase in the concentration of $PtCl_2$ led to a reduction in the diameter of the nanowires from 40 to 30 nm, consistent with a higher concentration generating more seeds for heterogeneous nucleation. The authors suggested that the PVP selectively-adsorbed to facets of the Ag, leading to kinetically-controlled and facet-selective growth of the nanoparticles into nanowires.

Later in 2002 Sun and Xia reported a self-seeding route that did not require seeding with Pt.[53] Instead of injecting the $AgNO_3$ and PVP solutions into the hot EG all at once, the precursors were added in parallel drop-wise

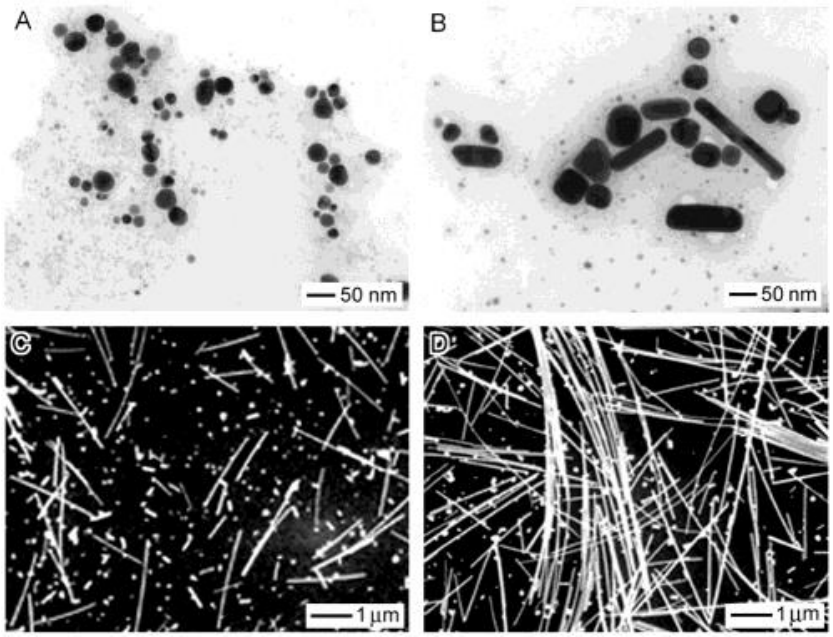


Figure 2.2 – TEM (a, b) and SEM (c, d) images of four crude samples of Ag nanoparticles and nanowires synthesised by Sun *et al.* Samples were taken from the reaction mixture 10 min (a), 20 min (b), 40 min (c), and 60 min (d) after the addition of the $AgNO_3$ and PVP solutions. Reprinted with permission from Ref. 51. Copyright 2002 American Chemical Society.

using a two-channel syringe pump. Unfortunately the crude nanowires were still contaminated by nanoparticles (by around 20 wt%) and thus required purification by centrifugation.

The authors investigated the effect of changing the mole ratio of PVP to $AgNO_3$ using PVP with a weight average molecular weight (M_w) of 55 kg/mol. Nanowires with aspect ratios as high as 1000 were produced when the ratio was 6:1. A higher ratio of 15:1 produced nanoparticles approximately 10 nm in diameter and ratios lower than 1:1 led to unacceptable decreases in yield and monodispersity. The researchers also examined the effect of changing the number of repeat units n in the PVP on the morphology of the product, trying $n = 1$ (monomer 1-ethyl-2-pyrrolidone), $n \approx 90$, and $n \approx 11700$. Nanowires with higher aspect ratios were obtained from PVP with a higher n. Other commodity polymers were tested, but only PVP produced anisotropic growth.

In a third paper published in 2002, Sun and co-workers combined the use of Pt seeds with the drop-wise addition of the $AgNO_3$ and PVP.[54] They reported the same trends as before for the effect of reaction temperature, ratio of PVP to $AgNO_3$, and Pt concentration on the nanoparticles and nanowires produced (up to 50 µm long). However, they stated that "the simultaneous and drop-wise addition of $AgNO_3$ and PVP solutions was critical to the formation of silver products with wire-like morphologies" in contradiction with their first report of seeded growth, where the $AgNO_3$ and PVP was not added drop-wise.

2.2 Growth mechanism

Following these papers, some questions remained regarding the origin of anisotropic growth and the role of PVP. In 2003, Sun and colleagues suggested the mechanism shown in Figure 2.3.[55] They proposed that nanowires grow from decahedral seeds enclosed by {111} facets and five "twin defects" arranged around a central axis.

A twin defect is a kind of stacking fault that is common in face-centred cubic (fcc) metals like Ag. Metal crystals are made up of layers of atoms

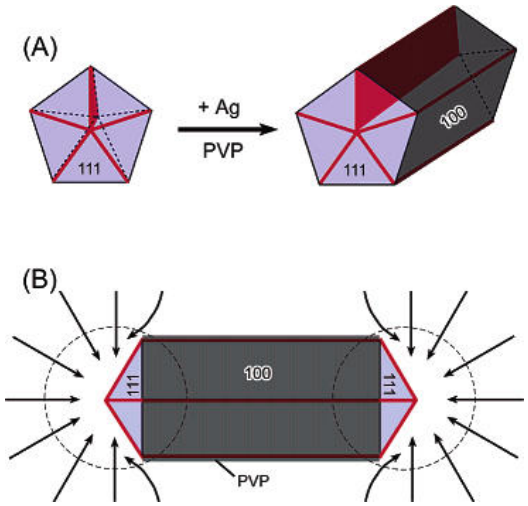


Figure 2.3 – Schematic of the mechanism proposed by Sun *et al.* for the growth of AgNWs.[55] In (a) MTPs formed at the start of reaction grow into rods in the presence of PVP. The dark grey colour represents the strong interaction between the {100} facets and PVP. PVP interacts only weakly with the {111} facets, shown in purple, allowing continued growth. The red lines represent the twin defects. (b) shows a projection perpendicular to the long axis of the rod. The strongly bound PVP prevents addition of the Ag atoms to the sides of the rod, leaving only the ends exposed for anisotropic growth into a wire. Reproduced with permission from Ref. 55. Copyright 2003 American Chemical Society.

arranged in a close-packed structure and the arrangement of these layers gives rise to two different crystal structures, hexagonal close-packed (hcp) and fcc. Figure 2.4 (a) shows a plan view of three adjacent layers in an hcp structure. A is the first layer of close-packed atoms. The atoms in the second layer B stack into the interstices of A. The third layer stacks into the interstices of B so that the atoms lie directly above the first layer A. This results in the stacking sequence $ABABAB$, where A denotes atoms that lie directly above one another and likewise for B. Figure 2.4 (b) shows three adjacent layers of the fcc structure. Layers A and B are as for the hcp structure. However the third layer of atoms sits in the interstices of B so that they are not directly above A, resulting in the fcc stacking sequence of $ABCABC$.

A twin defect occurs when the stacking deviates from this sequence, shown in Figure 2.5. In an fcc crystal, the layer following ABC should be A, but the atoms can mis-stack to form another layer B. If the sequence then continues uninterrupted the sequence is $AB\boldsymbol{C}BA$, where $\boldsymbol{C}$ forms the (111) twin defect.[56] The local structure around the defect is hcp, so the twin formation energy is related to the energy difference between fcc and hcp structures, and Ag and Au have the lowest energy barriers for incorporating twin defects among fcc metals.[57] Incoming growth units (atoms or clusters) move to a minimum energy position where the coordination to the surface is maximised. In general, there is a high likelihood of twin formation under conditions of high supersaturation since the addition rate of growth units will be high, meaning a growth unit that has by chance occupied a hcp position might not have the chance to move to the slightly lower energy fcc site before the arrival of an adjacent growth unit.[9]

Five-twinned decahedral seeds can be considered as assemblies of five tetrahedral single crystals arranged around a common axis, sharing a common edge and bounded by ten {111} triangular faces (see Figure 2.6 (a)). In fcc metals two {111} planes enclose an angle of 70.53°, which means that five units fall short of 360° by 7.35° (see Figure 2.6 (b)). Hence, there is an increase in the separation between atoms in the crystal lattice. The corresponding increase in energy due to the strain is compensated for by the expo-

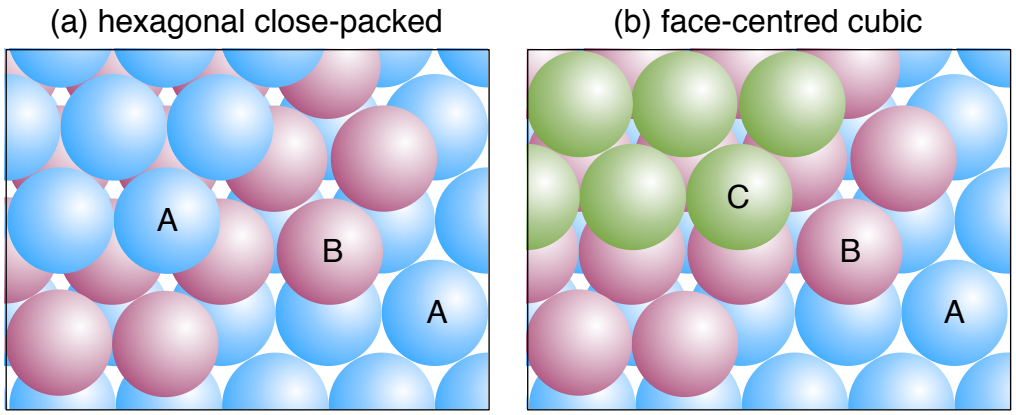


Figure 2.4 – Diagram showing a plan view of the close-packed layers in a hcp (a) and fcc (b) crystal structure.

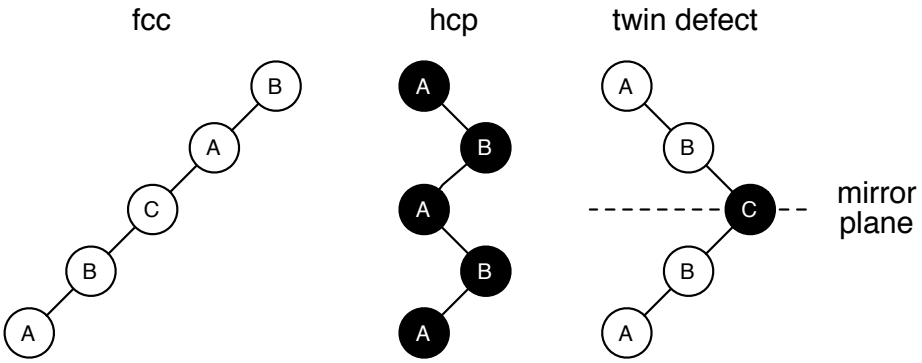


Figure 2.5 – Diagrams illustrating the stacking sequence in a fcc crystal, a hcp crystal, and a twin defect. Filled circles represent atoms in a local hcp environment.

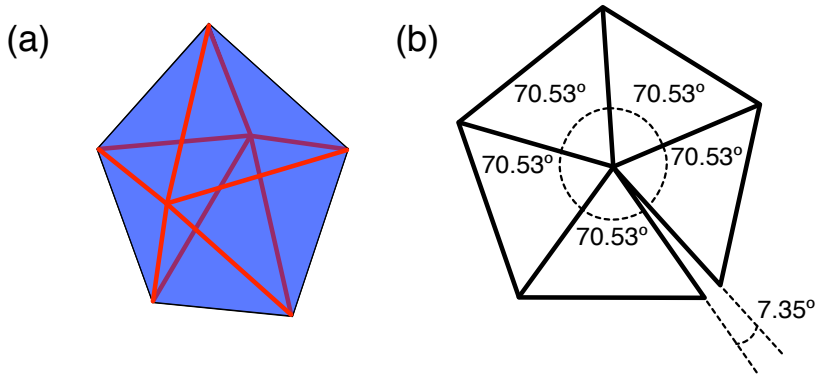


Figure 2.6 – (a) Drawing of a decahedral seed. The red lines show the boundaries of the twin defects. (b) Drawing of a five-fold twinned nanoparticle, showing how it is comprised of five tetrahedral subunits.

sure of the lowest energy {111} facets. (The surface energies of the low-index crystallographic facets are ordered $\gamma_{\{111\}} < \gamma_{\{100\}} < \gamma_{\{110\}}$.[58]) Ag atoms add to the twin boundaries during Ostwald ripening, since the boundaries are the highest energy site on a MTP, and this addition leads to anisotropic growth into a rod-like structure. (In contrast, isotropic growth is unfavourable, since it requires an increase in the area of the defective twin region, resulting in a large increase in strain that cannot be compensated for by the exposure of the {111} facets). The newly formed {100} facets are stabilised by chemical interactions between oxygen atoms of the PVP and the surface Ag atoms. The interaction of the PVP with the {111} facets must be weaker in order for the ends of the rod to grow continuously into a straight-edged wire with flat faces and a pentagonal cross-section.

Sun and colleagues presented three pieces of evidence to support the proposed growth mechanism. Firstly, TEM confirmed that some of the Ag nanoparticles present in the reaction mixture before nanorods appeared had a decahedral shape, while SEM showed that the nanowires had the expected pentagonal geometry. Secondly, electron diffraction patterns of single nanowires were complex and did not match patterns of fcc Ag, but were consistent with multiply-twinned Au nanorods with a pentagonal geometry. Thirdly, SEM images of AgNWs that had been broken by sonication re-

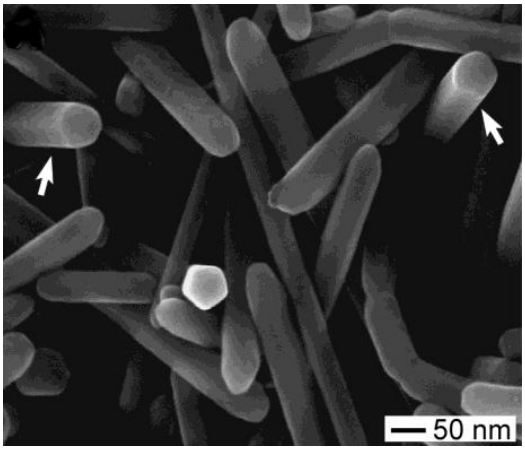


Figure 2.7 – SEM image of AgNWs that have been broken using sonication to show their pentagonal cross-section. Adapted with permission from Ref. 55. Copyright 2003 American Chemical Society.

vealed a pentagonal cross-section, consistent with their proposed mechanism (see Figure 2.7).

In addition, they demonstrated that PVP only interacts with the {100} facets by treating a dilute solution of AgNWs with 1,2-dodecanedithiol and Au nanoparticles. SEM showed that the ends of the AgNWs, but not the sides, were decorated with Au nanoparticles (which appeared as bright dots). The implication was that the PVP interaction only covered the {100} facets, leaving the {111} facets free to coordinate to the dithiol. This mechanism may also be consistent with the low yields and aspect ratios obtained using high ratios of PVP to $AgNO_3$, since a high concentration of PVP might result in coating of the {111} facets thereby preventing anisotropic growth.

Later the same year, Gao *et al.* published a report describing the synthesis and characterisation of AgNWs obtained using the self-seeding method.[59] They also observed nanowires with pentagonal cross-sections and recorded electron diffraction patterns that did not match single fcc crystals, leading them to propose the same nanowire growth mechanism as Sun and coworkers.

2.3 Ionic additives

2.3.1 Fe-mediated method

In 2005 Wiley *et al.* reported an investigation into the effect of adding Fe ions to the polyol synthesis.[60] They were motivated by their previous observation that twinned seeds could be selectively dissolved or "etched" by O_2 and Cl^- to produce single crystal truncated nanocubes and tetrahedra.[61] Because of the difficulty of precisely controlling the concentration of O_2 in the reaction mixtures, they were searching for non-gaseous etchants that could be added at controllable doping levels.

The authors used the same drop-wise addition of $AgNO_3$ and PVP as the self-seeding process, but also added a small amount of NaCl to the PVP solution. Without the NaCl, they found that the seeds aggregated to form irregular particles, which suggested that Cl^- was necessary for electrostatic stabilisation. They also used the same concentration of $AgNO_3$, but reduced the molar ratio of PVP to $AgNO_3$ from 6:1 to 1.51:1.

Wiley and colleagues found that AgNWs were produced in high yields when Fe^{3+} ions from either $Fe(acac)_3$ or $Fe(NO_3)_3$ were added to the solution of PVP and NaCl at Fe^{3+} and Cl^- concentrations of 2.2 µM and 0.06 mM respectively. Figure 2.8 shows TEM and SEM images of samples obtained using $Fe(acac)_3$ and $Fe(NO_3)_3$ at $t = 10$ min and 60 min. The authors claimed that the majority of the nanoparticles at $t = 10$ min were twinned and that these then grew into nanowires tens of microns long by $t = 60$ min.

They previously reported that, unless Fe^{3+} was added to the reaction mixture, the yellow colour of the Ag nanoparticles would disappear by $t = 2$ h, indicating the dissolution of the nanoparticles by oxidative etching.[61] Furthermore, when the reaction was carried out under an atmosphere of Ar in the absence of both Fe^{3+} and O_2, nanowires were still produced. From this they concluded that Fe^{3+} counters oxidative etching through the mechanism shown in Figure 2.9. They proposed that Fe^{3+} was reduced to Fe^{2+} by EG, and that the Fe^{2+} then reduced and removed atomic oxygen O_a from the

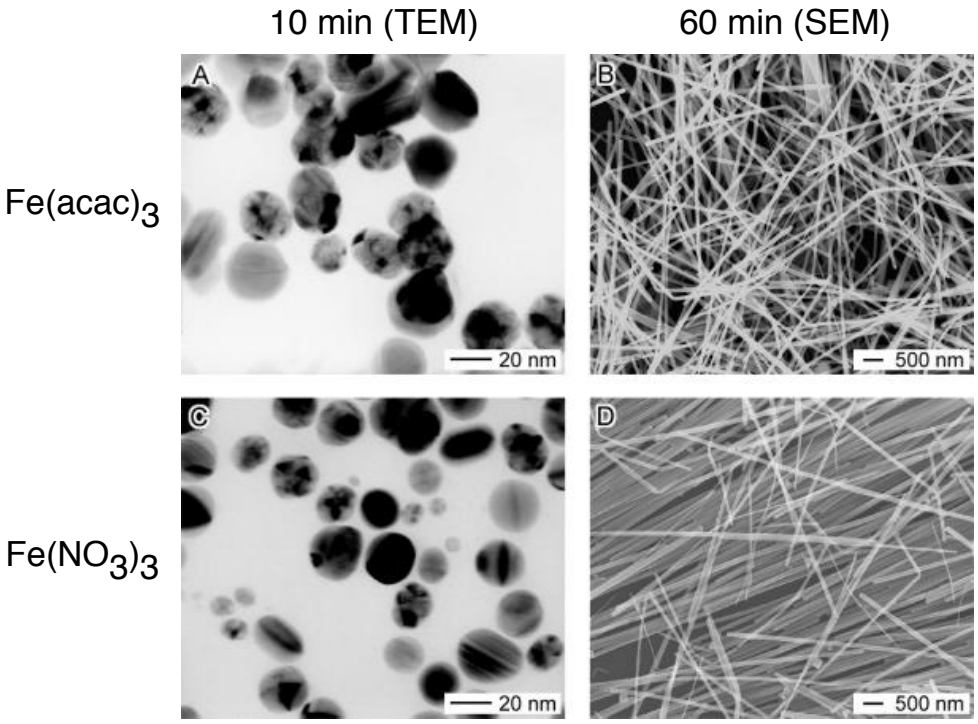


Figure 2.8 – TEM and SEM images of samples taken from reactions at $t = 10\,\text{min}$ (left) and 60 min (right) using the Fe-mediated method with 2.2 µM $Fe(acac)_3$ (top) or $Fe(NO_3)_3$ (bottom). Adapted with permission from Ref. 60. Copyright 2005 American Chemical Society.

surface of the Ag nanoparticles.[a] Otherwise, the O_a led to oxidative etching of the nanoparticles. They confirmed that Fe^{2+} was reduced by EG because the same results were obtained when $Fe(acac)_3$ was substituted for the same amount of $Fe(acac)_2$.

Wiley and co-workers also investigated the effect on the shape of the product of changing the concentration of the Fe additive. A ten-fold increase in the concentration of $Fe(acac)_2$ to 22 µM did not have a significant effect on the reaction, which again produced a mixture of twinned nanoparticles and single-crystal nanoparticles at $t = 10\,\text{min}$ and a high yield of nanowires at $t = 60\,\text{min}$. Another ten-fold increase in concentration to 220 µM led to the production of a mixture of irregularly shaped nanoparticles and rods at

[a]The authors cited previous studies that showed that between 200 K and 500 K O_2 will adsorb onto a Ag surface and dissociate into atomic oxygen O_a.[62–64]

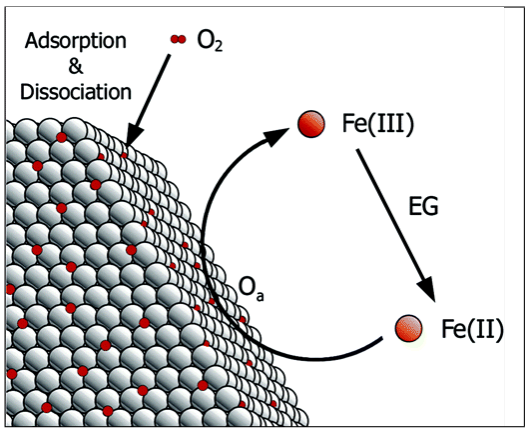


Figure 2.9 – Illustration of the mechanism by which Fe^{2+} removes atomic oxygen (O_a) from the surface of Ag nanostructures, preventing the dissolution of MTPs, proposed by Wiley *et al.*[60] Molecular oxygen (O_2) dissociates on the surface of the Ag nanostructure to form O_a. Fe^{2+} (from $Fe(acac)_2$ or the *in situ* reduction of Fe^{3+} from $Fe(acac)_3$) then reduces and removes O_a from the surface, prevent etching of the nanoparticle. Fe^{3+} is then reduced by EG back to Fe^{2+}, completing the catalytic cycle. Adapted with permission from Ref. 60. Copyright 2005 American Chemical Society.

$t = 10\,\text{min}$ and few nanowires at $t = 60\,\text{min}$. The researchers suggested that the high concentration of Fe^{3+} in the reaction mixture (produced by the oxidation of Fe^{2+} by O_a) etched the Ag nanostructures, leading to a rough and irregular morphology. This was consistent with the absence of etching when the same reaction was performed under an atmosphere of Ar. In summary, the authors showed that Fe ions could be used to protect MTPs in aerobic conditions and that the addition of Fe ions could be beneficial for the synthesis of AgNWs.

2.3.2 $CuCl_2$-mediated method

In 2008 Korte *et al.* reported a method of synthesising AgNWs using $CuCl_2$.[65] They heated EG to 151.5 °C for 1 h and then added a solution of $CuCl_2$ in EG to give a final concentration of Cu^{2+} and Cl^- of 20 µM and 40 µM respectively. They then sequentially injected solutions of PVP and then $AgNO_3$ (in a single shot, rather than drop-wise with a syringe pump). The authors reported that

the reaction was insensitive to small changes in the concentration of $CuCl_2$, but that deviation from the reaction temperature of 151.5 °C by as little as 10 °C substantially reduced the nanowire selectivity.

To study the effect of Cu^{2+} ions in the absence of Cl^- ions, the researchers substituted $CuCl_2$ for an equimolar amount of $Cu(NO_3)_2$ and reported that only Ag nanoparticles were obtained. The addition of a trace amount of NaCl for electrostatic stabilisation did not result in anisotropic growth. When only Cl^- ions were added (from NaCl, at the same concentration of 40 µM) only isotropic nanoparticles were obtained. Hence both Cu^{2+} and Cl^- appeared to be necessary to obtain nanowires.

Korte and colleagues concluded that the high concentration of Cl^- reduces the concentration of Ag^+ in the reaction mixture through the formation of AgCl and so reduces the nucleation rate at the start of the reaction. As free Ag^+ is consumed, the AgCl gradually dissociates and releases Ag^+, effectively mimicking the drop-wise addition of a syringe pump. This slow release conveniently favours the formation of smaller, thermodynamically more stable decahedral seeds and enables their sustained growth into wires.

Similarly to Wiley and colleagues, Korte investigated the effect of the Cu oxidation state and found that it did not significantly affect the outcome of the reaction. As with Fe(II) and Fe(III), they proposed that Cu(I) added directly or generated *in situ* from the reduction of Cu(II) by EG scavenges O_a from the surface of the Ag seeds, facilitating anisotropic growth. Figure 2.10 shows TEM images of seeds produced 3 min and 15 min after the addition of $CuCl_2$, showing the rapid onset of anisotropic growth.

2.4 Other batch routes

Since the first reports of AgNW synthesis using the polyol reaction, various modifications to the general synthesis route have been reported with a view to improve the shape-selectivity, aspect ratio, and yield of the nanowires, with varying degrees of success. For example, Yang *et al.* reported the use of glycerol ($HOCH_2C(OH)CH_2OH$) instead of EG, and Jia *et al.* blended glycerol and EG, although neither produced nanowires that were any longer

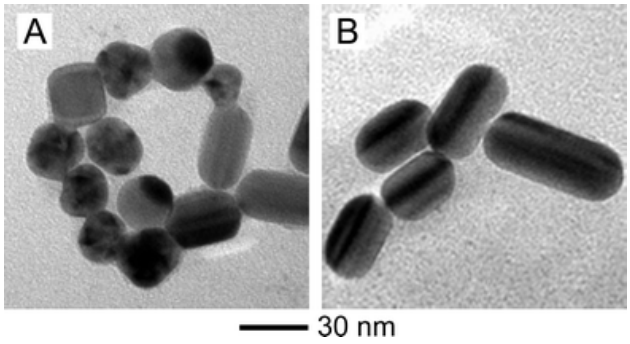


Figure 2.10 – TEM images of Ag seeds produced $t = 3\,\text{min}$ (a) and 15 min (b) using the $CuCl_2$-mediated method.[65] Adapted from Ref. 65 with permission of The Royal Society of Chemistry.

than those that had already been reported.[66,67]

In 2011 Coskun *et al.* reported an investigation into the effect of varying the stirring rate, the molar ratio of PVP to $AgNO_3$, the injection rate, the reaction temperature, and the concentration of NaCl on the product morphology.[68] Despite the limitation of only varying one parameter at a time, Coskun and co-workers established several trends. In particular, higher reaction temperatures (from 130 to 190 °C) resulted in a reduction in the diameter of the nanowires, accompanied by a slight increase in length, and higher molar ratios of PVP:$AgNO_3$ led to a reduction in both diameter and length. Higher stirring speeds led to a reduction in diameter and length, from $\sim 110\,\text{nm} \times 18\,\mu\text{m}$ with no stirring, to $\sim 60\,\text{nm} \times 10\,\mu\text{m}$ when stirring at 1000 rpm. Jiu *et al.* reported a similar trend.[69]

The concentration of NaCl was not found by the researchers to have a strong effect on the diameter and length of the nanowires. Instead, an optimum concentration of 12 µM was found to produce the highest yield of nanowires, with the omission of NaCl resulting in isotropic nanoparticles and the use of higher concentrations resulting in large (1 to 3 µm) particles of AgCl. As previously discussed, it has been suggested that Cl^- ions are necessary for electrostatic stabilisation of seeds[60] and/or to form AgCl that slowly releases Ag^+ ions by dissociation as Ag^+ ions are consumed.[65,70] Schuette and colleagues have also reported investigations into the role of Cl^- ions in the polyol synthesis, finding that AgNWs can heterogeneously nu-

cleate from AgCl nanocubes produced at the start of the synthesis.[71] The nanowires eventually detach from the nanocubes, which can either be generated *in situ* or added from a separate reaction. Without the addition of NaCl, they could not produce nanowires. In a follow-up paper, they found that the diameter of the nanowires was independent of the size of the nanocubes,[72] consistent with a finding by Coskun *et al.* that the diameter did not change with NaCl concentration.

In 2012 Lee *et al.* reported a method for the multi-step growth of nanowires.[73] They first synthesised AgNWs by dropwise addition of $AgNO_3$ and PVP in the presence of $CuCl_2$. By optimising the addition rate and sonication of the $AgNO_3$ precursor, they achieved an increase in the median length from *ca.* 10 to 50 µm. The authors claimed that sonication produced 2 nm Ag seeds (observed using TEM) that improved selectivity.[b] The crude nanowires were added to hot EG containing more $CuCl_2$ and PVP, followed by the dropwise addition of further $AgNO_3$. This process was repeated several times to produce nanowires with a median length of approximately 100 µm, albeit with extremely large length polydispersity (ranging from 10 to 400 µm).

In 2012 Bergin *et al.* reported a method similar to that described by Korte and colleagues, using $Fe(NO_3)_3$ as an O_2 scavenger and NaCl instead of $CuCl_2$ as a Cl^- source.[74] By varying the reaction temperature and time, they produced AgNWs up to 25 µm in length (Figure 2.11). Their method did not require dropwise addition, and was scaled up by the authors to a total mass of 0.55 g Ag (200 mL reaction volume).

The aforementioned syntheses all involve the addition of a precursor to a flask of hot EG. Lim *et al.* reported a different method in 2014 whereby a room temperature flask of $AgNO_3$, PVP, and $Fe(NO_3)_3$ in EG is stirred and heated to 151.5 °C at a rate of 1.4 °C/min, then kept at that temperature for 1.5 h.[75] They found that this heat-up method produced nanowires with a mean length and diameter of 21 µm and 84 nm respectively (Figure 2.12 (a)). In contrast, the hot-injection procedure (where the $AgNO_3$ was added all at once) produced polyhedral nanocrystals (100 to 150 nm, Figure 2.12

[b]It is worth noting that sonication is usually accompanied, whether intentionally or not, by heating. Therefore this apparent benefit might in fact be thermally driven.

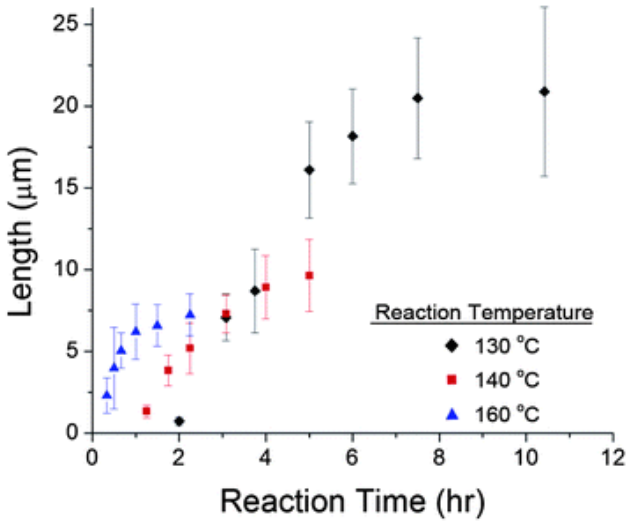


Figure 2.11 – Graph showing the effect of reaction time and temperature on the length of AgNWs produced by Bergin *et al* using $Fe(NO_3)_3$ and NaCl.[74] The authors did not state what the error bars represent. Adapted from Ref. 74 with permission of The Royal Society of Chemistry.

(b)). In both cases samples were taken when the reaction mixture turned yellow, indicating the formation of Ag nanoparticles, at $t = 90$ min for the heat-up method and at $t = 30$ min for the hot-injection method. Analysis of these samples using TEM showed that the nanoparticles produced using the heat-up method were multiply-twinned, whereas those produced in the hot-injection reaction were single crystals (that did not have the crystallographic structure to grow into a nanowire).

In 2015, Li *et al.* modified Bergin's method to use a heat-up route similar to that reported by Lim and co-workers.[76] They stirred a solution of NaBr, NaCl, PVP, and $AgNO_3$ in EG for 30 min at room temperature, and then heated the mixture to 170 °C. During heating, nitrogen gas was bubbled through the reaction mixture. Once the reaction mixture reached 170 °C, stirring was stopped and the mixture was left to react for 1 h. They found that the addition of NaBr reduced the diameter of the nanowires produced. Without NaBr, the nanowires were 72 ± 15 nm in diameter and 63 ± 17 µm in length. But with 2.2 mM NaBr, the diameter decreased to 20 ± 2 nm, with lengths of 40 ± 13 µm. (Any further increases in the concentration of NaBr

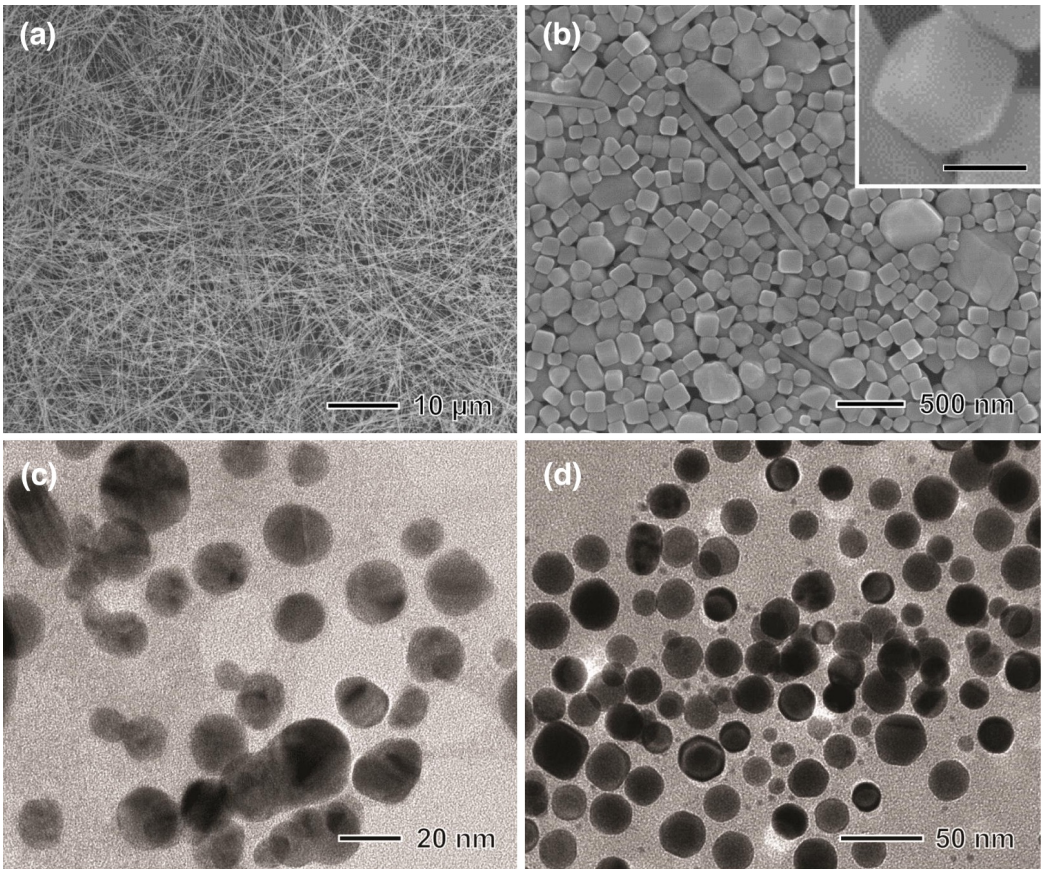


Figure 2.12 – SEM images of products obtained by Lim *et al.* using the heat-up (a) and hot-injection method (b).[75] The first approach yielded nanowires with a mean length of 21 µm while the second yielded nanoparticles that were approximately 100 to 150 nm in diameter. (b, inset) shows a high magnification image of a polyhedral nanoparticle. The scale bar is 100 nm. TEM images of samples taken at $t = 90$ min from the heat-up reaction (c) and $t = 30$ min from the hot-injection method (d). The inhomogeneous contrast of the nanoparticles in (c) indicates that the nanoparticles are multiply-twinned, in comparison to the single crystals in (d). Adapted from Ref. 75 with permission from Elsevier.

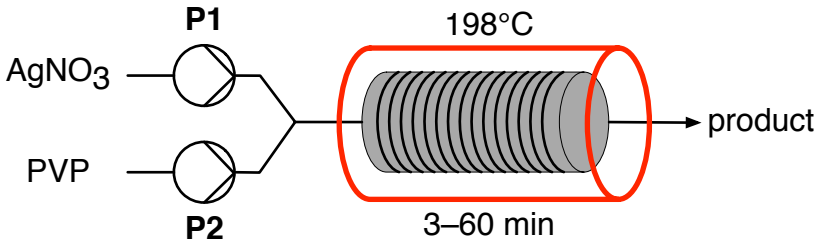


Figure 2.13 – Schematic of the reactor used by Gottesman *et al.* for the continuous flow synthesis of AgNWs. EG solutions of $AgNO_3$ and PVP are separately pumped by continuously-pumping dual-channel syringe pumps **P1** and **P2** into a PTFE coil. The PTFE coil is wrapped around an aluminium cylinder and placed inside a furnace at 198 °C. The product is collected at the outlet into a vial. By adjusting the flow rates residence times in the heated section are varied between 3 min and 60 min. Schematic drawn from the information in Ref. 77.

led to an increase in the number of nanoparticles produced.) The authors argued that the reduction in diameter induced by NaBr was caused by the increase in the number of nucleation events.

2.5 Continuous flow routes

To my knowledge there are only two reports relating to the flow synthesis of AgNWs. In 2012 Gottesman *et al.* reported a method for the continuous flow synthesis of AgNWs.[77] Separate solutions of $AgNO_3$ and PVP ($M_w \approx 58$ kg/mol) were pumped into a PTFE tube (internal diameter (ID) 1.5 mm) wrapped around an aluminium cylinder and placed inside a furnace at 198 °C. With a 30 min residence time, the AgNWs produced had an average length of 10 µm and diameter of around 70 nm. Gottesman did not report the use of halide or metal ions and did not specify the supplier and grade of the EG, so it is possible that the results were serendipitous (see Section 2.6 for further discussion). The authors did not comment on fouling of the reactor—which has plagued other continuous flow syntheses of nanoparticles—nor about the consistency of the product during operation. Additionally, they did not specify the flow rates of the precursor solutions,

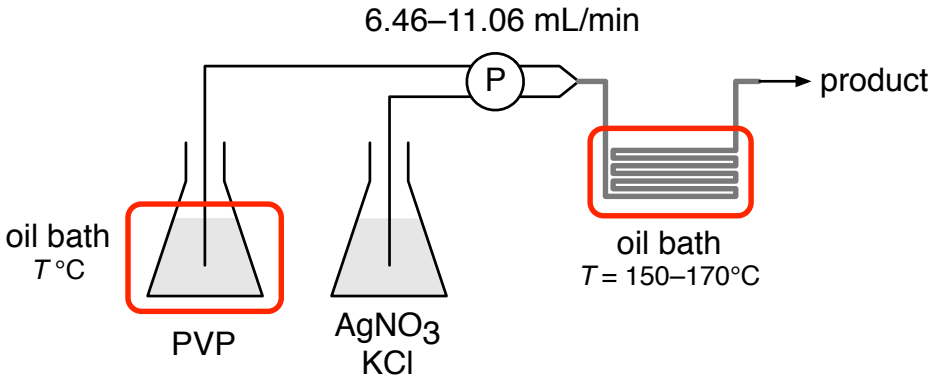


Figure 2.14 – Schematic of the continuous flow glass millifluidic reactor used by Chou *et al.* to synthesis AgNWs. Solutions of PVP (immersed in an oil bath at the reaction temperature T) and $AgNO_3$ and KCl (at room temperature) were pumped by peristaltic pump **P** into a glass tube (ID 6 mm and OD 8 mm; length unspecified). The glass tube was immersed in an oil bath at $T = 150\,°C$, 160 °C, or 170 °C. Product was collected at the outlet of the glass tube into a flask. The residence time was varied between 8 to 30 min. Schematic drawn from the information in Ref. 78.

nor the length or volume of the PTFE reaction coil.

In 2015 Chou *et al.* reported the continuous flow synthesis of AgNWs in a glass tube reactor.[78] Figure 2.14 shows a schematic of the reactor used by Chou and co-workers. They prepared two EG solutions: one of PVP ($M_w \approx 360\,kg/mol$) and another of $AgNO_3$ and KCl (to form AgCl seeds). The flask of PVP was heated in an oil bath at the same temperature as the reaction coil, although the authors did not report why. Both of these solutions were pumped into a glass tube with a relatively large ID of 6 mm and an OD of 8 mm that was immersed in an oil bath at a temperature of 150 °C, 160 °C, or 170 °C.

The report omits several important experimental details. The authors did not specify the length or total volume of the tube, nor its geometric shape. Neither did they specify whether the flow rate was the total flow rate or the flow rate of each precursor solution. They reported results for residence times between 8 and 30 min and specified corresponding flow rates in the range 6.46 to 11.06 mL/min. For a given reactor volume, the ratio of the total flow rate to residence time is a constant, but for the specified flow rates and residence

times, this is not the case. It is therefore reasonable to conclude that the authors have either incorrectly reported their reaction parameters or changed the length of the glass coil without saying so. Furthermore, the authors did not comment on the operational stability or fouling of the reactor, other than stating the need to flush the reactor with dilute HNO_3, followed by water and ethanol (which suggests fouling is an issue).

Nonetheless, with parameter optimisation the reactor produced nanowires with an average length and diameter of 22 µm and 90 nm, respectively. It is interesting to note that all the precursors were added to the reactor at once, unlike the usual batch approach of adding precursors drop-wise. The authors reasoned that the relatively large diameter of the glass tube results in the reaction mixture gradually reaching the reaction temperature (140 °C by $t \approx 2.5$ min and 147.5 °C by $t \approx 7.5$ min), much like the previously mentioned heat-up methods.

2.6 Challenges

2.6.1 Contaminants in ethylene glycol

The AgNW literature contains many contradictory conclusions about the conditions needed for nanowire growth. For example, in Sun and co-workers' self-seeding route,[53] no Cl^- was added to the reaction, but later Wiley[60] and Korte[65] found Cl^- was essential. A potential reason for the different findings is substantial variations in the level and identity of of ionic impurities present in research-grade EG. Indeed, Wiley and colleagues noted in a paper reporting the synthesis of single-crystal Ag nanoparticles published in 2004 that their EG was contaminated by different concentrations of chloride ions, ranging from 0.0019 to 0.116 mM (determined by evaporation followed by ion chromatography).[61] On this basis they recommended the use of EG from J.T. Baker, which had the lowest level of chloride ions, and acknowledged that previous results may have been due to sample contamination.

Fe ions are also found in many batches of EG. For example, in the first reports of AgNW synthesis by Sun and co-workers Fe ions were not added to

the reaction mixtures and the reactions were carried out in air.[51,53,54] Later, Wiley and colleagues reported that the addition of Fe ions was essential for AgNW growth in air, noting that it is possible for EG to be contaminated by Fe due to its synthesis and storage in steel vessels.[60]

These factors may explain why some reports—such as the continuous flow routes by Gottesman and Chou—describe the successful production of AgNW in the apparent absence of Fe^{2+}/Cu^{2+} and Cl^-. The significant variations in the ion content of EG also raises concerns with regards to reproducibility, which is of key importance for large scale production of AgNWs.

2.6.2 Glycolaldehyde as a reducing agent

Despite the success of the polyol synthesis in producing a wide variety of metal nanoparticles, there has been little discussion regarding the mechanism of how EG reduces metal ions. Skrabalak *et al.* published a report in 2008, suggesting that heating EG in air results in its oxidation to the reducing agent glycolaldehyde (GA):[79]

$$2\,HOCH_2CH_2OH + O_2 \longrightarrow 2\,HOCH_2CHO + 2\,H_2O \qquad (2.1)$$

Skrabalak and colleagues could not detect GA using gas chromatography-mass spectrometry and did not observe a change in the nuclear magnetic resonance (NMR) spectrum of EG before and after heating it for 1 h in air at 150 °C. Despite this, they used a spectrophotometric method, originally reported in 1967 by Basson and Du Plessis, where glycolaldehyde is oxidised by perchloric acid to produce gloyxal.[80] Glyoxal then reacts with 2,4-dinitrophenylhydrazine to produce glyoxal bis-2,4-dinitrophenylhydrazone, which has a characteristic blue colour due to an absorption maximum at 560 nm. Unfortunately, Skrabalak and co-workers did not characterise the structure of the derivative, so there is still a lack of concrete evidence for GA being the reducing agent.

2.6.3 Nanowire purification

For applications as a transparent conducting electrode, AgNW inks must be of high purity. Ag nanoparticles are detrimental to the performance of a AgNW transparent conducting electrode because they do not contribute to the percolating nanowire network and cause significant optical losses due to their strong absorption and scattering of visible light.[81]

Inevitably the polyol synthesis of AgNWs produces isotropic nanoparticle side-products, but few reports comment on the shape monodispersity. Researchers typically isolate nanowires by precipitation (by the addition of acetone) and separate them from the nanoparticles by centrifugation. The product is typically washed and centrifuged 2–3 times before being dispersed into a solvent such as water or ethanol. For a given rotor of radius r rotating with an angular velocity ω the relative centrifugal force (RCF) $= r\omega^2/g$, where g is acceleration due to gravity. Unfortunately, researchers rarely provide the RCF and instead state the rotational speed in revolutions per minute and centrifugation time. Without the rotor radius r, it is not possible to be certain whether researchers are trying to isolate the entire product—both nanowires and nanoparticles—or separate nanowires from side-products, and thus whether TEM or SEM images are representative of the crude solution.

Pradel *et al.* reported the separation of nanowires and nanoparticles using cross-flow filtration through a porous hollow fiber filter.[82] More recently, Li *et al.* selectively precipitated nanowires by slowly adding acetone to the crude product mixture, leaving the nanowires to sediment by gravity.[76] Two to four cycles of this process yielded high purity nanowires. Obviously, it would be better to avoid the need for purification altogether by only producing AgNWs. This remains a challenge.

2.7 Summary

Since the early reports by Sun and colleagues in 2002, many researchers have synthesised AgNWs using variants of the polyol process, achieving different lengths, diameters, and degrees of polydispersity. At its simplest, AgNWs

grow from five-fold twinned decahedral seeds in the presence of PVP, but it now seems likely the reaction is assisted by contaminants in EG. The importance of certain ionic species has been demonstrated, in particular metal ions such as Fe and Cu in helping protect the decahedral seeds from O_2, while Cl^- is important for sustaining nanowire growth and so obtaining AgNWs with high aspect ratio and monodispersity. Key to the successful production of AgNWs with minimal isotropic by-products (that do not require labour-intensive purification) is the production of decahedral seeds to the exclusion of all other shapes. Gradually heating up the reaction mixture from room temperature has been demonstrated to be a superior method for obtaining five-fold twinned seeds than standard hot-injection methods, in both flow and batch. In the following chapter I describe my improvements to a previously reported batch synthesis of AgNWs. My findings also highlight the sensitivity of the reaction to temperature and small changes in the concentration of chemical contaminants in EG.

Chapter 3

Batch Synthesis of Silver Nanowires

3.1 Introduction

As discussed in Chapter 2, AgNWs have been synthesised using many variations of the polyol synthesis, in which $AgNO_3$ is thermally reduced by EG (or a longer glycol) in the presence of PVP. The method reported by Bergin *et al.* was chosen as a starting point for this work.[74] In the synthesis, EG is heated to between 130 and 160 °C for 1 h in an oil bath. Afterwards, EG solutions of NaCl, $Fe(NO_3)_3$, PVP, and lastly $AgNO_3$ are added sequentially to the hot EG. The authors specified this particular order of addition, but noted that the time between each addition (about 30 s) is not critical. The reaction flask is stoppered and the mixture is left to react for between 0.5 and 12 h, with lower temperatures requiring longer reaction times.

This method was chosen here for three reasons. Firstly, the Cl^- and $Fe^{2/3+}$ ions are added from separate sources (NaCl and $Fe(NO_3)_3$), thus enabling their concentrations to be varied independently. This is not possible if a single reagent is used to supply both species, e.g. $CuCl_2$. Secondly, Bergin and co-workers demonstrated that the length and diameter of the AgNWs could be varied by adjusting the reaction time and temperature. Both features of the synthesis allow for the possibility of systematically varying the reaction

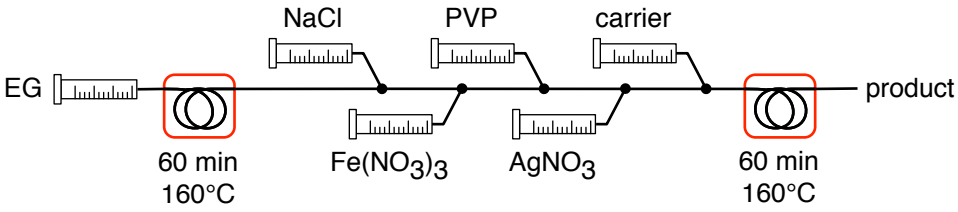


Figure 3.1 – Schematic of a hypothetical flow reactor that closely follows the batch synthesis of AgNWs described by Bergin *et al.* EG is pre-heated by pumping it into a coil of tubing immersed in an oil bath at 160 °C with a residence a time of 1 h. Solutions of NaCl, $Fe(NO_3)_3$, PVP, and $AgNO_3$ are then individually pumped into the stream of EG using Y-mixers. Lastly carrier fluid is pumped into the channel to generate a segmented flow, which enters a second oil bath (160 °C, 1 h residence time) where the reaction takes place. The flow at the outlet is collected into a vial.

parameters in flow to optimise for parameters such as AgNW length, diameter, or yield. Lastly, the procedure does not require dropwise addition of the $AgNO_3$ solution, which in flow would require the use of more complicated three-phase flow regimes (gas-liquid-liquid) to reliably dose each droplet.[35]

Before constructing a prototype flow reactor it was first necessary to establish which steps of the synthesis were critical to the success of the reaction and would therefore need to be replicated in flow. It is trivial to pre-heat the EG for 1 h and sequentially add precursor solutions in batch, but not in flow. Figure 3.1 shows a schematic of a hypothetical flow reactor that is intended to replicate the steps of the batch synthesis as closely as possible. EG is pumped into a coil of tubing, immersed in an oil bath at 160 °C, with a residence time of 1 h. Solutions of NaCl, $Fe(NO_3)_3$, PVP, and $AgNO_3$ are individually pumped, one after the other, into the stream of EG using four Y-mixers. Next, a segmented flow is created by pumping carrier liquid into the stream of reaction mixture. Use of a segmented flow can help to prevent fouling in the final reaction stage, when the reagents enter a second heated coil at 160 °C for 1 h. Here the $AgNO_3$ is reduced and nucleation and growth occurs. The crude product is collected at the outlet into a vial, where it separates from the carrier fluid by gravity.

This reactor is relatively complex, requiring six pumps and five junctions,

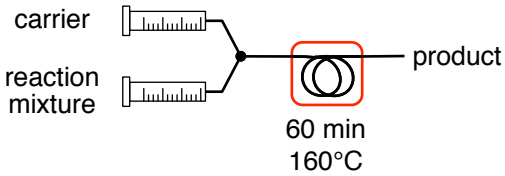


Figure 3.2 – Schematic of a simple flow reactor for AgNW synthesis where the reagents are combined into single reaction mixture. The reaction mixture and carrier fluid are injected into a two-in-one-out junction to produce a segmented flow.

and so there is a high initial cost of equipment and a large number of possible points of failure. Additionally, the long residence time of over 2 h requires either a low total flow rate, which limits the rate of production, or a large total reactor volume, which could lead to a large hydraulic resistance and thus require more powerful (and expensive) pumps. Furthermore, a long residence time makes it more time-consuming to evaluate different reaction conditions.

It is preferable to have a simpler reactor using fewer components and the shortest residence time possible, like the one shown in Figure 3.2. In this reactor the EG is not pre-heated for 1 h, reducing the residence time from 1 to 2 h and, instead of injecting each precursor individually, the precursors are mixed and loaded into a single syringe. The carrier liquid and precursor are injected from two separate pumps into a two-in-one-out junction to produce a segmented flow. The segmented flow enters a heated coil at 160 °C for 1 h, where the reaction takes place. The product is collected at the outlet. In addition to the shorter residence time, this reactor uses only two pumps and one junction.

Based on published reports of AgNW syntheses, these simplifications were considered unlikely to adversely affect the reaction. The first reports of the polyol synthesis of AgNWs did not involve pre-heating of the EG.[51,53,54] Other reports where pre-heating was used suggested it was necessary to remove trace water,[60,61] or used it without comment.[65,74] As discussed in Section 2.6.2, Skrabalak and co-workers suggested that heating EG in air results in its oxidation to GA, which then reduces the $AgNO_3$.[79] (Although Korte

et al. noted that the pre-heating time could be reduced from 1 h to 10 min when O_2 was *excluded* from the reaction using an Ar atmosphere.[65]) If this is indeed the case then pre-heating the EG for 1 h prior to the addition of the precursors should generate more GA and result in a higher initial reduction rate of $AgNO_3$. Therefore, without pre-heating the initial reduction rate should be lower, potentially leading to the nucleation of fewer particles that can then grow into longer wires (as discussed in Section 2.4). Taken together, these reports strongly suggest that pre-heating is unnecessary and hence may be omitted in flow.

The viability of combining all the precursors into a single syringe was less certain. Batch heat-up routes combine all the precursors into a single mixture, but they are heated and used immediately. It is unclear whether such a mixture would be stable in a syringe over an extended period of time, as NaCl and $AgNO_3$ might react to form AgCl, and PVP has also been shown to slowly reduce $AgNO_3$.[83] Precursor stability is a key requirement for a flow synthesis, if unwanted product variation is to be avoided. The next section describes the investigation into the viability of these simplifications using the batch method.

3.2 Heat-up versus hot-injection

In order to establish whether the above modifications were acceptable, the synthesis reported by Bergin and co-workers was modified for a heat-up procedure. All of the reactants used in the original hot-injection method were added to a flask at room temperature. The flask was then immersed in an oil bath set to 170 °C, causing the reaction mixture to reach a measured temperature of 160 °C after approximately 10 min. Bergin's hot-injection method was used as a control, and included 1 h of pre-heating. Both reactions were carried out simultaneously in the same oil bath and used the same stock solutions.

No changes were observed during pre-heating. Upon injection of the $AgNO_3$ solution to the hot EG ($t = 0$), the reaction mixture immediately turned yellow, consistent with the formation of Ag nanoparticles. At $t =$

2 min, the reaction mixture turned orange and gradually darkened in colour to become brown. At $t = 8$ min, the product was greenish-grey. No further colour changes were observed. At $t = 13$ min, gas started to gently bubble from the reaction mixture at a rate of a few bubbles per second.

For the heat-up reaction, the flask was placed into the oil bath ($t = 0$) and gradually turned yellow over the course of a minute. The yellow colouration was paler than for the hot-injection reaction, which suggested that the rate of production of Ag nanoparticles was lower. This was expected as the reaction mixture was heated up from room temperature and was therefore colder than the hot-injection reaction at the same time. The reaction mixture had a cloudy appearance and gradually turned yellow-brown by $t = 8$ min. At $t = 10$ min, the reaction mixture was greenish-grey and at $t = 16$ min it had a turbid appearance. Compared to the hot-injection control, the heat-up reaction mixture was a lighter grey. No gas evolution was observed.

3.2.1 Analysis using dark field optical microscopy

Aliquots of reaction mixture were removed from both reactions using a Pasteur pipette at $t = 13$ min, 16 min, and 20 min, and quenched in room temperature water. Each crude sample was drop-cast onto a glass microscope slide and examined using DFOM (Section 5.4.3). Figure 3.3 shows the images recorded. The first row shows images of samples removed from each flask at $t = 13$ min, when the hot-injection reaction mixture had become turbid. The nanowires from the heat-up reaction were clearly shorter and fewer in number (relative to the number of nanoparticles) than those produced in the hot-injection reaction. The second row shows DFOM images of samples removed at $t = 16$ min. The nanowires from the hot-injection reaction were approximately the same length as those obtained at $t = 13$ min, but those from the heat-up reaction were nearly twice as long as they had been only 3 min earlier. The bottom row shows the samples at $t = 20$ min. Only the nanowires from the heat-up reaction had continued to grow. Overall, the heat-up method had produced longer nanowires. The images indicated that the heat-up reaction beneficially yielded a smaller number of nanoparticles

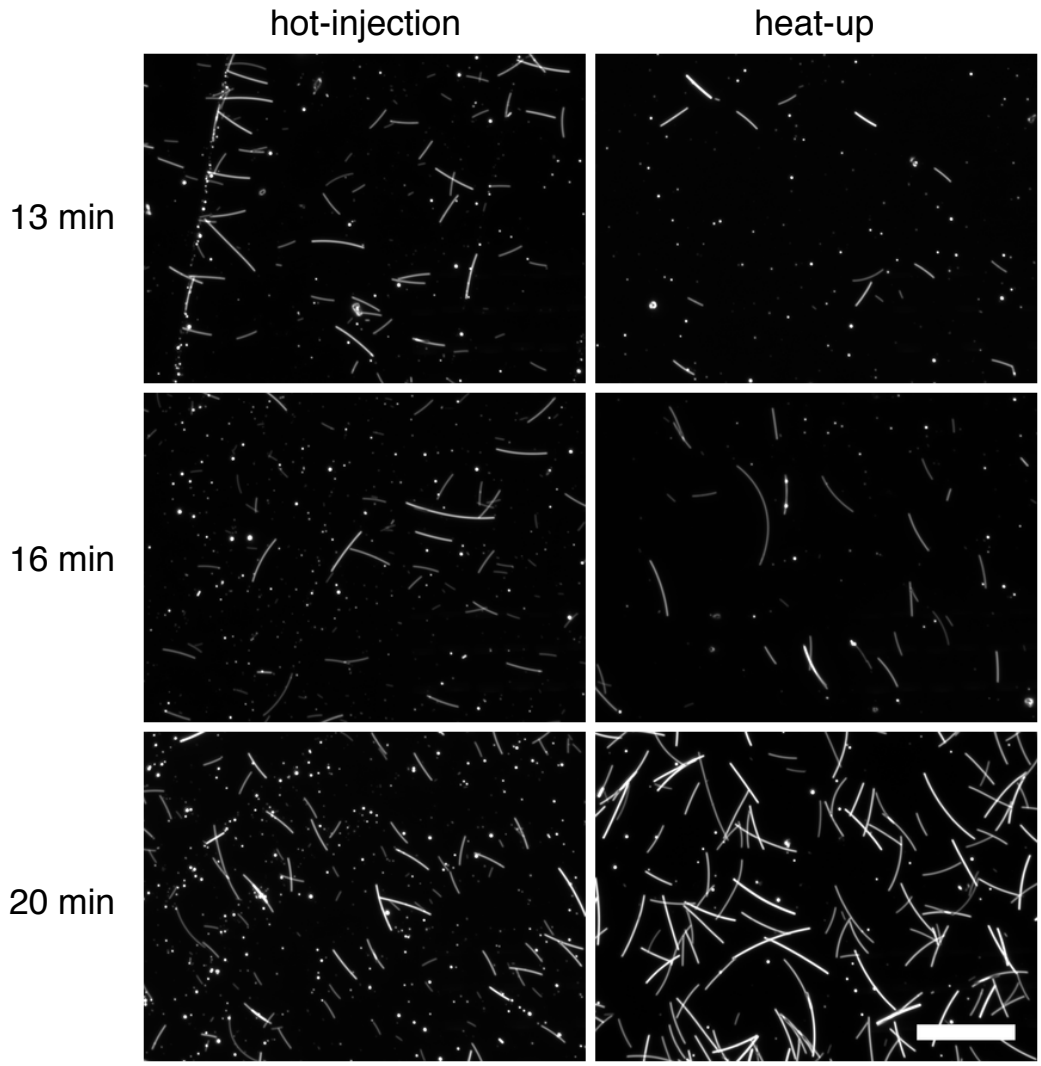


Figure 3.3 – DFOM images of samples removed from the hot-injection (left) and heat-up (right) reactions at $t = 13\,\text{min}$, $16\,\text{min}$, and $20\,\text{min}$. Scale bar: $20\,\mu\text{m}$.

relative to the number of nanowires.

In order to more precisely describe the relationship between nanowire length and reaction time for each method, 30 nanowires from each DFOM image were randomly selected and measured using computer software. Figure 3.4 shows histograms of the frequencies of the measured lengths, with the median length shown inset.[a] The top and bottom row show the samples from the hot-injection and heat-up reactions, respectively. At $t = 13\,\text{min}$, the hot-injection and heat-up reactions had produced nanowires of similar lengths, with median lengths of 4.8 µm and 4.4 µm, respectively. At $t = 16\,\text{min}$, the median length of the hot-injection reaction decreased by nearly half from 4.8 to 2.7 µm, whereas the median length of the heat-up reaction increased from 4.4 to 6.7 µm. By $t = 20\,\text{min}$, growth of the nanowires in the hot-injection reaction had re-started to give a median length of 4.1 µm (although this was still 15 % shorter than the median length of 4.8 µm at $t = 13\,\text{min}$). In contrast, the nanowires in the heat-up reaction continued growing and had reached a median length of 9.1 µm.

The decrease in the median length observed during the hot-injection reaction has been attributed to etching of the AgNWs by nitric acid (HNO_3), a by-product of the reduction of $AgNO_3$. Bergin *et al.* proposed that if GA is responsible for the reduction of $AgNO_3$ then:[74]

$$2\,AgNO_3 + HOCH_2CHO + H_2O \longrightarrow HOCH_2COOH + 2\,Ag + 2\,HNO_3 \quad (3.1)$$

HNO_3 then oxidises elemental Ag (including AgNWs) to produce $AgNO_3$ and nitric oxide (NO) gas as a by-product. This explanation is consistent with the gas evolution seen from the hot-injection reaction mixture between 13 and 16 min when the AgNWs were observed to decrease in length.

$$4\,HNO_3 + 3\,Ag \longrightarrow 3\,AgNO_3 + NO\uparrow + 2\,H_2O \quad (3.2)$$

This reaction produces the starting material $AgNO_3$, which is once again available for reduction and growth, as demonstrated by the increase in me-

[a] The median was chosen over the mean because the median is less sensitive to outliers.[84]

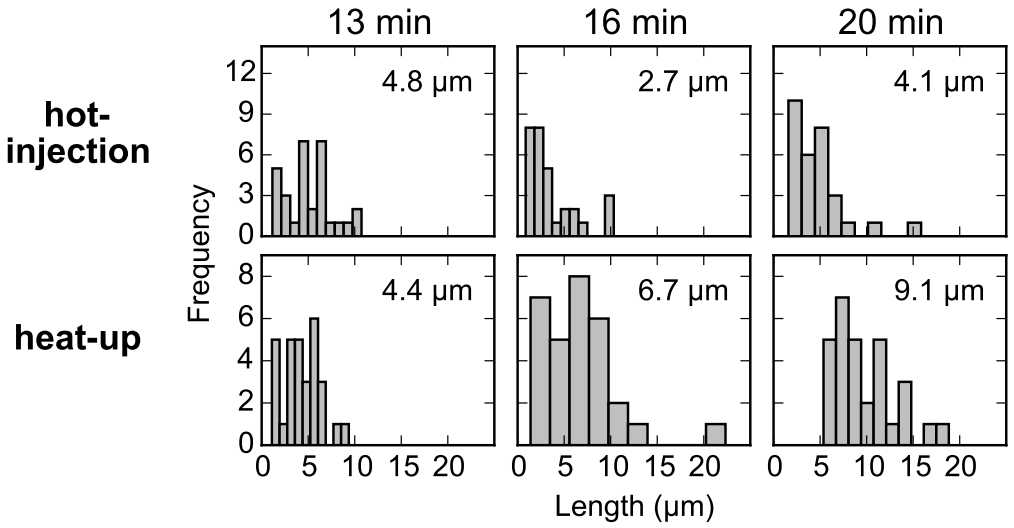


Figure 3.4 – Histograms showing the frequency of AgNW lengths measured from the DFOM images of samples removed from the hot-injection (top row) and heat-up (bottom row) reactions at $t = 13\,\text{min}$, 16 min, and 20 min. Inset to each histogram is the median length.

dian length between $t = 16\,\text{min}$ and $t = 20\,\text{min}$.

The histograms in Figure 3.4 also show that short AgNWs (<5 µm) are always present in the hot-injection reaction, with the frequency of short AgNWs increasing as the reaction progresses. For the heat-up reaction, no AgNWs less than 5 µm long were recorded at $t = 20\,\text{min}$. It is reasonable to infer that nucleation occurs throughout the hot-injection reaction, whereas it stops earlier in the heat-up method, leading to reduced polydispersity.

Lastly, the AgNWs produced by both methods compare favourably to those reported by Bergin *et al.* At the same temperature (160 °C), the authors produced AgNWs of length 7.4 µm after a reaction time of approximately 2 h. With a 20 min reaction time, they obtained AgNWs of length 2.5 µm. (They did not specify the length referred to the mean length or another statistic.) In comparison, the hot-injection and heat-up methods in this work produced AgNWs with median lengths of 4.1 µm and 9.1 µm, respectively.

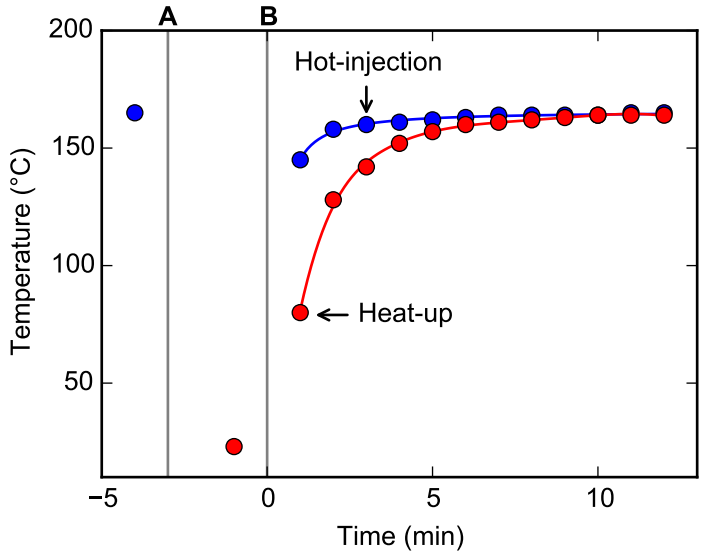


Figure 3.5 – Graph showing the temperature of the reaction mixtures over time for the hot-injection and heat-up methods. **A** marks the time at which NaCl solution was added to the hot-injection reaction, followed by the $Fe(NO_3)_3$ and PVP. **B** marks the time at which $AgNO_3$ was added to the hot-injection reaction and the heat-up reaction mixture was immersed into the oil bath.

3.2.2 Temperature profile comparison

In order to monitor the temperature rise in the two methods, a thermometer was inserted into each reaction mixture and the temperature was recorded at regular intervals, see Figure 3.5. After pre-heating for 1 h, the EG for the hot-injection reaction had reached a steady temperature of 163 °C. Room temperature solutions of NaCl, $Fe(NO_3)_3$, and PVP were then added to the hot EG one after the other, marked on Figure 3.5 by **A**, causing the temperature of the reaction mixture to decrease. The addition of the $AgNO_3$ solution at $t = 0$ min is marked by **B**. After the addition of the $AgNO_3$ ($t = 1$ min), the temperature was 145 °C and steadily increased to 165 °C at $t = 12$ min. For the heat-up reaction, the solutions were added to the flask at 23 °C (**A**). The flask was then immersed into the hot oil bath at $t = 0$ (**B**). At $t = 1$ min, the temperature was 80 °C, 65 °C lower than the hot-injection reaction mixture at that point in time. It then took 6 min for the heat-up reaction mixture to reach 160 °C, whereas the hot-injection reaction mixture took only 3 min.

It is reasonable to conclude that the higher temperature of the hot-injection reaction resulted in a higher rate of reduction of $AgNO_3$ and therefore a higher nucleation rate and the formation of more nuclei, leaving fewer moles of Ag available for seed growth and so yielding shorter AgNWs. In contrast, in the heat-up reaction fewer seeds were nucleated leaving more Ag available for their growth into longer AgNWs.

3.2.3 Conclusions

The heat-up method produced AgNWs over twice as long as those produced by the hot-injection method and resulted in better shape-selectivity. Additionally, the difference in temperature profile for the heat-up and hot-injection methods suggested that using a single temperature zone for the entire flow reactor would be sub-optimal. If the results reported here were shown to be consistently true, we would conclude that pre-heating is not a pre-requisite for AgNW formation and that it should be possible to omit the pre-heating stage in flow and combine the precursors into a single syringe

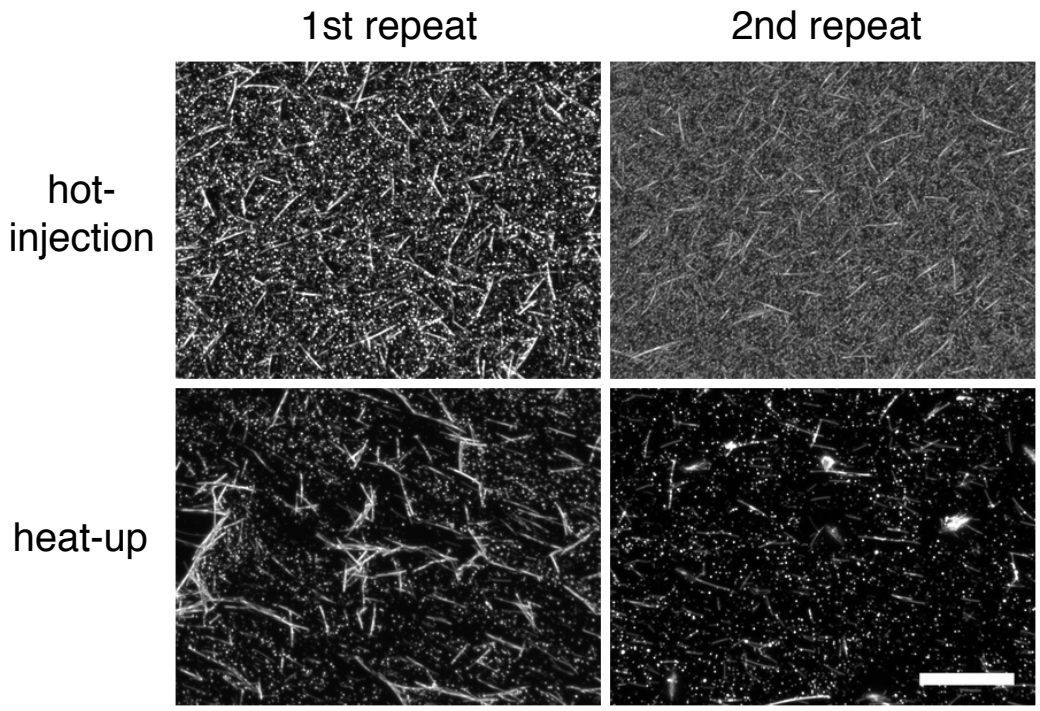


Figure 3.6 – DFOM images of samples taken at $t = 15\,\text{min}$ from two repeats of the hot-injection and heat-up syntheses. The images are representative of the product of obtained from the reactions that failed to reproduce the results in Section 3.2. Scale bar: 20 µm.

held at room temperature (subject to the precursor being chemically stable over time). However, as is discussed in the next section, these results could only be reproduced after thorough and comprehensive investigation into the procedure.

3.3 Irreproducibility of batch synthesis

The repeat reactions following the reactions reported in Section 3.2 did not produce the same results. Figure 3.6 shows DFOM images of samples taken at $t = 15\,\text{min}$ from two of the repeat reactions. These are typical of the product that was obtained. The DFOM images showed that both methods now produced a large number of nanoparticle by-products, particularly in the hot-injection reaction, and that the AgNWs were short, polydisperse,

and not as wire-like as those in Figure 3.3.

We concluded that either the results in Section 3.2 were anomalous or that an unknown experimental parameter had significantly changed after the reactions in Section 3.2. Since the results in Section 3.2 were an improvement over results in the literature and also relevant to future reactions in flow, it was desirable to identify the cause of the anomaly or the parameter that had changed that had led to the change in the product.

To do this, I undertook a comprehensive examination of the entire experimental procedure. Figure 3.7 shows a cause-and-effect diagram displaying all possible factors that might affect the product of the reaction. Cause-and-effect diagrams are a commonly-used tool for isolating the cause of process failures.[86] For clarity, possible causes are grouped into one of five categories: reagents and materials, equipment, environment, experimental procedure, and product analysis.

Sample analysis errors were considered the least likely cause as the difference in product morphology would not be explained by use of the wrong microscope objective. Regardless, care was taken to ensure that the correct microscope objective and associated calibration data were used. The spatial calibration was also checked periodically for correctness and no variation was observed.

It was not possible to precisely control the laboratory environment. However, small variations in humidity or temperature were considered unlikely to affect the reaction so dramatically. Light-induced nucleation of $AgNO_3$ solutions was prevented by wrapping the containers in aluminium foil.

Causes related to the experimental procedure were controlled by taking particular care to carry out the same procedure for every experiment. Glassware contamination was prevented by following a rigorous cleaning procedure (Section 5.2.1). Causes due to the equipment were eliminated by using the same hot plate, thermocouple probe, oil bath, and Eppendorf pipettes for all experiments. With those causes controlled for, or thought unlikely, only pipetting errors and reagent contamination remained as probable causes of the failure of the synthesis.

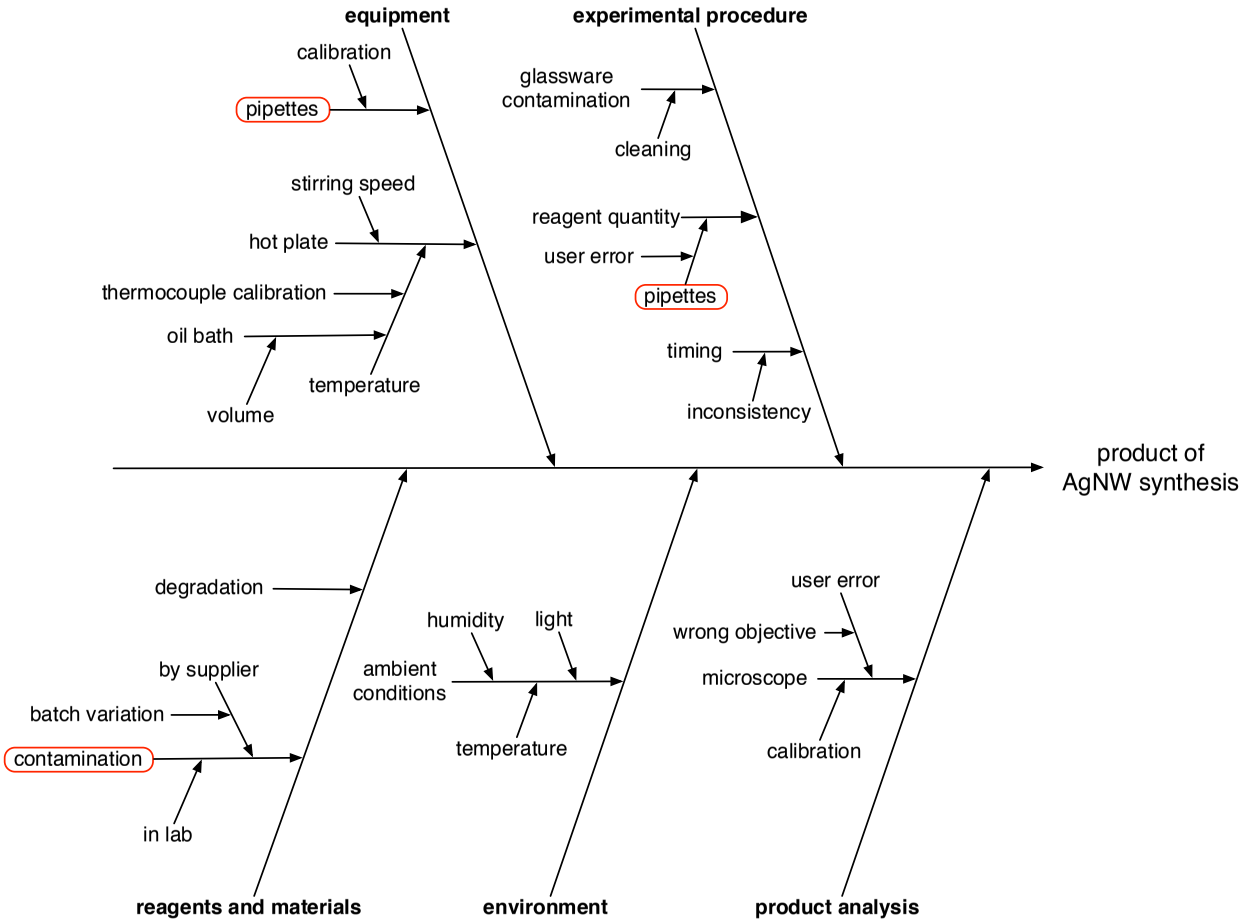


Figure 3.7 – Cause-and-effect diagram showing factors that might affect the product of the AgNW synthesis. Circled in red are the causes not eliminated by either their low likelihood or experimental design.

$V_{\max}$ (µL)	V_{nom} (µL)	$\bar{V}$ (µL)	e_V (%)	s_V (µL)	$s_V/\bar{V}$ (%)
20	10	9.887	-1.1	0.5894	5.9
	20	20.02	-0.1	0.5139	2.6
5000	840	848.9	1.1	43.41	5.2
	2075	2083	0.4	13.39	0.6
	5000	4995	-0.1	45.17	0.9

Table 3.1 – Table showing the results of the gravimetric analysis of the pipetting used in the heat-up and hot-injection AgNW syntheses. $V_{\max}$ is the maximum volume of the pipette, V_{nom} is the nominal volume, $\bar{V}$ is the mean of dispensed volume, e_V is the systematic error ($e_V = (\bar{V} - V_{\text{nom}})/V_{\text{nom}}$), s_V is the sample standard deviation, and $s_V/\bar{V}$ is the CV.

3.3.1 Pipetting errors

Pipette calibration errors would lead to a systematic error. The pipettes used were calibrated yearly, but unknown damage to a pipette (e.g. by it being dropped) could affect the calibration and lead to the sudden failure of the reactions. There is also a random error component in the volume of liquid dispensed, which increases in magnitude with poor pipetting technique. Pipette manufacturers specify limits for systematic and random errors (when the pipette is used correctly). As a first investigation, the accuracy and precision of the pipetting used in the hot-injection and heat-up syntheses was examined using gravimetric analysis. Gravimetric analysis involves dispensing a sample of liquid from the pipette under test into a vessel placed on an analytical balance. The actual volume dispensed by the pipette under test is calculated by dividing the mass of the dispensed liquid by its density.

Since EG was the liquid dispensed in the reaction, it was also used for the analysis. Each dispensed volume used in the synthesis was tested: 10 µL and 20 µL dispensed from a 20 µL pipette, and 840 µL, 2075 µL, and 5000 µL dispensed from a 5 mL pipette. Ten pipette tips were each tested three times to give a total of 30 measurements for each nominal (dispensed) volume V_{nom}. Changes in the density of EG (1.11 g/mL) due to temperature variation were considered negligible over typical laboratory temperatures ($< 0.5\,\%$ over 15 to 25 °C).[87]

Table 3.1 shows the results of the gravimetric analysis. It shows the volume of the pipette $V_{\max}$ used for the test, V_{nom}, and the corresponding mean dispensed volume $\bar{V}$, systematic error e_V, standard deviation s_V and CV $s_V/\bar{V}$. In all cases the systematic error was small and fell within the limits specified by the manufacturer. However, some of the random errors were large and exceeded the manufacturer's limits. For the 20 µL pipette with $V_{\text{nom}} =$ 10 µL and 20 µL, the CVs were 5.9 % and 2.6 % respectively (compared to a maximum of ±0.6 % and ±0.3 %, respectively, specified by the manufacturer). This pipette was used to add stock solutions of NaCl and $Fe(NO_3)_3$ the reaction mixtures, and therefore these results suggested there was a large variation in the concentration of these compounds between reactions. In a worst case scenario (where the volume dispensed $V = V_{\text{nom}} \pm 2s_v$), the final concentration of NaCl and $Fe(NO_3)_3$ in the reaction mixture would deviate from the desired concentration by ±5.2 % and ±11.8 %, respectively.

The CV for the three nominal volumes used with the 5 mL pipette all exceeded the manufacturer's limits. When $V_{\text{nom}} = 840$ µL, the CV was 5.2 % (compared to a limit of ±0.6 % for $V_{\text{nom}} = 500$ µL). When the pipette was used at full capacity ($V_{\text{nom}} = 5000$ µL), the CV was ±0.9 % (compared to a limit of 0.15 % for $V_{\text{nom}} = 5000$ µL). Both of these nominal volumes were used to add EG to the reaction flask. Thus the random error would alter the overall concentration of all the species in the reaction. In a worst case scenario, the total volume and overall concentration of all species would deviate from the desired concentration by ±2.3 %.

Lastly, the 5 mL pipette was used to add 2075 µL $AgNO_3$ solution and 2075 µL PVP solution to the reaction mixture. For this nominal volume the CV was ±0.6 % (compared to a limit of ±0.25 % for $V_{\text{nom}} = 2500$ µL). In a worst case scenario, the concentration would have deviated ±10.4 % from the desired concentration.

3.3.2 Minimisation of pipetting errors

Gravimetric analysis established that there was significant random variation in the volume of EG and of each precursor added to the reactions. This could

	(a) Original		(b) Modified		
Compound	c (M)	V (mL)	c (mM)	V (mL)	c_f (mM)
EG	—	15.84	—	0	—
NaCl	0.220	0.02	8.80	0.5	4.40×10^{-3}
$Fe(NO_3)_3$	2.00×10^{-2}	0.01	0.401	0.5	2.00×10^{-4}
PVP	0.378	2.075	82.5	9.51	0.784
$AgNO_3$	0.247	2.075	53.9	9.51	0.513
Total	—	20.02	—	20.02	—

Table 3.2 – Table concentration of the stock solutions c and corresponding volume V added to the reaction mixture for the (a) original and (b) modified batch procedure. c_f shows the final concentration in the reaction mixture, which is the same for (a) and (b).

have caused the anomalous results described in Section 3.2. Following these findings, the experimental procedure was modified to reduce the random error. This would minimise the batch-to-batch variation in concentration of the precursors, and could lead to the identification of the cause of the change in product.

Table 3.2 shows the volume V of each solution added to the reaction and the concentration c of the stock solutions for the original (a) and modified procedure (b). The last column shows the final concentration c_f of each species in the reaction mixture, and is (intentionally) the same for both procedures.

In the original procedure, 15.84 mL neat EG was added to the flask. Relatively small—and hence imprecise—quantities of NaCl (20 µL) and $Fe(NO_3)_3$ (10 µL) were then added to the neat EG. PVP and $AgNO_3$ (2.075 mL) were added from a 5 mL pipette, using less than half of the capacity of the pipette.

Larger volume pipettes are more precise than smaller volume pipettes, and a pipette is most precise when it at least half full ($V_{\text{nom}}/V_{\text{max}} \geq 0.5$). Therefore the procedure was modified so that neat EG was no longer added. The other precursors were then diluted, and the volume added increased, so that the total reaction volume and concentration of each species was unchanged. Furthermore, the dilution factors were chosen so that the volume

$V_{\max}$ (µL)	V_{nom} (µL)	$\bar{V}$ (µL)	e (%)	s_V (µL)	$s_V/\bar{V}$ (%)
1000	500	496.3	-0.7	2.244	0.4
5000	4755	4763	0.2	12.98	0.3

Table 3.3 – Table showing the results of the gravimetric analysis of the pipetting used in the modified AgNW synthesis. $V_{\max}$ is the maximum volume of the pipette, V_{nom} is the nominal volume, $\bar{V}$ is the mean of dispensed volume, e_V is the systematic error ($e_V = (\bar{V} - V_{\text{nom}})/V_{\text{nom}}$), s_V is the sample standard deviation, and $s_V/\bar{V}$ is the CV.

required could be dispensed from a pipette that was at least half full and also to minimise the number of pipetting steps (with the pipettes available in the laboratory).

The volume of NaCl solution added was increased by a factor of 25 from 20 to 500 µL. The volume of $Fe(NO_3)_3$ solution added was also increased to 500 µL, equal to a 50-fold increase from 10 µL. So that the final concentrations were unchanged, the NaCl and $Fe(NO_3)_3$ stock solutions were diluted by a factor of 25 and 50, respectively. Both of these precursors could then be added to the reaction using a 1 mL pipette. The PVP and $AgNO_3$ solutions were diluted by a factor of 4.58, so that the volume of each solution added increased from 2.075 to 9.51 mL. 9.51 mL could be added using two additions of 4.755 mL from a 5 mL pipette.

In addition to these changes to precursor solutions, the reverse pipetting technique was adopted (see Section 5.4.1). Reverse pipetting is recommended by manufacturers over standard forward pipetting when pipetting viscous liquids like EG, and offers better reproducibility.

The accuracy and precision of this method was then assessed using gravimetric analysis. Table 3.3 shows the results. The systematic errors were all small (<1 %), which is expected since the same pipettes were used as in Section 3.3.1. The modifications were successful as the random errors were all small: 0.4 % and 0.3 % for dispensed volumes of 500 µL ($V_{\max}$ = 1 mL) and 4755 µL ($V_{\max}$ = 5 mL), respectively. These did lie outside the manufacturer's random error limits (±0.2 % and ±0.25 %, respectively), but only by a fraction of a percent. This is probably due to the high viscosity of

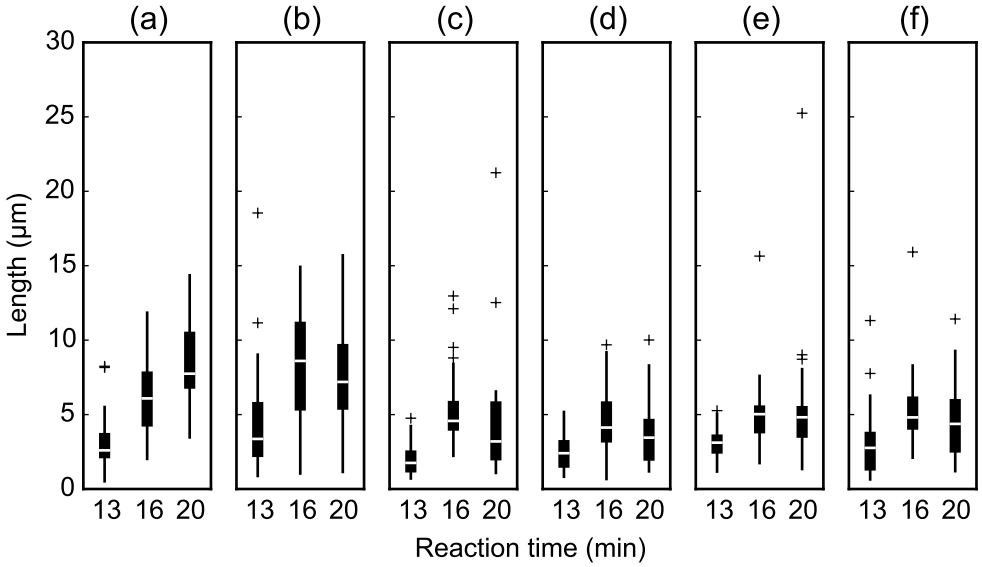


Figure 3.8 – Box and whisker plots of the lengths of AgNWs removed from repeat heat-up reactions (a–f) at $t = 13\,\text{min}$, 16 min, and 20 min using the modified pipetting method.

EG compared to water, which is normally used for calibration. The modified method was still a significant improvement over the original method in terms of precision and experimental simplicity.

3.3.3 Testing the modified method

Following these changes to the experimental method, the heat-up reaction was repeated to establish whether the product of the reaction and also the batch-to-batch reproducibility were affected. As before, samples were taken at $t = 13\,\text{min}$, 15 min, and 20 min, and examined using DFOM. The length of 30 nanowires was measured from each sample. Figure 3.8 (a) shows three box and whisker plots of the nanowire lengths obtained from DFOM images of each sample. (See Appendix A.1 for a description of the key features of a box and whisker plot.) The median length gradually increased from 2.6 µm at $t = 13\,\text{min}$, to 6.1 µm at $t = 16\,\text{min}$, and finally to 7.8 µm at $t = 20\,\text{min}$. These values are in good agreement with the results from Section 3.2.

To establish the reproducibility of the method, repeat reactions were nec-

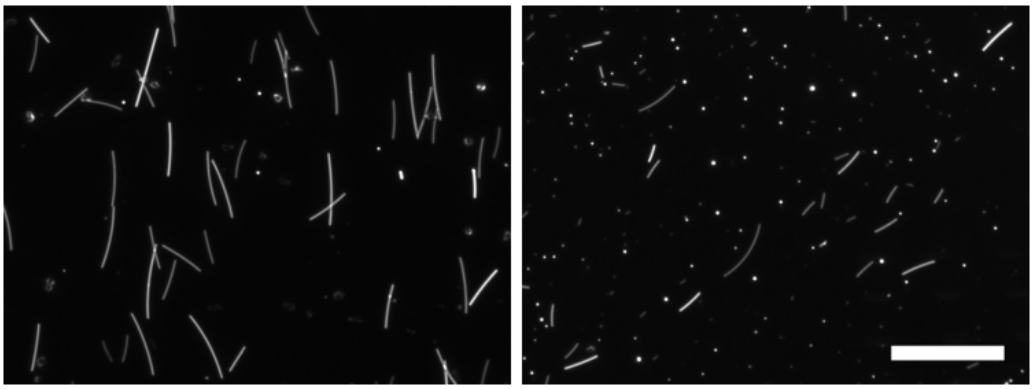


Figure 3.9 – DFOM images of samples removed at $t = 20\,\text{min}$ from reactions (a, left) and (f, right). Scale bar: 20 µm.

essary. Figure 3.8 (b) shows the results from the first repeat. A different trend was observed, where the median length was 3.36 µm at $t = 13\,\text{min}$, increased to a maximum of 8.60 µm at $t = 15\,\text{min}$, but then decreased to 7.19 µm at $t = 20\,\text{min}$. Figure 3.8 (c) shows the results from the second repeat, which show a significantly different trend of median length versus time. At $t = 13\,\text{min}$ the median length was only 1.8 µm. The AgNWs then grew, leading to an increase in the median to 4.6 µm at $t = 16\,\text{min}$, but the median then decreased in length to 3.2 micron at $t = 20\,\text{min}$.

Because of the significant variation between these reactions (a–c), the reaction was repeated a further three times. The results are shown in Figure 3.8 (d–f). The final four reactions (c–f) shared a similar trend and produced nanowires with a median length 3.5 µm, 4.8 µm, and 4.4 µm at $t = 20\,\text{min}$, respectively. Taken together, the results in Figure 3.8 show a marked change in the trend of nanowire length over time between reactions (b) and (c), with a signifiant deterioration in nanowire length over the course of the set of measurements. This difference can be clearly seen in the DFOM images of the final samples from reactions (a) and (f) shown in Figure 3.9. These results suggested that another uncontrolled factor had changed and adversely affected the reaction.

3.3.4 Effect of ethylene glycol lot number

The only causes in Figure 3.7 that had not been investigated were those related to the reagents and materials. The same stock solutions of $Fe(NO_3)_3$ and NaCl were used for reactions (a-f). The PVP solution ran out after reaction (b), so a new solution was prepared and used in reaction (c) onwards. These solutions were the same concentration to within experimental error (82.3 mM and 82.5 mM). Both solutions were made from the same bottle of PVP, but the EG was taken from two different bottles. The bottles contained the same product from the same supplier, but inspection revealed that they had different lot numbers. For reactions (a) and (b) the PVP solution was prepared using EG from lot BCBN5970V, but for reactions (c–f) the PVP solution was prepared using EG from lot BCBN2592V. Henceforth, lot BCBN5970V and lot BCBN2592V are referred to as lot A and lot B, respectively. As discussed in Section 2.6.1, EG has been reported to have varying concentrations of ionic species that can affect the reaction. It was thought possible that the two lots contained substantially different concentrations of impurities that then affected nanowire growth.

$AgNO_3$ solutions were prepared as required because they turned yellow overnight, indicating the formation of silver nanoparticles. Coincidentally, the $AgNO_3$ solutions were made using EG from the same lot number as the EG used to prepare the PVP solutions. The same stock solutions of $Fe(NO_3)_3$ and NaCl, prepared using EG from lot A, were used for all reactions. Therefore reactions (a–b) were prepared entirely with EG from lot A, whereas reactions (c–f) were 5% lot A and 95% lot B by volume.[b] This suggested that reactions carried out in EG from lot A produce longer nanowires than reactions carried out in EG from lot B.

To establish the reproducibility and size of the effect of the EG lot on AgNW length, repeat reactions were carried out where the lot used for the $AgNO_3$ and PVP solutions was changed. An additional three reactions using EG from lot A (g–i) and a single reaction using EG from lot B (j) were

[b]The $Fe(NO_3)_3$ and NaCl solutions accounted for 5% of the total reaction volume (see Table 3.2).

		Length (µm)	
Reaction	Lot	Median	SD
a	A	7.75	2.73
b	A	7.19	3.30
c	B	3.20	4.03
d	B	3.45	2.16
e	B	4.82	4.25
f	B	4.37	2.54
g	A	10.76	3.30
h	A	9.89	3.85
i	A	9.46	4.75
j	B	6.74	2.66

Table 3.4 – Table showing for reactions (a–k) the lot number of the EG used to prepare the PVP and $AgNO_3$ solutions and the median length and SD at $t = 20\,\text{min}$.

carried out so that there was a total of five reactions for each lot. The lot and the median length and standard deviation (SD) at $t = 20\,\text{min}$ for all the reactions (a–j) are tabulated in Table 3.4.

Figure 3.10 shows box and whisker plots of the nanowire length for samples removed from reactions (g–j) at $t = 13\,\text{min}$, 16 min, and 20 min. Reactions (g–i) used EG from lot A. For (g), the median length was 3.95 µm after $t = 13\,\text{min}$. It steadily increased to 8.82 µm by $t = 16\,\text{min}$ and to a maximum of 10.8 µm by $t = 20\,\text{min}$. A similar trend was observed for (h). At $t = 13\,\text{min}$ the median length was 4.12 µm and increased to 8.44 µm at $t = 16\,\text{min}$. At $t = 20\,\text{min}$ the AgNWs had a median length of 9.89 µm. Unexpectedly, no anisotropic particles were observed using DFOM in reaction (i) at $t = 13\,\text{min}$. They were observed three minutes later at $t = 16\,\text{min}$ with a median length of 3.46 µm, which was similar to the samples removed at $t = 13\,\text{min}$ for reactions (g) and (h). They grew to a median length of 9.46 µm by $t = 20\,\text{min}$. For (j), which used EG from lot B, a different trend was observed. At $t = 13\,\text{min}$ the median length was 1.96 µm. By $t = 16\,\text{min}$ the median length had reached a maximum of 6.98 µm, and then decreased to 5.73 µm for the final sample removed at $t = 20\,\text{min}$.

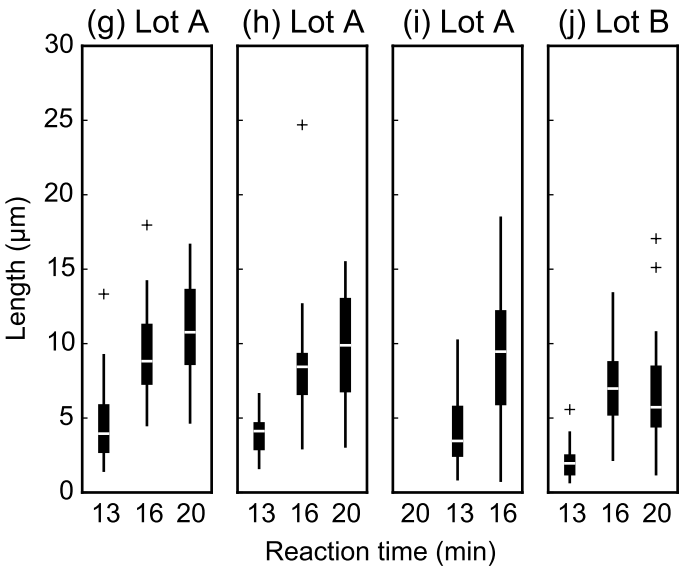


Figure 3.10 – Box and whisker plots showing the length of AgNWs removed from the reaction mixture at $t = 13\,\text{min}$, 16 min, and 20 min for reactions (g–j). For (i), no box plot is shown at $t = 13\,\text{min}$ because no nanowires were seen using DFOM.

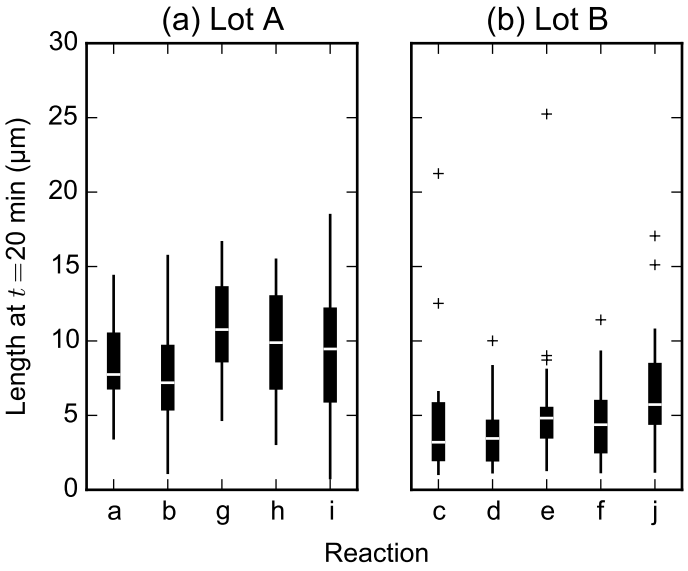


Figure 3.11 – Box and whisker plots showing the length of AgNWs measured in the sample removed at $t = 20\,\text{min}$ from reactions (a–j), grouped by (a) lot A and (b) lot B.



Figure 3.12 – Photograph of a vial of AgNWs dispersed in water.

Figure 3.11 shows box and whisker plots of the length of AgNWs measured from samples removed at $t = 20\,\text{min}$ for all reactions (a–j). Reactions using the same lot of EG are grouped together, showing EG lot A and B in Figure 3.11 (a) and (b), respectively. There is a clear difference in the length of the AgNWs produced using each lot: AgNWs grown in lot A have a larger median length than AgNWs grown in lot B. The median length for all reactions using lot A was 9.02 µm, compared to 4.41 µm using lot B. (The mean length and standard deviation were 9.15 µm and 3.78 µm, respectively, for lot A, and 4.94 µm and 3.52 µm, respectively, for lot B.)

In conclusion, AgNWs grown using EG from lot A were approximately twice as long as those grown in EG from lot B, and the switch to EG from the former to latter lot number is likely to have caused the sudden degradation in the performance of the synthesis. It was not caused by poor precision in pipetting, although the improvements in the experimental method simplified the procedure and will also have improved its batch-to-bath reproducibility.

3.3.5 Electron microscopy analysis

The AgNWs produced using each lot of EG were analysed using SEM in order to determine the diameter of the AgNWs and also validate the length

measurements made using DFOM. Specimens for SEM must be electrically conductive, so the insulating PVP surfactant was removed from the surface of the AgNWs by adding acetone to the crude product mixture. The AgNWs precipitated out and were were isolated by centrifugation and redispersed in water, producing a turbid, grey solution (Figure 3.12). The suspension was then drop-cast onto a conductive silicon substrate for SEM and a glass microscope slide for DFOM, so that the two analysis techniques could be compared.

Figure 3.13 shows SEM micrographs of the AgNWs. The left and right hand side show micrographs of washed AgNWs synthesised in EG from lot A (reaction (h)) and lot B (reaction (i)) respectively. The top row shows low magnification micrographs for length measurements, whilst the bottom row shows high magnification micrographs for diameter measurements. The top-left micrograph of the product from lot A shows AgNWs with a small number of isotropic nanoparticles as a by-product. In comparison, the top-right micrograph of the product grown in lot B shows a larger number of isotropic nanoparticles relative to the number of AgNWs. Figure 3.14 shows DFOM images of the same washed samples. Again, the images show that there were fewer nanoparticle by-products using lot A compared to lot B.

The diameter of 50 AgNWs from each lot was measured from the high magnification SEM micrographs. These are shown in the histograms in Figure 3.15. For lot A, the mean average diameter $\bar{d} = 52\,\text{nm}$ and SD $s = 10\,\text{nm}$. For lot B, $\bar{d} = 43\,\text{nm}$ an $s = 11\,\text{nm}$. Therefore the AgNWs grown in lot A are 26 % thicker than those grown in lot B. The smaller CV for lot A ($s/\bar{d} = 0.19$) compared to lot B ($s/\bar{d} = 0.26$) shows that the diameters of AgNWs from lot A are slightly less polydisperse than the AgNWs from lot B.

The length of 100 AgNWs was also measured from the low magnification SEM and DFOM micrographs in Figure 3.13 and Figure 3.14. Figure 3.16 shows histograms of the lengths for each lot and imaging method, with the vertical red lines indicating the mean average length of each sample. The median, mean, and SD are shown in Table 3.5. Using SEM, the median length of the AgNWs grown in lot A (7.66 µm) was 18 % longer the median length for AgNWs grown in lot B (6.51 µm). Similarly, the mean length for

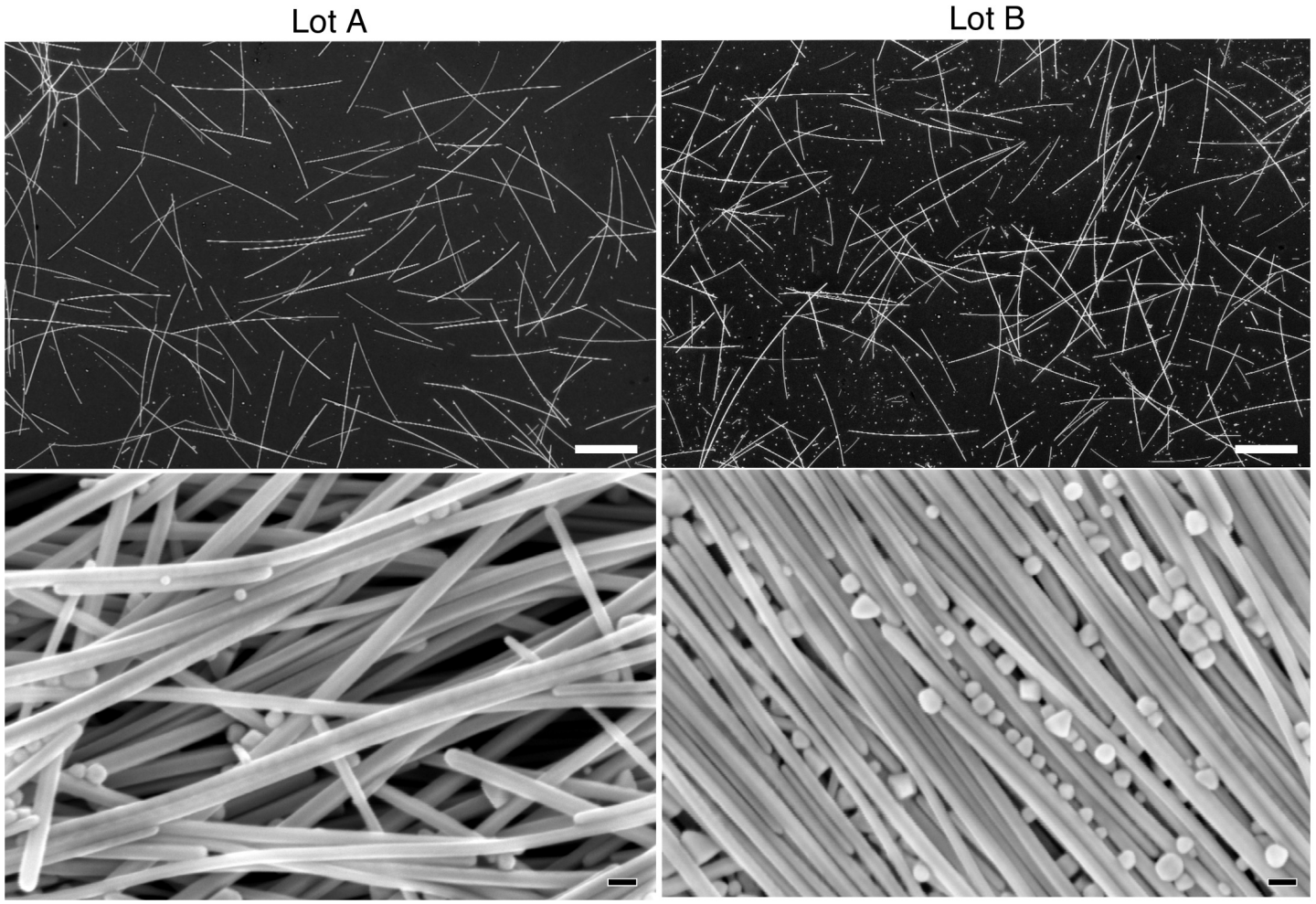


Figure 3.13 – SEM images of samples of AgNWs grown in EG from lot A (left, reaction (i)) and lot B (right, reaction (j)) at low (top) and high (bottom) magnifications. Top scale bars: 5 µm. Bottom scale bars: 100 nm.

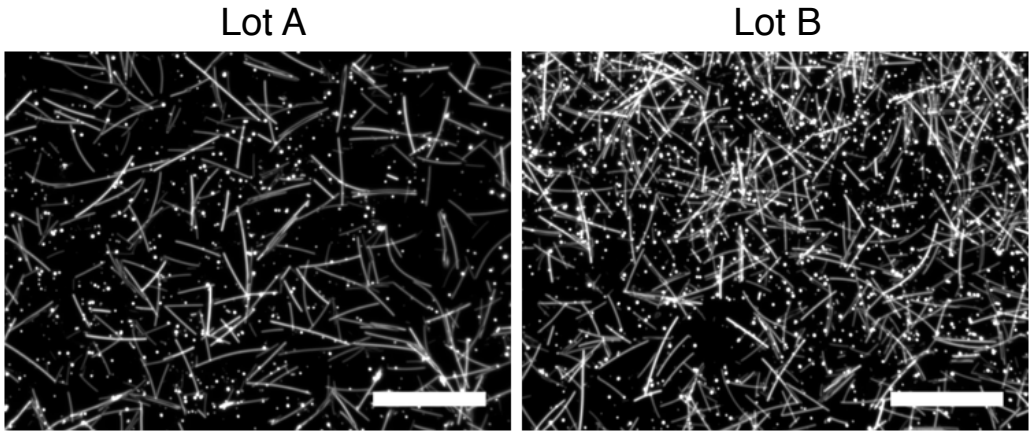


Figure 3.14 – DFOM images of washed AgNWs from (left) lot A (reaction (i)) and (right) lot B (reaction (j)). Scale bar: 20 µm.

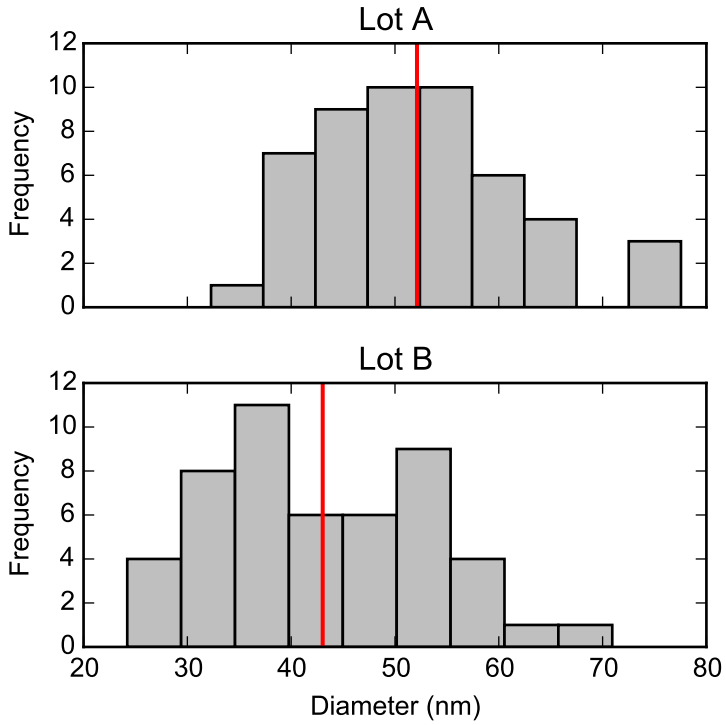


Figure 3.15 – Histograms showing the diameter of AgNWs synthesised in EG from lot A (reaction (i)) and lot B (reaction (j)). The red vertical line marks the mean average. The diameter of 50 AgNWs was measured from the high resolution SEM micrographs shown in Figure 3.13.

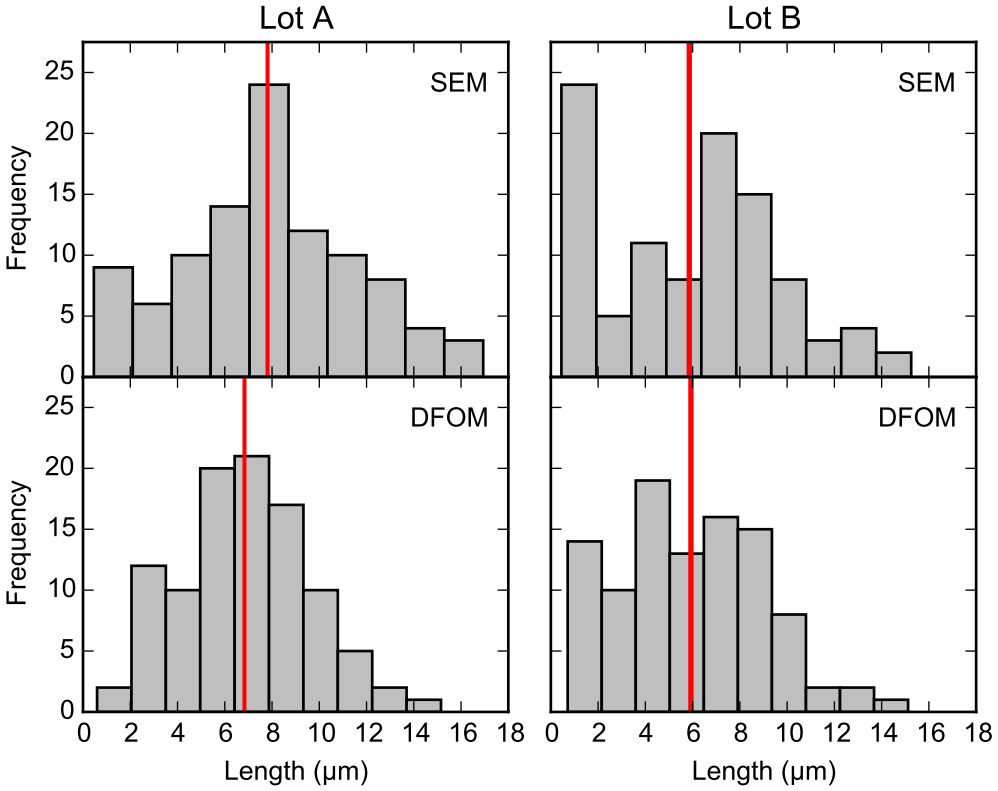


Figure 3.16 – Histograms showing the lengths of washed AgNWs, measured using DFOM and SEM, synthesised in EG from lot A (reaction (i) and lot B (reaction (h)). Each histogram represents 100 AgNWs measurements. The vertical red line marks the mean average.

lot A (7.81 µm) was 33 % longer compared to lot B (5.86 µm). The smaller CV for lot A ($s/\bar{l} = 0.48$) indicated that the length polydispersity was lower than for the AgNWs from lot B ($s/\bar{l} = 0.65$).

As expected, similar trends were observed using DFOM. The median length for lot A (6.64 µm) was 11 % larger than the median length for lot B (5.97 µm). The mean length for lot A (6.83 µm) was 15 % larger than the mean for lot B (5.92 µm). The CV for lot A ($s/\bar{l} = 0.40$) compared to lot B ($s/\bar{l} = 0.52$) indicated that the AgNWs from lot A were more monodisperse.

There was small differences in the average lengths determined using the DFOM and SEM techniques. For lot A, the average lengths determined using each technique are in good agreement to within *ca.* 1 µm. Furthermore, the

		Lot (µm)	
Technique	Statistic	A	B
SEM	Median	7.66	6.51
	Mean	7.81	5.86
	SD	3.72	3.80
DFOM	Median	6.64	5.97
	Mean	6.83	5.92
	SD	2.75	3.08

Table 3.5 – Table showing the median, mean, and SD of the length of AgNWs measured using SEM and DFOM for washed samples from lot A (reaction (i)) and lot B (reaction (j)).

histograms in Figure 3.16 show similarly-shaped length distributions. For lot B, the average lengths from each technique were in even better agreement to within *ca.* 0.5 µm. The histograms for lot B in Figure 3.16, fewer short AgNWs (< 2 µm) were observed using DFOM compared to SEM. The data here are insufficient to establish whether this is due to chance or a characteristic of DFOM. Nonetheless, these results demonstrate the suitability of DFOM for determining the length of AgNW samples, but care must be taken to compare samples using the same measurement technique.

3.3.6 Losses due to washing

In Section 3.3.5, analysis using SEM required crude samples to be washed in order to remove electrically-insulating PVP. Once washed, samples were analysed using DFOM as well as SEM so that the two measurement techniques could be compared. This also enabled us to compare the DFOM measurements of the crude and washed AgNW samples and thus investigate the effect of washing. Figure 3.17 shows histograms of the length of the AgNWs in crude and washed samples from reactions (i) (lot A) and (j) (lot B) measured using DFOM. For lot A, which produced longer AgNWs than lot B, the median decreased from 9.46 to 6.64 µm and the mean decreased from 9.06 to 6.83 µm. For lot B, the median increased slightly from 5.73 to 5.97 µm and the mean decreased from 6.74 to 5.93 µm. This suggests that

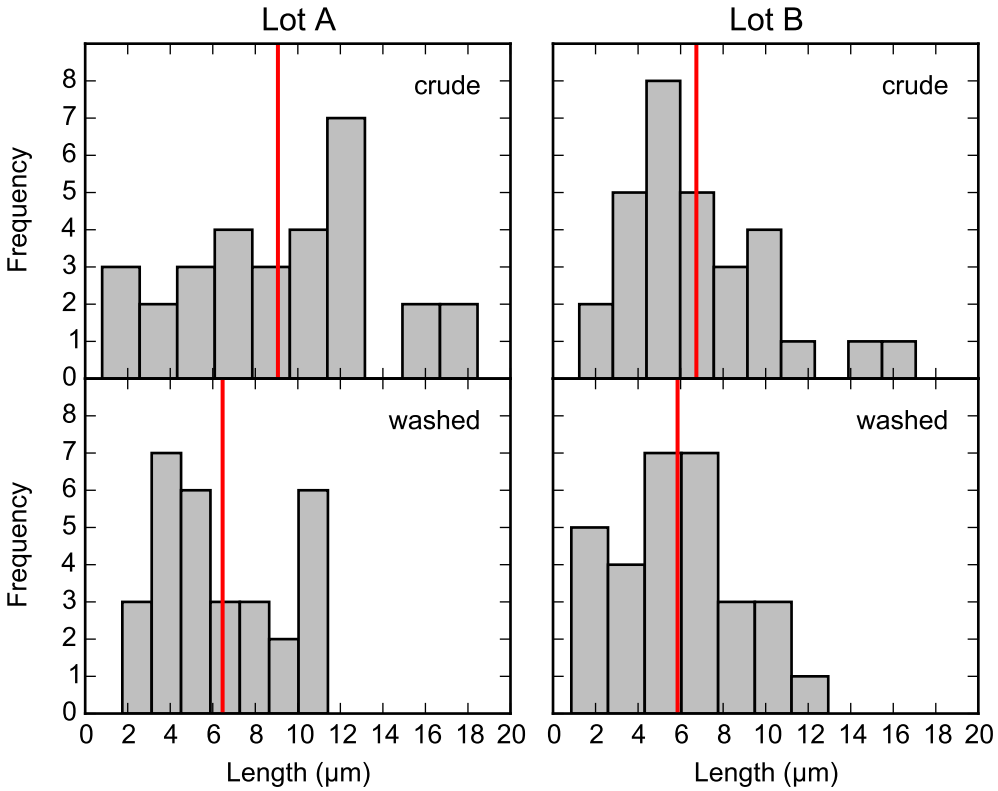


Figure 3.17 – Histograms showing the length of AgNWs measured using DFOM for crude and washed samples synthesised in EG from lot A (reaction (i)) and lot B (reaction (j)). The vertical red line indicates the mean average.

longer AgNWs were lost in the washing process.

3.4 Chemical analysis of ethylene glycol

The large difference in the length of the AgNWs produced using the two different lots of EG suggests the possible presence of a chemical species that inhibits or promotes growth in one of the lots. The manufacturer of the EG provides certificates of analysis for each lot number which show the specification of the EG and the maximum permissible concentration of various chemical elements (see Appendix A.2). Cl, Cu, and Fe ions have been reported to affect the growth of AgNWs (see Section 2.3).

Table 3.6 shows the maximum concentration of these elements from the specification and the corresponding concentrations deliberately added to the reaction from NaCl and $Fe(NO_3)_3$ (see Table 3.2). The table shows that the concentration of Cl^- and Fe^{2+}/Fe^{3+} added to the reaction from solutions of NaCl and $Fe(NO_3)_3$ respectively may be many orders of magnitude smaller than the concentration of Cl and Fe already in the solvent. More specifically, NaCl was added to the reaction mixture to give a final concentration of 4.40 µmol/L. However the specification sheet states that the EG may contain Cl at a concentration of up to 5000 µmol/L—more than 1000 times higher than the final NaCl concentration. Similarly for Fe, the final concentration of $Fe(NO_3)_3$ was 0.20 µmol/L, but the specification was up to 3000 µmol/L—15,000 times higher than desired. Cu, which was not added in this work but is known to affect the AgNW synthesis, may also be present at relatively large concentrations of up to 300 µmol/L.

EG from each lot was analysed using NMR to check for the presence of other organic species. Figure 3.18 shows the ^1H NMR spectra of EG from lots A and B. Three peaks intense peaks were observed. The first peak at 7.3 ppm can be assigned to $CHCl_3$ from the deuterated chloroform used as the solvent. The others were readily assigned to the CH_2 (3.8 ppm, 2 H) and OH ((a) 2.06 ppm; (b) 1.97 ppm; 1 H) protons in EG, in agreement with the literature.[88] Several weak signals were observed at chemical shifts in the range 3.54 to 4.65 ppm (see inset). In particular, there were three

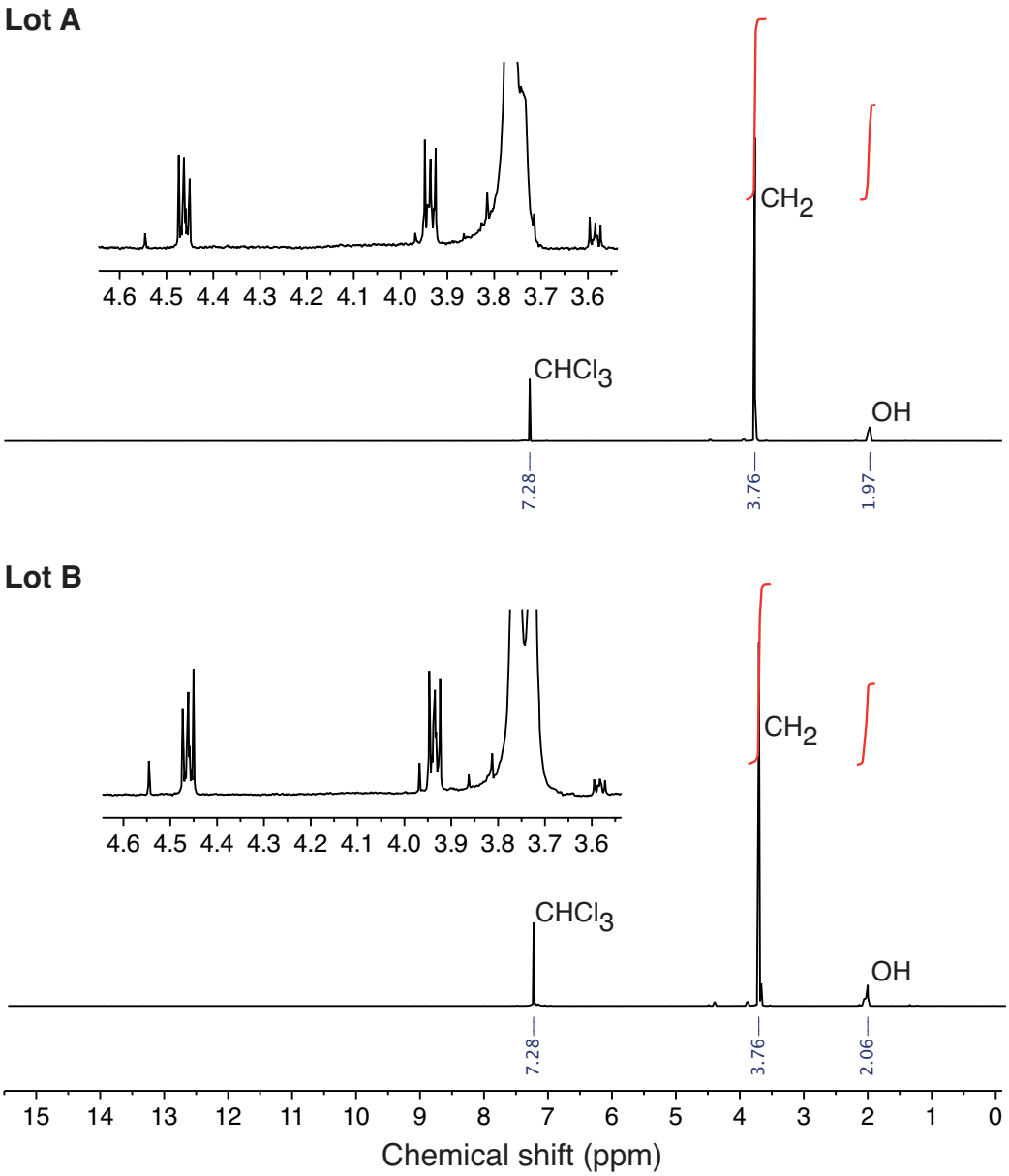


Figure 3.18 – ^{1}H NMR spectra of EG from (top) lot A and (bottom) lot B. EG assignment: δH (400 MHz; $CDCl_3$) (a) 2.1 (1 H, br. s, OH) and 3.8 (2 H, s, CH_2); (b) 2.0 (1 H, br. s, OH) and 3.8 (2 H, s, CH_2). Both spectra show signals consistent with the structure of EG. Inset: enlargement of 3.54 to 4.65 ppm region, showing weaker signals suggesting the presence of higher order glycols.

	Concentration (µmol/L)	
Species	Specification	Reaction
Cl	5000	4.40
Cu	300	—
Fe	3000	0.20

Table 3.6 – Table showing the concentration of Cl, Cu, and Fe in the EG according to the manufacturer certificates of analysis in Appendix A.2. For comparison, the concentration of Cl (from NaCl) and Fe (from $Fe(NO_3)_3$) added to the reaction are shown.

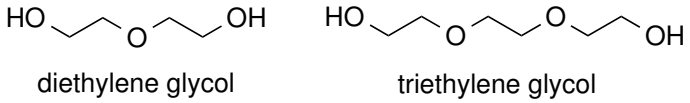


Figure 3.19 – Chemical structure of diethylene glycol and triethylene glycol.

multiplets at 4.46 ppm, 3.94 ppm, and 3.58 ppm, in addition to some weaker singlets. The spectra also show a peak overlapping the CH_2 singlet at around 3.72 ppm, which is more intense in (a). These weaker peaks are most likely attributable to higher order glycols, such as diethylene glycol and triethylene glycol (Figure 3.19), as this region is consistent with $O-CH_2$ protons that are deshielded by adjacent oxygen atoms. The multiplet would arise from coupling to the adjacent CH and OH protons. A two-dimensional NMR correlation spectroscopy (COSY) experiment confirmed that these multiplets were indeed coupled to one another (see Appendix A.3). Aside from the small difference in the chemical shift of the OH peak (which is broad due to proton exchange), the spectra of the two samples were the same and gave no indication that the lots contained differing organic species.

These findings suggests that the difference in the length of the AgNWs produced from lot A and lot B of EG is due to a large difference in the concentration of trace metals.

3.5 Conclusions & further work

The method reported by Bergin and co-workers was chosen as a starting point for the goal of synthesising AgNWs in a flow process. Bergin's synthesis used the hot-injection approach where a solution of $AgNO_3$ is added to a hot reaction mixture. The high temperature results in a fast initial rate of reduction and nanoparticles nucleate and grow almost instantaneously. Simply replicating all of the batch steps in a flow process was considered inefficient. Such a flow reactor would have a long total residence time of at least 2 h and therefore place a limit on how quickly different reaction conditions could be tested. A long residence time would also limit the reactor throughput, unless a large reactor volume was used. This would then require more costly high-pressure pumps. A direct conversion to a flow process would also have the disadvantage of requiring a large number of pumps and junctions, because of the sequential addition of precursors, making the reactor undesirably complex.

The hot-injection procedure was therefore adapted to a heat-up reaction to see whether the number of steps could be reduced and therefore make the flow process simpler and faster. In a heat-up reaction all of the precursors are added to a flask at room temperature, and then it is heated to the reaction temperature. The initial rate of reduction is lower than in the hot-injection reaction, requiring a longer time for the yellow colour of Ag nanoparticles to develop. Analysis using DFOM showed that AgNWs produced using the heat-up method reached a median length of 9.1 µm after 20 min, compared to only 4.1 µm for the hot-injection method. The AgNWs produced in this work, using both methods, compared favourably to the results reported by Bergin *et al.* Using their hot-injection method, the researchers produced AgNWs just 2.5 µm long after 20 min, and 7.4 µm long after 2 h. The heat-up method also produced fewer isotropic nanoparticles as by-products, which is important for large scale production so as to reduce waste. The difference between the heat-up and hot-injection methods is attributable to the temperature of the reaction mixtures over time. The lower initial temperature and therefore lower initial reduction rate of the heat-up method leads to the nucleation of

fewer AgNWs, leaving more Ag available for growth of the seeds into long AgNWs.

Unfortunately the results obtained from this reaction (and the preliminary tests leading up to it) could not be reproduced. Instead of the heat-up reaction producing longer AgNWs and fewer nanoparticle by-products than the hot-injection reaction, both methods repeatedly produced isotropic nanoparticles and a small number of polydisperse and short AgNWs. Either the first results from the heat-up reaction were anomalous or a unknown parameter had changed and caused the reaction to fail. Because the results were a significant improvement over the literature reports and also particularly desirable for a flow process, I decided to try and identify either the cause of the anomaly or the sudden failure.

The entire procedure was carefully examined. The accuracy and precision of pipetting was identified as a possible cause. Using gravimetric analysis it was found that the random error was large relative to the volume of reactants being added to the reactions and could have led to variation in the concentration of the reactants in each reaction. The pipetting procedure was then modified so as to reduce the number of pipetting steps in each reaction and also use as much of the capacity of the pipettes as possible. Gravimetric analysis showed significant improvement in the relative size of the random error.

The adapted procedure was then tested using the heat-up method. The first test showed a similar trend to the results obtained at the start of the chapter. However further repeat reactions showed a sudden degradation in the performance of the reaction (as determined by the AgNW length). Careful examination of the EG used to prepare the precursors found that the lot number of the EG had unknowingly changed between reactions. Additional reactions were then carried out where the lot was changed deliberately. AgNWs grown in EG from lot A were twice as long as those grown in EG from lot B. Importantly, the reaction carried out in lot A produced fewer nanoparticle by-products.

The specification sheets of the EG showed that it could contain concentrations of Cl and Fe several orders of magnitude higher than the concentration

of NaCl and $Fe(NO_3)_3$ added to the reactions. Both lots were examined using NMR, which showed that both lots contained low concentrations of higher glycols like di- and triethylene glycol. Considering the large difference in the product from each lot of EG, it is likely that one of the lots contains a significantly higher or lower concentration of a (or several) metal species that promote or hinder AgNW growth.

Further work is necessary to characterise the chemical differences between the lots of EG. Inductively-coupled plasma mass spectrometry would identify the elements present and quantify their concentration. This information would enable the determination of the concentration of additives required to obtain the results from lot A with other lots of EG. Unfortunately I was unable to gain access to this technique during this work. It is likely that other published reports of metal nanocrystal synthesis using the polyol process were similarly helped or hindered by the unknown presence of contaminants.

Furthermore, DFOM analysis of the washed samples prepared for SEM suggested that the washing and centrifugation process to remove insulating PVP destroyed longer AgNWs. Improvements to the washing procedure are clearly necessary in order to prevent loss of the longest nanowires.

In summary, the batch procedure was successfully adapted—after resolving issues with reproducibility—to a simple heat-up procedure that produced *ca.* 9 µm long AgNWs in a short reaction time of 20 min. The following chapter describes the adaptation of my simplified method to a flow process.

Chapter 4

Flow Synthesis of Silver Nanowires

4.1 Introduction

In Chapter 3 I described a simplification of the batch synthesis of AgNWs reported by Bergin *et al.* from a multi-step hot-injection procedure to a one-pot heat-up reaction. The latter, as discussed in Section 3.1, lends itself to a more straightforward flow process involving fewer components and a shorter residence time (the flow chemistry equivalent of reaction time). In this chapter I describe the development of a flow process for producing AgNWs.

In the previous chapter I also identified a significant difference in the length of the AgNWs produced using two different lots of EG from the same supplier (Sigma-Aldrich). The EG from lot BCBN5970V (lot A) produced longer AgNWs and for this reason, unless stated otherwise, it was used throughout this chapter.

4.2 Preliminary tests

Figure 4.1 shows a schematic of the flow reactor used for my first attempt at producing AgNWs in flow. Two syringe pumps fitted with gas-tight glass syringes were connected to the inlets of a polyether ether ketone (PEEK)

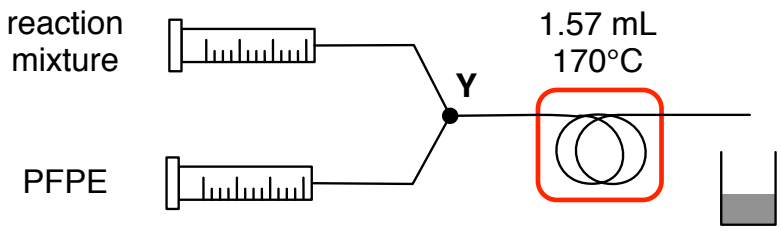


Figure 4.1 – Schematic of the reactor used for the first attempt at synthesising AgNW in flow. A syringe containing the reaction mixture of NaCl, PVP, $Fe(NO_3)_3$, and $AgNO_3$ and a syringe of PFPE carrier fluid are injected into a Y-mixer (**Y**) at flow rates of 39.25 µL/min each. The segmented flow generated at **Y** enters a 2 m long coil of 1 mm ID PTFE tubing (1.57 mL, 20 min residence time) immersed in an oil bath at 170 °C. The flow is collected at the outlet, where the product and carrier fluid separate by gravity.

Y-mixer. The outlet of the Y-mixer was connected to a 2 m long coil of 1 mm ID PTFE tubing (1.57 mL) immersed in a well-stirred oil bath at 170 °C. A vial was placed at the end of the tubing for waste or sample collection. Glass syringes were selected over plastic syringes because of their ability to withstand cleaning using nitric acid and also their higher stiffness which results in a more stable flow. PTFE tubing was selected for its chemical inertness, its stability at elevated temperatures, low cost, and optical transparency (which allows visual inspection of the flow).

The same solution of NaCl, PVP, $Fe(NO_3)_3$, and $AgNO_3$ used in the batch heat-up synthesis (developed and tested in Sections 3.3.2 and 3.3.3, respectively) was prepared and loaded into one of the syringes. The syringe was wrapped in aluminium foil to block out ambient light (as $AgNO_3$ reacts with NaCl to form AgCl, which is reduced to Ag upon exposure to light). PFPE was loaded into the other syringe. It was chosen as the carrier fluid for its chemical inertness and immiscibility with most solvents over a wide range of temperatures. It also preferentially wets PTFE and hence prevents the reaction mixture from contacting the channel walls, significantly reducing the likelihood of fouling compared to continuous flow. The reaction mixture and carrier fluid were injected into the Y-mixer, thus generating a segmented flow into the coil of tubing in the oil bath. Figure 4.2 shows a photograph of a PFPE–EG segmented flow representative of the flow produced from the

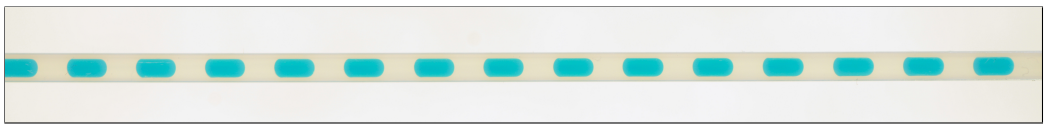


Figure 4.2 – Photograph of a PFPE-EG segmented flow from the outlet of the Y-mixer. The EG was dyed with methylene blue to render it visible.

Y-mixer.

In the batch experiments in Chapter 3 the reaction mixture was colourless. However, approximately 30 min after the solution had been prepared and loaded into the syringe, the solution and the slugs exiting the Y-mixer had turned pale yellow, indicating that some of the $AgNO_3$ had been reduced and formed silver nanoparticles (which have a characteristic yellow colour due to surface plasmon resonance). Any chemical reaction of the precursor solution in the syringe was considered unacceptable because it would lead to variation in the product over time. Therefore a different reactor configuration was required.

4.3 Dual-precursor flow reactor

Xiong *et al.* reported the reduction of $AgNO_3$ by PVP at 60 °C.[83] From this it seemed reasonable that nucleation of $AgNO_3$ in the syringe might be prevented by separating $AgNO_3$ from the other reactants. Figure 4.3 shows a schematic of the dual-precursor flow reactor used to test this hypothesis, where the single syringe containing all the precursors was replaced with two separate syringes, one containing PVP and the other containing all other reagents. To accommodate the extra syringe, the Y-mixer was replaced the three-in-one-out junction shown in Figure 4.4 (see Section 5.3.2 for specification). One syringe contained $AgNO_3$ solution (precursor A) and the other syringe contained a solution of PVP, $Fe(NO_3)_3$, and NaCl (precursor B). With the new configuration, no colour change of the $AgNO_3$ solution was observed even after 24 h.

During preliminary tests approximately a quarter of the slugs coalesced to form larger slugs (up to 20 mm long) as they flowed through the heated

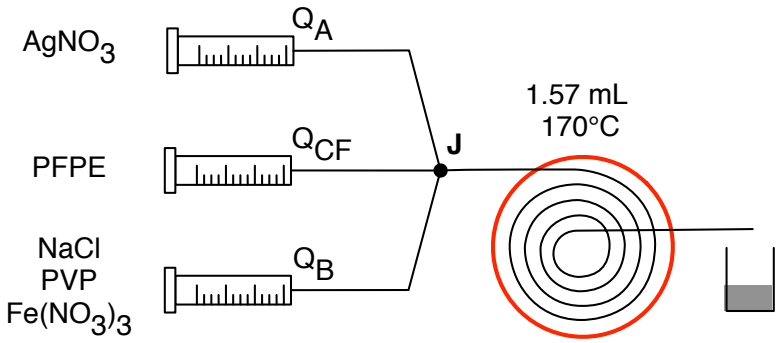


Figure 4.3 – Schematic of the dual-precursor flow reactor for producing AgNWs in flow. Precursor A (EG solution of $AgNO_3$), PFPE carrier fluid, and precursor B (EG solution of NaCl, PVP, and $Fe(NO_3)_3$) are pumped at volumetric flow rates Q_A, Q_{CF}, and Q_B respectively into a three-in-one-out junction **J** ($Q_A/Q_B = 0.905$ and $Q_{CF}/(Q_A + Q_B) = 1$). The segmented flow generated at **J** exits the outlet and passes into a 2 m length of 1 mm ID PTFE tubing (1.57 mL) immersed in an oil bath at 170 °C. The outlet stream is collected into a vial.

section. Whilst no channel fouling was observed, this coalescence was a concern because it resulted in the reactant-product mixture contacting the channel walls for a longer period of time before being "washed" by the PFPE, thus potentially increasing the likelihood of fouling. Additionally, the slugs were no longer identical, potentially leading to higher polydispersity. Inspired by the work of Bannock and co-workers,[89] the reactor tubing was threaded through a metal frame in a spiral configuration, see Figure 4.5. The entire frame was then immersed an oil bath. By fixing the tubing in a horizontal plane, vertical movement of the slugs was minimised and preliminary tests using neat EG indicated that this eliminated coalescence.

Table 4.1 shows the flow rates used to vary the residence time t_R. The volumetric flow rate ratio of precursor A to precursor B was fixed at $Q_A/Q_B = 0.905$ so that the concentration of the reactants in the droplets was the same as for the batch reaction. PFPE carrier fluid was injected at a flow rate equal to the total flow rate of the precursors ($Q_{CF} = Q_A + Q_B$) in order to produce a balanced segmented flow. The total flow rate ($Q_{total} = Q_{CF} + Q_A + Q_B$) was varied to give residences times of 13 min, 16 min, and

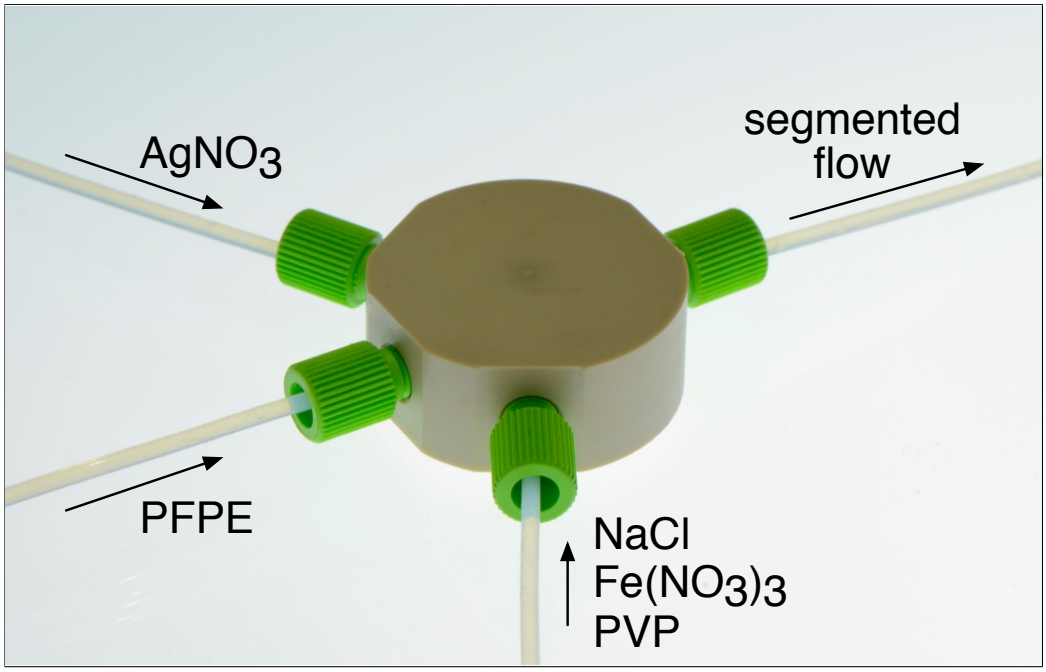


Figure 4.4 – Photograph of a three-in-one-out junction with tubing connected to the three inlets for the $AgNO_3$ solution, carrier fluid, and a solution of NaCl, $Fe(NO_3)_3$, and PVP. A segmented flow exits through the outlet. The junction was machined from PEEK. See Section 5.3.2 for full specification.

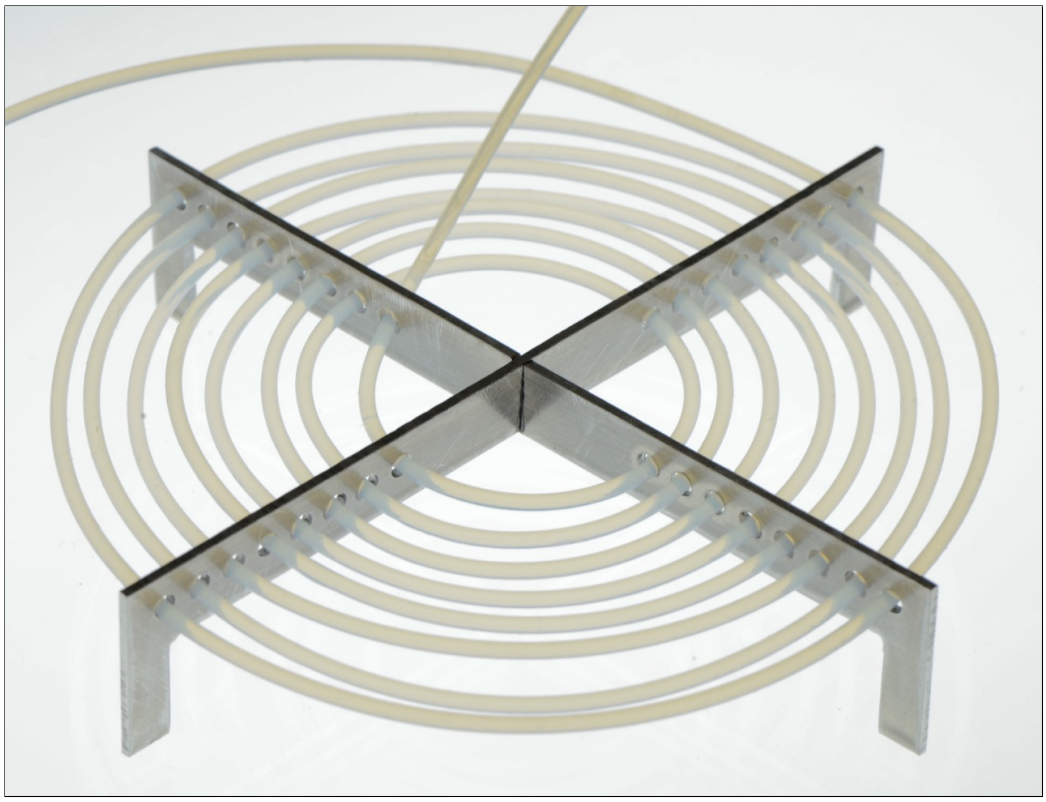


Figure 4.5 – Photograph of the metal frame used to mount the reactor tubing in a horizontal plane. The tubing enters at the centre and spirals outwards. For scale, the outer diameter of the tubing is 2 mm.

	Flow rate (µL/min)			
t_R (min)	Q_{tot}	Q_{CF}	Q_{A}	Q_{B}
13	120.85	60.42	28.71	31.72
16	98.20	49.09	23.33	25.78
20	78.55	39.27	18.66	20.62

Table 4.1 – Flow rates used to vary the residence time t_R for the dual-precursor flow reactor shown in Figure 4.3. $t_R = V/Q_{\text{tot}}$, where V is the reactor volume (1.57 mL) and Q_{tot} is the total flow rate. The ratio of the flow rates of precursor A to precursor B was constant ($Q_{\text{A}}/Q_{\text{B}} = 0.905$). Equal flow rates of carrier fluid and reagent were used ($Q_{\text{CF}}/(Q_{\text{CF}} + Q_{\text{B}}) = 1$) in order to generate a segmented flow.

20 min (equivalent to the times at which samples were taken from the batch reactions in Chapter 3). After changing the flow rates, the reactor was left for $1.5 \times t_R$ in order to establish a uniform segmented flow. During this stabilisation time the product was collected into a waste beaker. For sample collection, the beaker was replaced with a vial containing 1 mL water, and product was collected for approximately 1 min per sample. The vial was gently swirled to disperse the product into the water, giving a turbid grey solution. (The addition of water to the viscous product made it easier to recover from the PFPE using a Pasteur pipette.)

Figure 4.6 shows a photograph of the reactor in operation. The three residence times were carried out using a single preparation of precursors and repeated three times in total using new precursors each time (precursor A was always prepared fresh, while precursor B was prepared from stock solutions of the individual components). In all experiments, the colourless slugs of reaction mixture turned yellow within 2 min of them entering the oil bath. After 8 min, the slugs turned grey, and by 12 min a small droplet of gas had formed next to each slug. No further colour changes were observed with longer residence times, but the volume of the gas slug steadily increased by up to 50 % when the residence time was 20 min. The gas slugs often had the unwanted effect of causing the immediately adjacent slugs to coalesce.

Each crude sample was analysed using DFOM as described in Section 5.4.3.

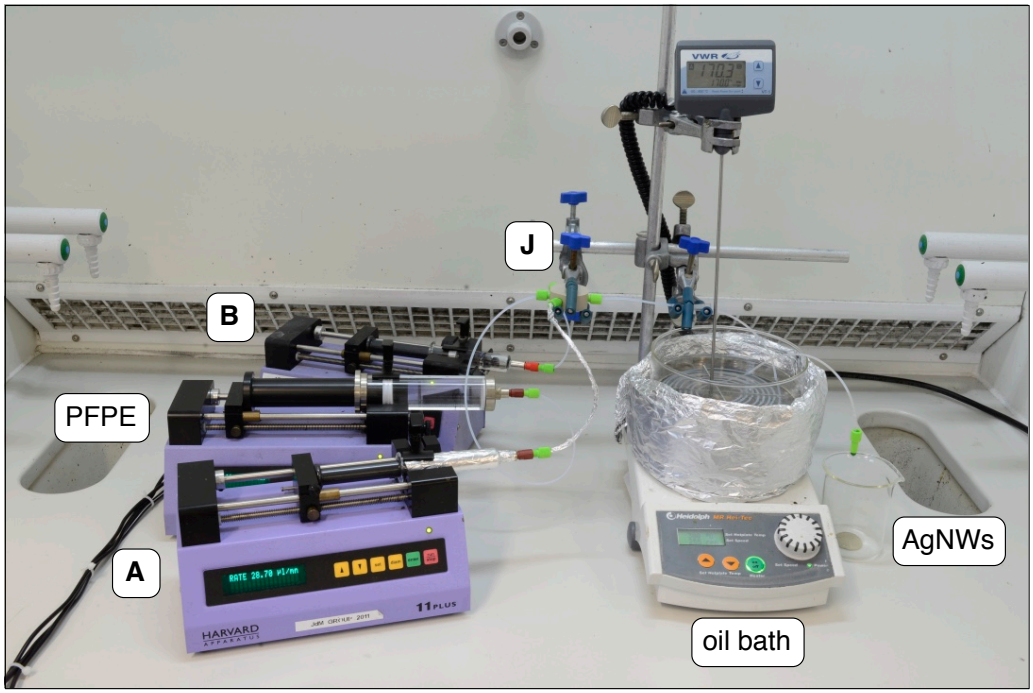


Figure 4.6 – Photograph of the typical dual-precursor reactor configuration. Left: pumps for precursor **A** (with syringe wrapped in aluminium foil), precursor **B**, and PFPE carrier fluid. Centre (mounted in clamp): three-in-one-out junction **J** (see Figure 4.4 for close-up photograph). Right: oil bath containing tubing mounted in metal frame and beaker at outlet collecting product.

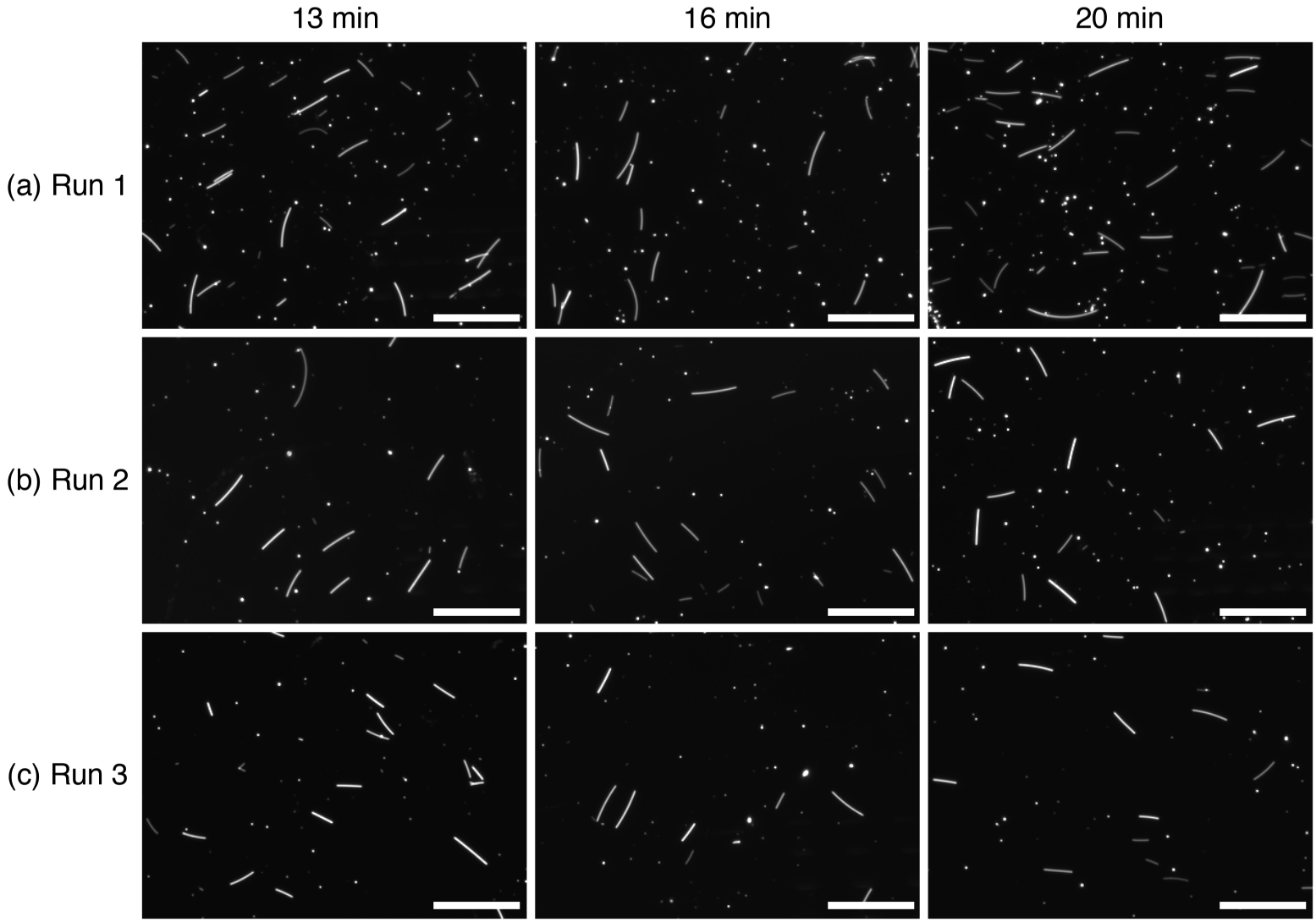


Figure 4.7 – DFOM images of samples produced in flow. (a–c): runs 1–3. Left to right: 13 min, 16 min, and 20 min residence times. Scale bars: 20 µm.

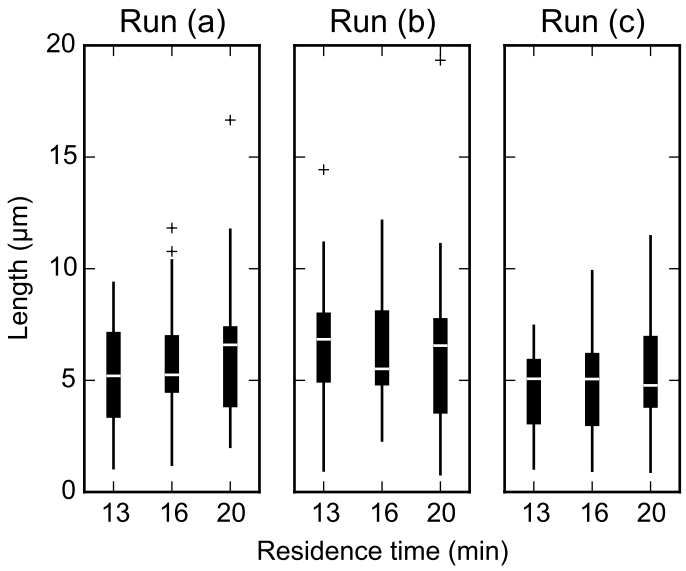


Figure 4.8 – Box and whisker plots showing the length of 30 AgNWs for residence times of 13 min, 16 min, and 20 min. The experiment was repeated three times (a–c).

Figure 4.7 shows the DFOM images that were recorded. The images show that AgNWs and silver nanoparticles were produced for all three residence times and repeat runs. The length of the AgNWs are plotted in the box and whisker plots in Figure 4.8. For run (a) the median length was 5.2 µm for the shortest residence time of 13 min. A 16 min residence time produced AgNWs with a similar median length of 5.3 µm. The longest residence time of 20 min produced the longest AgNWs with a median length of 6.6 µm. For run (b), slightly longer AgNWs were obtained but, as with run (a), there was little variation in the median length. The median was 6.8 µm after 13 min, decreasing to 5.5 µm after 16 min, and increased to 6.6 µm after 20 min. For run (c), the median was 5.1 µm, 5.1 µm, and 4.8 µm for residence times of 13 min, 16 min, and 20 min, respectively, indicating little growth after 13 min.

The boxes (representing the second and third quartiles) in Figure 4.8 show that most of the AgNWs were of similar length regardless of residence time and run. Taken together, the weak dependence of the median length on the residence time suggested that AgNW growth had already stopped

after 13 min and that the all of the $AgNO_3$ had been reduced to Ag^0. After approximately 12 min gas evolution was observed. This was most probably NO, a by-product of the dissolution of Ag by HNO_3 (see Scheme 3.2 on page 73). Therefore even longer residence times would be expected to result in a decrease in yield and AgNW length.

The overall median length at $t_R = 20$ min across runs (a–c) was 6.0 µm. In comparison, the batch experiments in Section 3.2 had a median of 4.1 µm for the hot-injection reaction and 9.1 µm for the heat-up reaction (both after 20 min). Therefore the AgNWs produced in flow were 46 % longer than the hot-injection product but 34 % shorter than the heat-up product. The overall standard deviation at $t_R = 20$ min across runs (a–c) was 3.1 µm, compared to 2.9 µm and 3.4 µm for the hot-injection and heat-up reactions, respectively. Therefore the AgNWs produced in flow were more polydisperse than those produced using the hot-injection route, but less polydisperse than the AgNWs produced using the heat-up route.

4.4 Stability testing

The AgNWs produced using the dual-precursor flow reactor in Section 4.3 were approximately one third shorter than the AgNWs synthesised using the batch heat-up method. Furthermore, the DFOM revealed the presence of nanoparticle by-products, which require the use of time-consuming and wasteful purification procedures to remove them. It was hoped that adjustments to the reaction conditions—like the reaction temperature or concentration of a precursor—might produce longer AgNWs with better shape-selectivity. However before testing whether this was indeed the case it was necessary to first demonstrate that the reactor was capable of consistently producing the same product under fixed reaction conditions. If the product varied during reactor operation it would be impossible to establish whether any observed changes were due to changes in the parameter being varied or reactor instability. The reactor channels must also be resistant to fouling, otherwise the channels will narrow (which reduces the reactor volume and decreases the residence time) and eventually block completely.

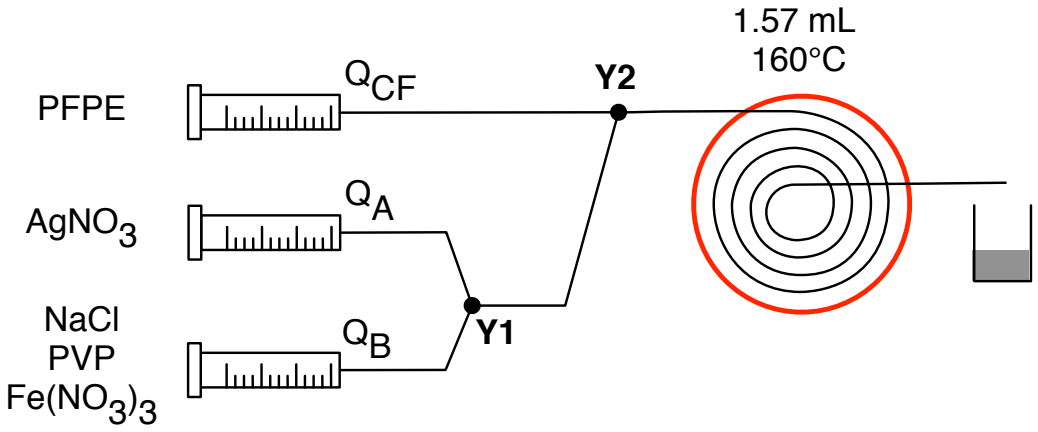


Figure 4.9 – Schematic of the flow reactor used to assess the consistency of the product during operation. An EG solution of $AgNO_3$ and an EG solution of NaCl, PVP, and $Fe(NO_3)_3$ were pumped into Y-mixer **Y1** at $Q_A = 39.37\,\mu L/min$ and $Q_B = 12.99\,\mu L/min$, respectively. The outlet of **Y1** was connected to one of the inlets of Y-mixer **Y2** and PFPE was pumped at $Q_{CF} = 52.36\,\mu L/min$ into the other. The segmented flow produced at the outlet of **Y2** was connected to a 2 m length of 1 mm ID PTFE tubing (1.57 mL) threaded through a metal frame and immersed in an oil bath at 160 °C. The outlet stream was collected into a vial.

Figure 4.9 shows a schematic of the flow reactor used to assess the stability of the segmented flow process. The results in Section 4.3 suggested that the reaction had gone to completion in less than 13 min, so the oil bath temperature was reduced from 170 °C to 160 °C to reduce the rate of nucleation and increase the amount of $AgNO_3$ available for AgNW growth. To compensate for the reduction in temperature, the residence time was increased slightly by 2 min to 15 min ($Q_{CF} = 52.36\,\mu L/min$, $Q_A = 39.37\,\mu L/min$, and $Q_B = 12.99\,\mu L/min$). In order to test the resilience of the reactor to fouling, the concentration of $AgNO_3$ in the slugs was increased 2.5 times from 25.6 mM to 64.3 mM.

In the experiments in Section 4.3, a single set of precursors was used to test 13 min, 16 min, and 20 min residence times. Including time for sample collection, switching between flow rates, and waiting for the reactor to reach steady state, the precursors were at most 90 min old by the time the reactions had completed. For the stabilisation tests larger volumes of precursor were

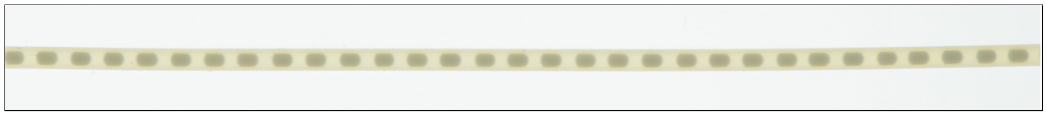


Figure 4.10 – Photograph of the segmented flow after it exited the oil bath, showing grey slugs of AgNWs dispersed in colourless PFPE.

loaded into the syringes so that the reactor could run for continuously for 8 h. After the reactor had reached steady state and produced a uniform flow, the product was collected into a vial. The vial was replaced with a new vial every 1 h.

Figure 4.10 shows a photograph of the segmented flow after it exited the oil bath, with the slugs undergoing the same colour changes as before. A small number of slugs (fewer than one in a hundred) coalesced due to the formation of a gas bubble in the last *ca.* 1 min of the heated section. As discussed in Section 3.2.1, NO gas is a by-product of the oxidation of Ag by HNO_3. This observation suggested that the increase in residence time from 13 to 15 min, even with the 10 °C reduction in temperature, was unnecessary and may have even resulted in slight decrease in AgNW length.

Results of the DFOM analysis are shown in the box and whisker plots in Figure 4.11 (a). As indicated by the outliers, every fraction contained a small number of very long AgNWs (up to 20.7 µm). The median length of each fraction varied between 5.5 and 7.2 µm and the median of all measurements was 6.2 µm. This was slightly longer than the overall median length of 6.0 µm with the dual precursor reactor in Section 4.3, which used $t_R = 20$ min, $T = 170$ °C, and a lower $AgNO_3$ concentration.

Figure 4.11 (b) shows a scatter plot of each AgNW measurement against fraction number. The red line shows the linear function $l = \beta_0 + \beta_1 n$, where l is AgNW length and β_0 and β_1 are coefficients. n is fraction number ($n = 1, 2, ..., 8$) with fraction n corresponding to the product collected over the nth hour of operation. Using least squares regression, the 95 % confidence interval of the coefficients $\beta_0 = 6.6 \pm 0.9$ µm (equal to the mean AgNW length across all fractions) and $\beta_1 = 0.0 \pm 0.2$ µm. Since $\beta_1 \approx 0$, there was virtually no change in the length of the AgNWs produced. Furthermore, no significant

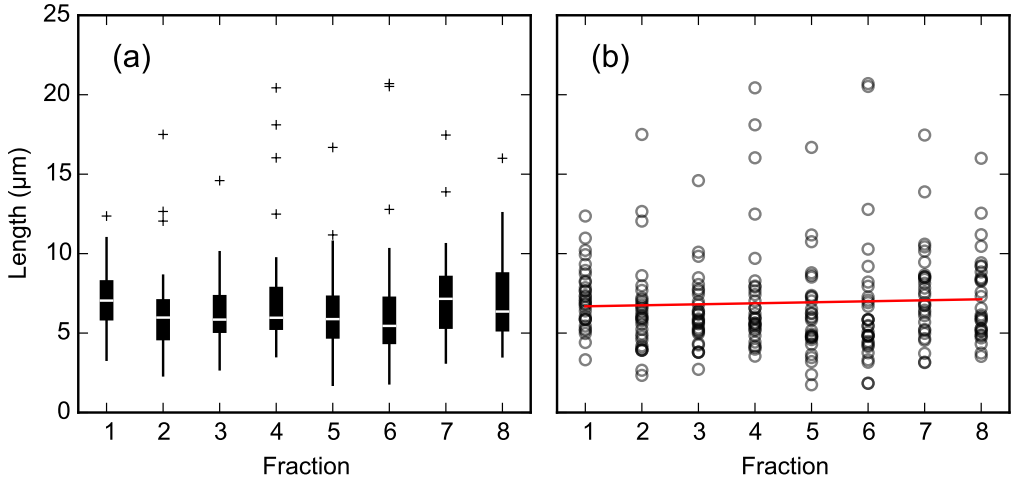


Figure 4.11 – (a) Box and whisker and (b) scatter plots showing the length of 30 AgNWs measured from 8 fractions collected hourly over 8 h continuous operation ($T = 160\,°C$ and $t_R = 15\,min$). Fraction n corresponds to the product collected over the nth hour of operation. The red line shows the linear line of best fit.

relationship was found between the AgNW length and fraction number over the 8 h production period.[a]

Figure 4.12 shows DFOM images of the first and last fraction. They show that both fractions produced a similar quantity of isotropic nanoparticles in addition to AgNWs, much like the images of AgNWs produced from the dual-precursor reactor in Section 4.3.

In summary, these results demonstrate the suitability of a segmented flow reactor for the continuous production of AgNWs. The flow reactor was shown to produce consistent product over an 8 h period of operation with no evidence of reactor fouling, even with a higher $AgNO_3$ concentration. The good stability of the product suggested that the reactor could be used to investigate the effect of changing individual reaction parameters on the product shape and size, as described in the following sections.

[a]The null hypothesis ($H_0 : \beta_1 = 0$) could not be rejected ($p = 0.48$) in favour of the alternative hypothesis ($H_a : \beta_1 \neq 0$).[90]

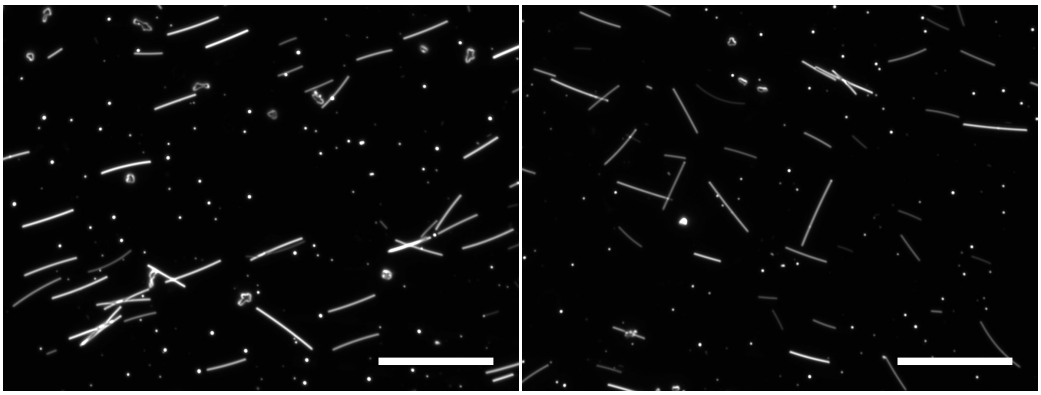


Figure 4.12 – DFOM images of product from the first (left) and last (right) fractions produced during the stability testing of the reactor. Scale bar: 20 µm.

4.5 Effect of varying reaction temperature and residence time

Having established that the reactor was stable over an 8 h operating period, temperature and residence time were chosen as the first parameters to investigate. The rate of reduction of $AgNO_3$ by EG has previously been shown to increase with temperature. For example, Bergin *et al.* found that it took 3 h to reach 80 % conversion of Ag^+ to Ag^0 at 140 °C, but only around 30 min at 160 °C.[74] The change in reduction rate will affect the rate of nucleation and growth, and should therefore affect the size and shape of the product.

Samples were produced using residence times of 13 min, 16 min, 20 min, and 25 min at temperatures between 150 °C and 170 °C (in 5 °C intervals). Table 4.2 shows the flow rates used for each residence time. Residence times were tested in a randomised order. Fresh precursors were prepared for each reaction temperature and, as in the previous experiments, the reactor was allowed to stabilise for 1.5 times the residence time after setting each flow rate to reach steady-state. Product was collected for each temperature and residence time combination and then analysed using DFOM as before.

Figure 4.13 shows graphs of AgNW length versus residence time for each temperature tested. The hollow grey circles show the length of individual

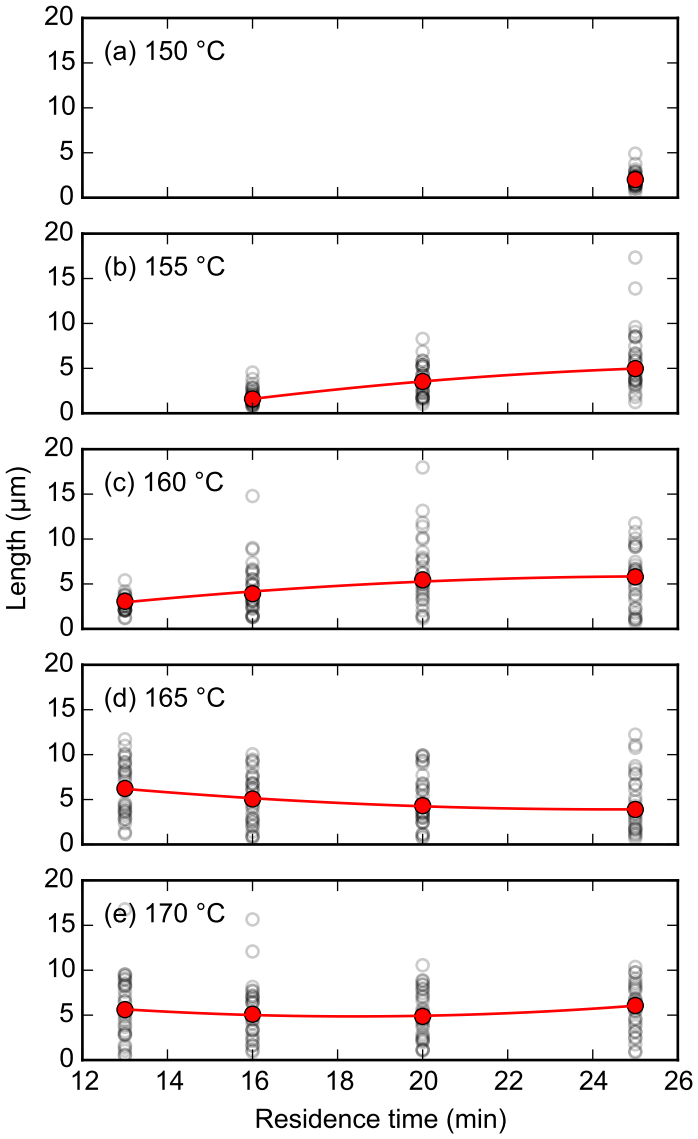


Figure 4.13 – Graphs showing AgNW length against residence time for temperatures between 150 °C and 170 °C (a–e). Each grey circle represents a single AgNW measurement. Red dots mark the median length for each residence time. The red line is a guide to the eye. No AgNWs were produced for $t_R < 25$ min at $T = 150$ °C and $t_R = 13$ min at $T = 155$ °C.

	Flow rate (µL/min)			
t_R (min)	Q_{total}	Q_{CF}	Q_{A}	Q_{B}
13	120.85	60.42	28.71	31.72
16	98.20	49.09	23.33	25.78
20	78.55	39.27	18.66	20.62
25	62.84	31.42	14.93	16.50

Table 4.2 – Table showing the residence time t_R and flow rates for experiments to investigate the effect of temperature and residence time on the synthesis of AgNWs. Q_{total} is the total flow rate, Q_{CF} is the flow rate of carrier fluid, and Q_{A} and Q_{B} are the flow rates of precursors A and B. ($t_R = V/Q_{total}$, where the reactor volume $V = 1.57\,\text{mL}$; $Q_A/Q_B = 0.905$; $Q_{\text{CF}}/(Q_{\text{CF}} + Q_{\text{B}}) = 1$.)

AgNWs, whilst the red markers show the median length. Figure 4.13 (a) shows the results for the lowest temperature, $T = 150\,°\text{C}$. AgNWs were only produced for $t_R = 25\,\text{min}$, with shorter residence times producing isotropic particles. The AgNWs obtained using $t_R = 25\,\text{min}$ were relatively short with a median length of 2.0 µm.

A 5 °C increase in temperature to 155 °C resulted in the production of AgNWs at a shorter residence time of 16 min. Figure 4.13 (b) shows that the median length increased steadily from 1.60 µm at $t_R = 16\,\text{min}$, to 3.5 µm at $t_R = 20\,\text{min}$, to 5.0 µm at $t_R = 25\,\text{min}$.

Figure 4.13 (c) shows a similar trend for $T = 160\,°\text{C}$. AgNWs were produced at the shortest residence time tested, $t_R = 13\,\text{min}$, and these had a median length of 3.1 µm. The AgNWs grew in length as the residence time increased. For the last two samples taken at $t_R = 20\,\text{min}$ and 25 min, the median increased only slightly from 5.5 to 5.8 µm, suggesting that the reaction had nearly reached completion. A slightly different trend was observed for $T = 165\,°\text{C}$, shown in Figure 4.13 (d). The AgNWs with the largest median length were produced at the shortest residence time, and longer residence times produced shorter AgNWs. At $t_R = 13\,\text{min}$, the median length was 6.2 µm, but at $t_R = 25\,\text{min}$ it was 3.9 µm. However, a number of longer AgNWs up to *ca.* 12.5 µm long were present for all residence times, suggesting

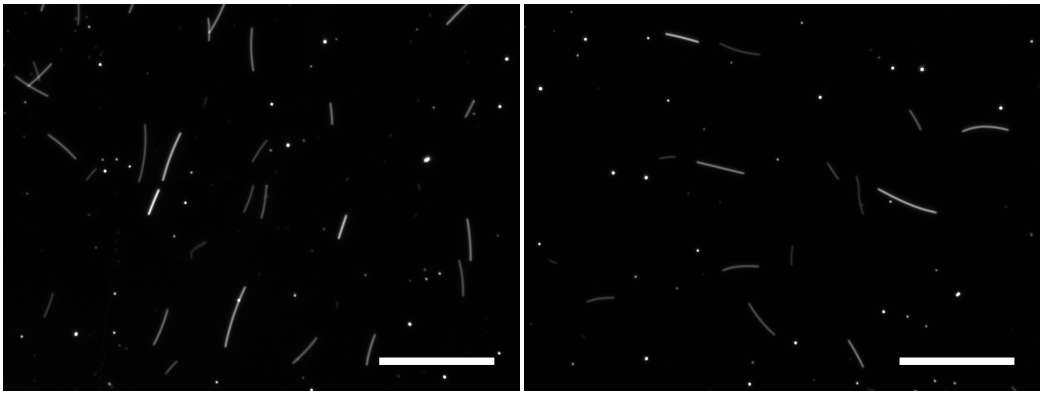


Figure 4.14 – DFOM images of AgNWs produced at $T = 165\,°C$ and $t_R = 13\,\text{min}$ (left) and $T = 170\,°C$ and $t_R = 25\,\text{min}$ (right). The median lengths were 6.2 µm and 6.1 µm, respectively. Scale bar: 20 µm.

that nucleation and growth were occurring simultaneously. Figure 4.13 (e) shows that there was relatively little change in the length of the AgNWs produced for the highest temperature tested, $T = 170\,°C$. The longest AgNWs were produced at $t_R = 25\,\text{min}$, with a median length of 6.1 µm.

Overall, the longest AgNWs with a median length of 6.2 µm were obtained using $t_R = 13\,\text{min}$ and $T = 165\,°C$. In comparison to the batch results in Chapter 3, AgNWs produced using the hot-injection method were approximately a third shorter (4.1 µm), but the heat-up route produced AgNWs that were approximately 50 % longer (9.1 µm). There was also a slight difference in the length of the AgNWs produced at $T = 160\,°C$ in this experiment and those in the stability tests, which were at the same temperature. The stability tests produced AgNWs with an overall median length of 6.2 µm at $t_R = 15\,\text{min}$, whilst the largest median length at the same temperature in this experiment (obtained using a separate batch of precursor) was only 5.8 µm (0.4 µm shorter) at $t_R = 25\,\text{min}$. This suggests that the reaction may be sensitive to precursor preparation. If large quantities of consistent product were required, however, a large batch of precursor could be prepared and continuously pumped into the reactor until the desired quantity of product was obtained.

Unfortunately, changes in the temperature and residence time had no discernible effect on the number of isotropic nanoparticle by-products. For

example, Figure 4.14 shows DFOM images of two samples of similarly-sized AgNWs produced using different temperature-residence time combinations. The left image shows AgNWs produced at $T = 165\,°\text{C}$ and $t_R = 13\,\text{min}$. The right image shows AgNWs produced at $T = 170\,°\text{C}$ and $t_R = 25\,\text{min}$. Both images show a similar number of nanoparticle by-products relative to the number of AgNWs.

4.6 Varying concentration of ionic additives

4.6.1 Sodium chloride

As described in Section 2.3, the presence of ionic species like Cl^- promotes growth of AgNWs in the polyol synthesis. The concentration of NaCl used in the flow reactions reported above may not have been optimal for obtaining long AgNWs, so its effect on AgNW length was investigated.

The concentration of NaCl could not be independently varied using the reactors used in the previous sections as any change to the flow rate ratio of precursor A to precursor B would also change the ratio of $AgNO_3$ to PVP and $Fe(NO_3)_3$. In order to change the concentration of NaCl independently of the other reagents, the reactor was modified to incorporate a third precursor syringe, the schematic of which is shown in Figure 4.15. Precursor B, which previously contained a solution of $Fe(NO_3)_3$, NaCl, and PVP, was replaced with a pair of syringes connected together with a Y-mixer. Both syringes contained the concentration of PVP (74.6 mM) and $Fe(NO_3)_3$ (19.1 µM) used in the previous flow experiments, but they contained differing concentrations of NaCl. This enabled control over the concentration of NaCl in the segmented flow by varying the flow rate ratio of these two syringes. Generally, we can denote the concentration of species x and its concentration in syringe A as $[x]_A$ and the concentration in syringe B as $[x]_B$. If syringes A and B are injected into a Y-mixer (or other junction) at volumetric flow rates Q_A and Q_B, respectively, then the concentration after the Y-mixer $[x]_Y$ is

$$[x]_Y = P[x]_A + (1 - P)[x]_B \tag{4.1}$$

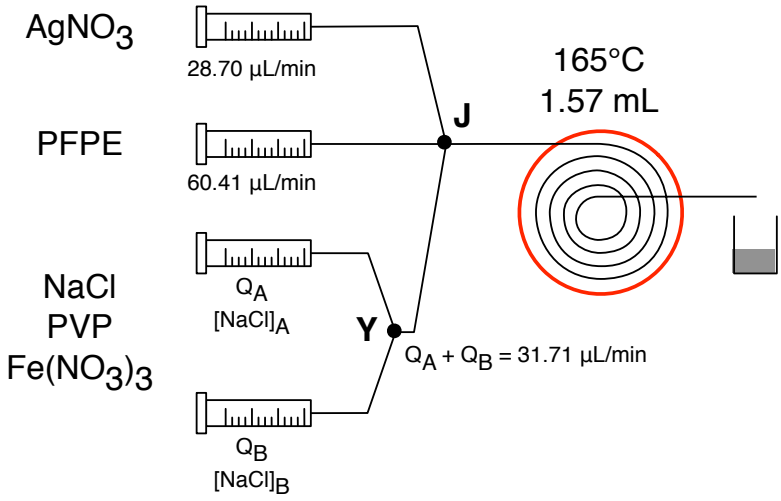


Figure 4.15 – Schematic of the reactor used to vary the concentration of NaCl in the droplets. Two solutions containing different concentrations of NaCl, $[\mathrm{NaCl}]_A$ and $[\mathrm{NaCl}]_B$, were pumped into a Y-mixer **Y**. By varying the relative ratio of the two syringes, the outlet stream of the Y-mixer contains a concentration between $[\mathrm{NaCl}]_A$ and $[\mathrm{NaCl}]_B$. The concentrations of $Fe(NO_3)_3$ and PVP were the same in both precursors. The outlet of the Y-mixer, PFPE carrier fluid, and $AgNO_3$ precursor are connected to the inlets of a three-in-one-out junction **J**. The outlet of the droplet generator is connected to 2 m of 1 mm ID tubing immersed in an oil bath ($T = 165\,°\mathrm{C}$ and $t_R = 13\,\mathrm{min}$).

where $P = Q_A/(Q_A + Q_B)$.

Table 4.3 shows the five sets of flow rates tested for two different pairs of syringes. For pair (i), syringe A contained the standard concentration of NaCl (0.420 mM) and syringe B contained no NaCl. Therefore $[\mathrm{NaCl}]_Y$ could be varied between 0 ($P = 0$) and 0.420 mM ($P = 1$). The outlet of the Y-mixer ($Q_A + Q_B = 31.71\,\mu\mathrm{L/min}$) then flowed into the three-in-one-out junction where it was combined with the $AgNO_3$ flow ($Q_{\mathrm{Ag}} = 28.70\,\mu\mathrm{L/min}$). At this junction $P = 0.525$, and since the $AgNO_3$ precursor did not contain any NaCl, it follows from Equation 4.1 that the NaCl concentration decreased to $0.525 \times [\mathrm{NaCl}]_Y$, resulting in a NaCl concentration range between 0 and 0.220 mM in the segmented flow.

For pair (ii), syringe A contained a higher concentration of NaCl (2.11 mM) and syringe B contained the standard concentration (0.420 mM). Therefore

	Flow rate (µL/min)		[NaCl] (mM)	
P	Q_A	Q_B	After **Y**	After **J**
(i) $[\text{NaCl}]_A = 0.420\,\text{mM}$ and $[\text{NaCl}]_B = 0$				
1.00	31.71	0	0.420	0.220
0.75	23.78	7.93	0.315	0.165
0.50	15.86	15.86	0.210	0.110
0.25	7.93	23.78	0.105	0.055
0	0	31.71	0	0
(ii) $[\text{NaCl}]_A = 2.11\,\text{mM}$ and $[\text{NaCl}]_B = 0.420\,\text{mM}$				
1.00	31.71	0	2.105	1.105
0.75	23.78	7.93	1.684	0.884
0.50	15.86	15.86	1.263	0.663
0.25	7.93	23.78	0.841	0.442
0	0	31.71	0.420	0.220

Table 4.3 – Table showing the flow rates for values of P between 0 and 1 and the corresponding concentration of NaCl after the Y-mixer **Y** and after the addition of $AgNO_3$ at **J** (the final concentration) for two pairs of concentrations of NaCl, (i) low and (ii) high. $Q_{Ag} = 28.70\,\mu\text{L/min}$, $Q_A + Q_B = 31.71\,\mu\text{L/min}$, $t_R = 13\,\text{min}$, and $T = 165\,^\circ\text{C}$.

higher reaction concentrations between 0.220 mM ($P = 0$) and 1.105 mM ($P = 1$) could be tested. The conditions which produced the longest AgNWs in Section 4.5, $T = 165\,^\circ\text{C}$ and $t_R = 13\,\text{min}$, were selected for these experiments.

As in previous experiments, flow rates were tested in a randomised order and the reactor was left for $1.5 \times t_R$ min after changing the flow rates for the reactor to reach steady state. Each sample was analysed using DFOM as described in Section 5.4.3. Figure 4.16 shows a graph of the median nanowire length versus the final concentration of NaCl in the droplets. The error bars extend to the first and third quartiles. The blue and green markers correspond to the experiments using the low (i) and high (ii) concentration pairs of precursors, respectively.

Using the low concentration pair of precursors (i), the concentration of NaCl in the segmented flow was varied between 0 and 0.220 mM. No an-

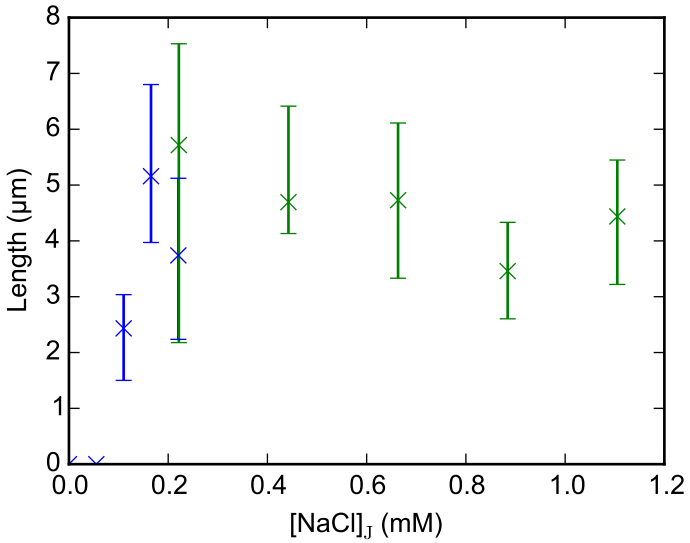


Figure 4.16 – Graph showing the median AgNW length versus the concentration of NaCl after the three-in-one-out junction. The error bars extend to the first and third quartiles. No AgNWs were obtained when the NaCl concentration was 0 and 0.055 mM. Blue and green markers correspond to the low (i) and high (ii) concentration pairs of syringes in Table 4.3.

isotropic particles were produced in the absence of NaCl or at the lowest concentration of 0.055 mM. A small number of AgNWs of median length 2.4 µm were observed when the concentration was 0.110 mM. An increase in NaCl concentration to 0.16 mM caused the median length to double to 5.2 µm, but a further increase to the highest concentration for this pair of precursors (0.22 mM, equal to the concentration used in previous experiments) produced AgNWs with a smaller median length of 3.7 µm.

Using the high concentration pair of precursors (ii), the NaCl concentration in the segmented flow was varied between 0.220 mM and 1.11 mM. AgNWs were obtained for all concentrations. The lowest concentration (0.220 mM) produced AgNWs of median length 5.7 µm. This was slightly longer than the same concentration obtained using the low concentration pair and demonstrated that there was some variation between the experiments. As the concentration was increased, there was a slight decrease in the median length. At the highest concentration (1.11 mM), the median length was 4.4 µm. Therefore, on the basis of AgNW length alone, the optimum NaCl concentration appeared to be *ca.* 0.220 mM.

Figure 4.17 shows DFOM images of the samples. (a–c) are images of the samples produced using the low concentration pair of precursors, which produced NaCl concentrations in the range 0.055 to 0.22 mM. (d–h) are images of the samples produced using the high concentration pair of precursors, which produced NaCl concentrations in the range 0.22 to 1.11 mM. (Note that the image of the sample produced without any NaCl is not shown, as it was visually identical to that produced at 0.055 mM.) The images show that the number of AgNWs produced relative to the number of nanoparticle by-products increased as the concentration of NaCl increased from 0 to 0.44 mM. As the concentration increased beyond 0.44 mM, the number of AgNWs relative to the number of nanoparticles decreased slightly.

Overall, it was found that a NaCl concentration of 0.44 mM produced AgNWs with the best shape-selectivity, while a 0.22 mM concentration produced the longest AgNWs. At 0.44 mM the median length was 4.7 µm compared to 3.7 µm and 5.7 µm (low and high concentration pairs of syringes, respectively) at 0.22 mM.

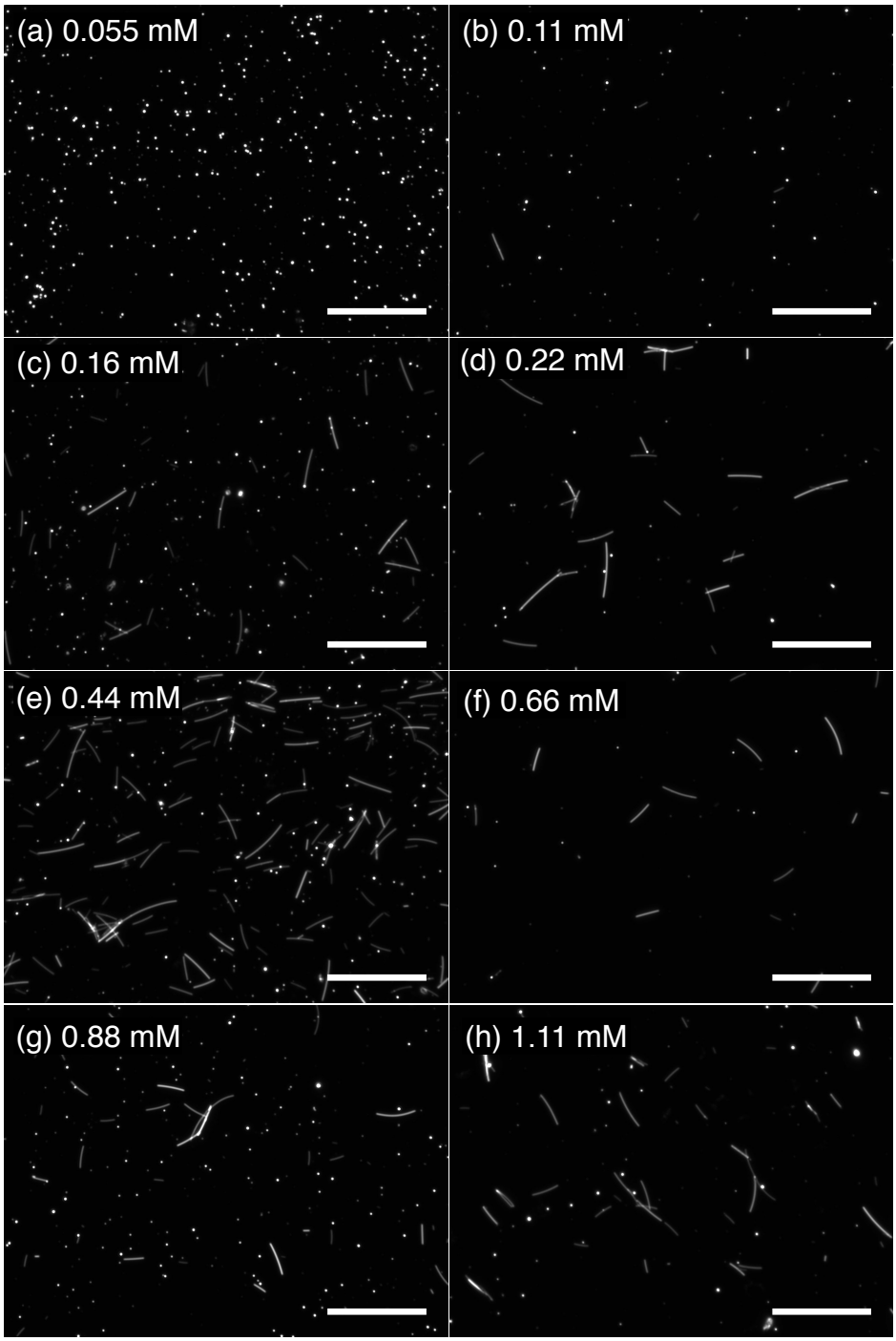


Figure 4.17 – DFOM images of samples produced using different concentrations of NaCl. The images show samples produced using concentrations of NaCl from 0.055 to 0.16 mM (a–c) and 0.22 to 1.11 mM (d–e) from the low (i) and high (ii) concentration precursor pairs. Scale bars: 20 µm.

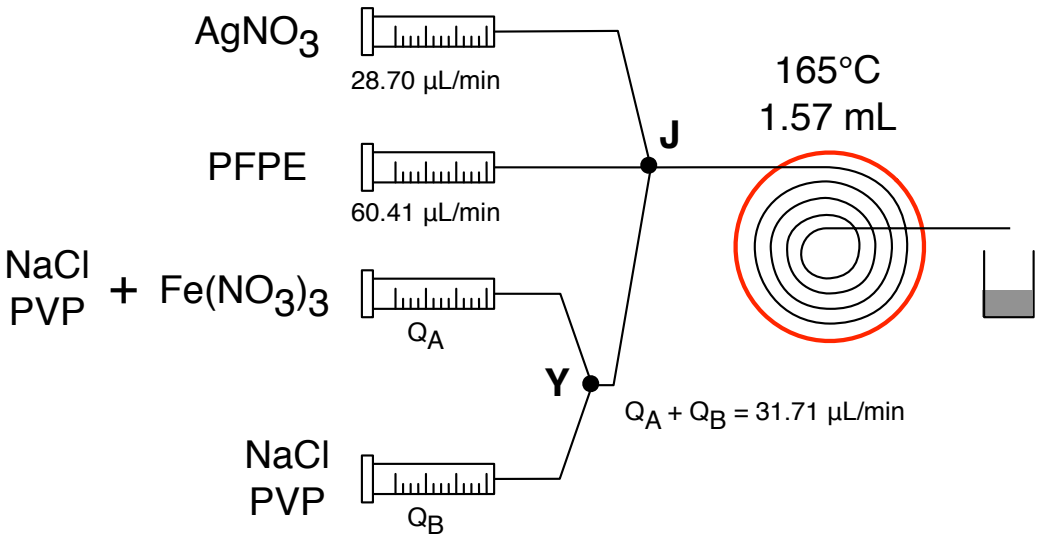


Figure 4.18 – Schematic of the reactor used to vary the concentration of $Fe(NO_3)_3$ in the droplets. Solutions of $AgNO_3$ and PFPE carrier fluid were injected into a three-in-one-out junction **J**. One syringe containing the standard concentrations of NaCl, PVP, and $Fe(NO_3)_3$, and another containing standard concentrations of NaCl and PVP, but no $Fe(NO_3)_3$, were injected into a Y-mixer **Y**. The outlet of **Y** is connected to the third inlet of **J**. The outlet of **J** is connected to 2 m of 1 mm PTFE tubing (1.57 mL) mounted in a metal frame and submerged in an oil bath ($T = 165\,°C$ and $t_R = 13\,min$). The product was collected into a vial of water.

4.6.2 Iron nitrate

The effect of varying $Fe(NO_3)_3$ was investigated next since, as described in Section 2.3, the presence of ionic species like $Fe^{2+/3+}$ is crucial in the polyol synthesis to protect decahedral seeds from dissolution via O_2. The concentration of $Fe(NO_3)_3$ used in the reactions reported above may not have been optimal for obtaining long AgNWs, so it was chosen as the next parameter to investigate.

Figure 4.18 shows a schematic of the reactor used to vary the $Fe(NO_3)_3$ concentration in the reaction. Precursor B (containing NaCl, PVP, and $Fe(NO_3)_3$) was replaced with a pair of precursors containing the previously used concentration of NaCl (0.420 mM) and PVP (74.6 mM), but different concentrations of $Fe(NO_3)_3$. The $Fe(NO_3)_3$ concentration was 38.39 µM in

	Flow rate (µL/min)		[$Fe(NO_3)_3$] (µM)	
P	Q_A	Q_B	After **Y**	After **J**
1.00	31.70	0	38.39	20.15
0.75	23.78	7.93	28.79	15.11
0.50	15.85	15.85	19.20	10.07
0.25	7.93	23.78	9.60	5.04
0	0	31.70	0	0

Table 4.4 – Table showing the flow rates for values of P between 0 and 1 and the corresponding concentration of $Fe(NO_3)_3$ after the Y-mixer **y** and after the addition of $AgNO_3$ at **J** (the final concentration). $[Fe(NO_3)_3]_A$ = 38.39 µM and $[Fe(NO_3)_3]_B = 0$. $Q_{CF} = 60.41$ µL/min, $Q_{Ag} = 28.70$ µL/min, and $T = 165$ °C.

syringe A, but no $Fe(NO_3)_3$ was added to syringe B. Therefore the $Fe(NO_3)_3$ concentration at the outlet of the Y-mixer could be varied between 0 and 38.39 µM. The outlet of the Y-mixer ($Q_A + Q_B = 31.71$ µL/min) flowed into the three-in-one-out junction where it combined with the $AgNO_3$ flow ($Q_{\mathrm{Ag}} = 28.70$ µL/min). At this junction $P = 0.525$, and since the $AgNO_3$ precursor did not contain any $Fe(NO_3)_3$, it follows from Equation 4.1 that the $Fe(NO_3)_3$ concentration decreased to $0.525 \times [Fe(NO_3)_3]_Y$, resulting in an $Fe(NO_3)_3$ concentration in the segmented flow between 0 to 20.15 µM.

Table 4.4 shows the five sets of flow rates used across the possible range of $Fe(NO_3)_3$ concentrations. It also shows the corresponding concentration of $Fe(NO_3)_3$ at the outlet of the Y-mixer and after the addition of $AgNO_3$ (the final concentration). The conditions that produced the longest AgNWs in Section 4.5, $t_R = 13$ min and $T = 165$ °C, were also used here.

Figure 4.19 shows box and whisker plots of AgNW length for each concentration of $Fe(NO_3)_3$ tested. When no $Fe(NO_3)_3$ was added, the median length was 3.8 µm. For the lowest the $Fe(NO_3)_3$ concentration of 5.04 µM, the median length increased to 5.7 µm. But further increases in the concentration of $Fe(NO_3)_3$ up to 20.15 µM did not yield any significant changes in length, with the median values being around 6 µm. The observed sample-to-sample variation was similar to that observed during stability testing (Section 4.4).

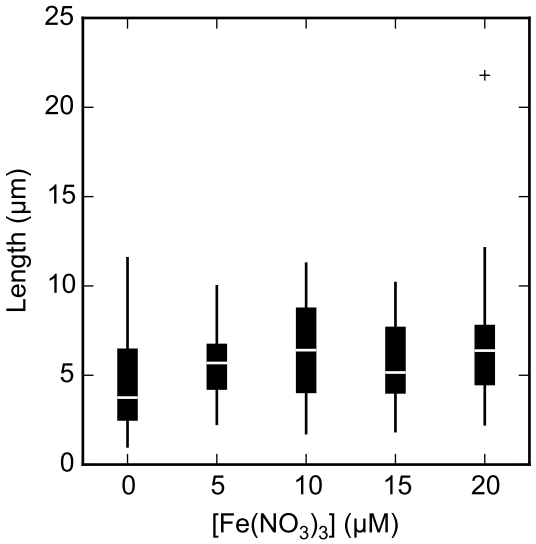


Figure 4.19 – Box and whisker plots showing the length of AgNWs produced at $Fe(NO_3)_3$ concentrations from 0 to 20 µM (T =165 °C and t_R = 13 min).

Figure 4.20 shows DFOM images of the samples produced for each concentration of $Fe(NO_3)_3$. All of the images show a similar number of AgNWs relative to the number of nanoparticles, providing little evidence for a relationship between AgNW-selectivity and $Fe(NO_3)_3$ concentration.

4.6.3 Ionic species in ethylene glycol

In Chapter 3 I reported significant differences in AgNWs length and selectivity for nominally identical reactions using two different lots of EG. Lot A (BCBN5970V) produced AgNWs twice as long as those obtained with lot B (BCBN2592V). The specification sheets showed that the EG could contain concentrations of Cl and Fe several orders of magnitude higher than the usual concentration of NaCl and $Fe(NO_3)_3$ added to the reactions. Lot A was used in this Chapter. The results above show that varying the concentration of $Fe(NO_3)_3$ had almost no effect on both AgNW length and selectivity. Experiments changing the concentration of NaCl showed that NaCl must be added to produce AgNWs. This suggests that lot A may have contained a high concentration of $Fe^{2+/3+}$, rather than Cl^-.

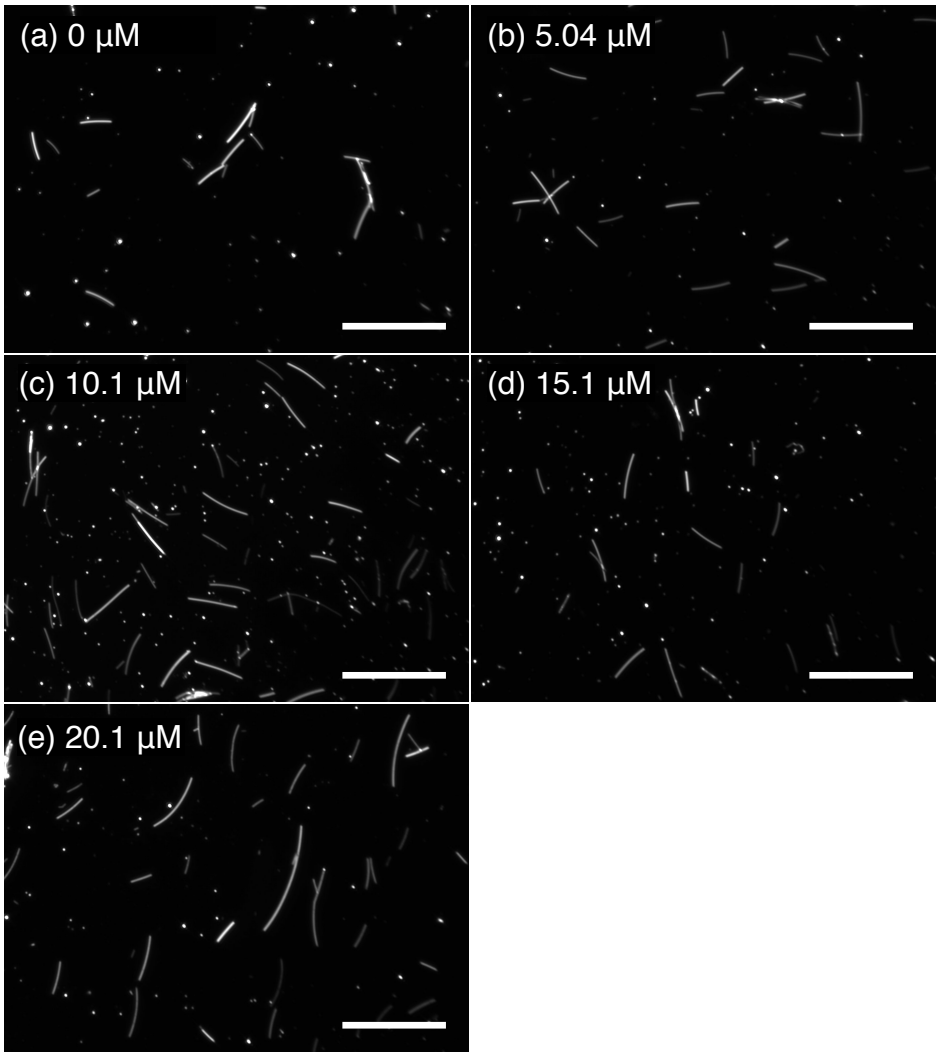


Figure 4.20 – DFOM images of samples produced using different concentrations of $Fe(NO_3)_3$, from 0 to 20.1 µM (a–e). Scale bars: 20 µm.

4.7 Conclusions

In Chapter 3 I described the development of a straightforward heat-up batch process to produce AgNWs. In this chapter I described its successful adaptation to flow using a variety of reactor configurations. The first flow reactor used a single precursor mixture, but this was found to be unstable and would most likely result in variation of the product over time.

On the basis of a previous study that had shown the reduction of $AgNO_3$ by PVP, I modified the reactor design to include an additional syringe containing $AgNO_3$ separate from the other reagents. Using this dual-precursor reactor, AgNWs were produced using residence times between 13 and 20 min at 170 °C. The observed variation in length suggested that growth had stopped after 13 min, the approximate time at which gas evolution became observable, a probable cause of oxidative etching of the AgNWs. The AgNWs produced using a 20 min residence time had a median length of 6.0 µm. Stability tests showed that this reactor produced consistently AgNWs over an 8 h period without any sign of reactor fouling.

The good stability of the reactor allowed me to carry out a systematic investigation into the effect of key reaction parameters. Samples were obtained using combinations of residence times between 13 and 25 min and temperatures between 150 and 170 °C. The longest AgNWs with a median length of 6.2 µm were obtained using a 13 min residence time and 170 °C temperature. There was no discernible effect of either parameter on the number of nanoparticle by-products.

The reactor was modified so that the concentration of NaCl and $Fe(NO_3)_3$ could be varied independently of the other reactants. A NaCl concentration of at least 0.110 mM was required to obtain AgNWs. The longest AgNWs of median length 5.7 µm were produced when the concentration was 0.22 mM, which was in close agreement with the batch procedure. A slightly higher NaCl concentration of 0.44 mM produced fewer nanoparticle by-products, but at the expense of AgNW length which fell to 4.7 µm. AgNWs were produced even when $Fe(NO_3)_3$ was absent, but the addition of $Fe(NO_3)_3$ at 5 mM increased the median length to 5.7 µm. Higher concentrations of up

to 20 mM did not result in a significant increase in length. The number of nanoparticle by-products remained roughly constant, regardless of $Fe(NO_3)_3$ concentration. Overall, the longest AgNWs which had a median length of 6.1 µm were produced using a 13 min residence time and 165 °C temperature. These AgNWs were shorter than those produced in batch using the hot-injection (4.1 µm) and heat-up (9.1 µm) reaction procedures.

In summary, I developed a reliable method for the continuous production of AgNWs using a droplet flow microreactor and evaluated a range of reaction conditions and parameters. Although further optimisation is still required to achieve long AgNWs, the reactor potentially offers a more controlled environment for AgNW synthesis than conventional batch reactions. The following section describes promising areas for future study.

4.8 Further work

4.8.1 Other reaction parameters

The reactor used in Section 4.6 to vary the concentration of NaCl and $Fe(NO_3)_3$ could also be used to investigate the effect of varying the ratio of $AgNO_3$ to PVP. PVP plays a critical role in passivating the {100} facets of MTPs. Too little PVP results in isotropic growth, whereas too much PVP also passivates {111} facets thus preventing anisotropic growth.[68] The concentration used for the experiments reported in this thesis not have been optimal for minimising the number of nanoparticle by-products. Furthermore, by adjusting the ratio of $AgNO_3$ to PVP it may be possible to control the diameter of the AgNWs produced. A higher concentration of $AgNO_3$ and PVP may also enable growth of longer AgNWs.

This work used PVP with an average molecular weight of 55 kDa. Different average molecular weights may produce longer AgNWs with fewer by-products. For example, Ran *et al.* found that a 2:1 mixture (by mass) of 360 kDa and 55 kDa PVP produced AgNWs with diameters of around 25 nm and lengths around 40 µm.[91] The flow reactor could be used to carry out reactions with different ratios of different molecular weight PVP solutions.

The investigation into the effect of varying reaction temperature and residence time described in Section 4.5 showed that AgNWs synthesis was substantially complete at $t_R = 13\,\text{min}$ and $T = 170\,^\circ\text{C}$. This suggests that it may possible to produce AgNWs using residence times shorter than 13 min, which would enable higher rates of production.

4.8.2 Extinction spectra and inline analysis

Investigation of the areas above would be more efficient if it were possible to analyse the product in real time as it travels through the outlet channel. As I described in Section 1.4, optical techniques are particularly straightforward to integrate with microfluidic reactors. With this in mind, the extinction spectra of many AgNW samples produced during the course of this work were recorded. Figure 4.21 shows extinction spectra of crude samples produced at (a) 150 °C and (b) 165 °C using residence times from 13 to 25 min. These spectra were typical of the samples produced. Large changes were observed in the extinction spectra of samples produced using shorter residence times, particularly at lower temperatures when the reaction rate was slower. These changes were expected, as anisotropic growth of an isotropic MTP would significantly alter the surface plasmon resonance modes and hence the wavelengths of light absorbed. At higher temperatures the AgNWs grew relatively quickly, and the spectra typically showed little variation, like the spectra shown in Figure 4.21 (b). Unfortunately I was unable to establish a clear trend between the extinction spectra and information obtained using DFOM and SEM, particularly as AgNWs grew longer. This may be due the inherent polydispersity of the AgNW–nanoparticle mixture and/or loss of surface plasmon resonance as the AgNWs reached a particular length.

Separation of the product mixture by shape and size (by centrifugation or filtration) followed by optical analysis of the components may enable one to establish the origin of the spectral features. If successful, the extinction spectrum of a crude sample could possibly be used to estimate the length of the AgNWs produced and the number of nanoparticle by-products. Light scattering measurements could also be an alternative method of analysis. In-

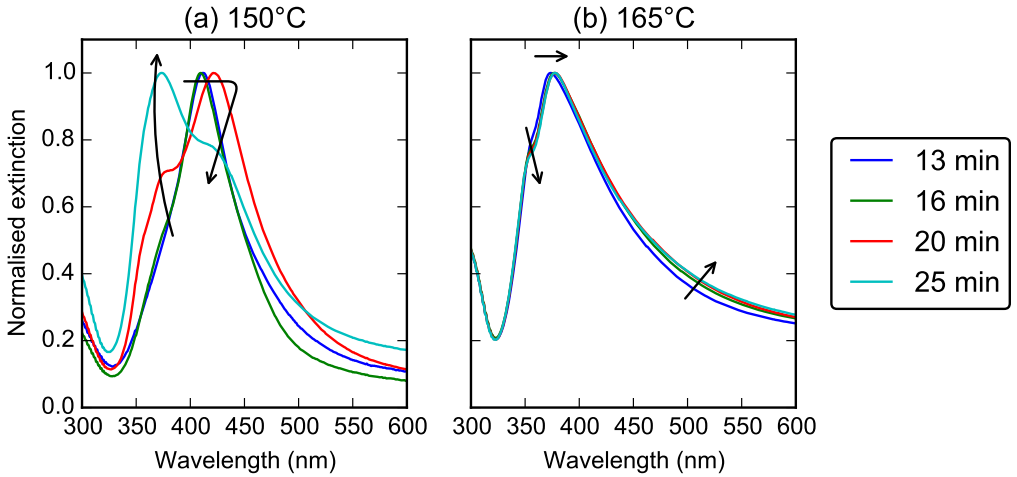


Figure 4.21 – Normalised extinction spectra of crude samples produced at (a) 150 °C and (b) 165 °C using residence times from 13 to 25 min. The arrows are a guide to the eye and show the change in the spectral features as the residence time increased.

line analysis would enable faster evaluation of different reaction conditions and, in combination with a computer-controlled feedback-loop, could be used to implement a self-optimising reactor that autonomously finds the best conditions to produce long AgNWs with as few nanoparticle by-products as possible.

4.8.3 Adsorption of AgNWs at the EG-PFPE interface

Preliminary experiments were carried out in continuous flow. The reactor channels blocked within approximately 30 min of reactor operation. Visual examination of the tubing revealed significant deposition of grey material on the channel walls and demonstrated the effectiveness of segmented flow at preventing fouling. Nonetheless, segmented flow produces a large EG-PFPE interface and interfacial adsorption of nanoparticles is a well-documented phenomenon.[92] Zhang *et al.* reported that the addition of a non-ionic surfactant (Triton X-100) in an water-in-oil droplet synthesis of Ag nanocubes reduced polydispersity. They argued that the surfactant passivated the oil-water interface and prevented the adsorption of the nanoparticles.[15] In this

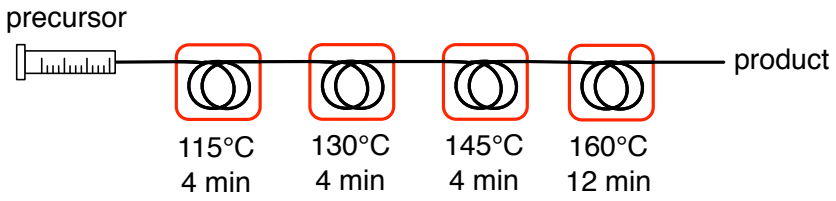


Figure 4.22 – Schematic of the continuous flow reactor used for preliminary investigation into the effect of multiple temperature zones. Precursor solution ($AgNO_3$, PVP, NaCl, and $Fe(NO_3)_3$) is injected at 100 µL/min into a length of tubing (4 m) is immersed in four consecutive temperature-controlled oil baths. 0.5 m tubing is immersed in each of the first three oil baths and 1.5 m tubing is immersed in the final oil bath. Product is collected at the outlet.

work, the AgNWs produced in flow were shorter than those grown in batch. It may be the case that the AgNWs were adsorbed at the EG-PFPE interface, thus slowing growth. Similarly to the work by Zhang and co-workers, it may be possible to produce longer AgNWs by adding a non-ionic surfactant to the PFPE and/or EG.

4.8.4 Multiple temperature zone flow reactor

In Section 3.2.2 I compared the temperature profile of the hot-injection and heat-up reactions and concluded that the lower temperature at the start of the heat-up reaction was preferable for longer AgNW growth. Both of these temperature profiles are markedly different from the one I employed in flow. The high surface area to volume ratio of a microfluidic channel results in fast heat transfer. Hence the reaction mixture flowing through the channel reaches the temperature of the oil bath almost immediately. On the basis of the batch results it is possible that a microfluidic reactor with multiple temperature zones may be preferable for the production of longer AgNWs.

Figure 4.22 shows a schematic of the reactor used to carry out preliminary experiments to test this hypothesis.[b] Precursor solution (identical to the precursor used in the batch heat-up reaction described in Section 3.2) was

[b]These experiments were carried out before the EG lot number was identified as a factor that significantly affects the reaction and prior to the adoption of a dual precursor configuration.

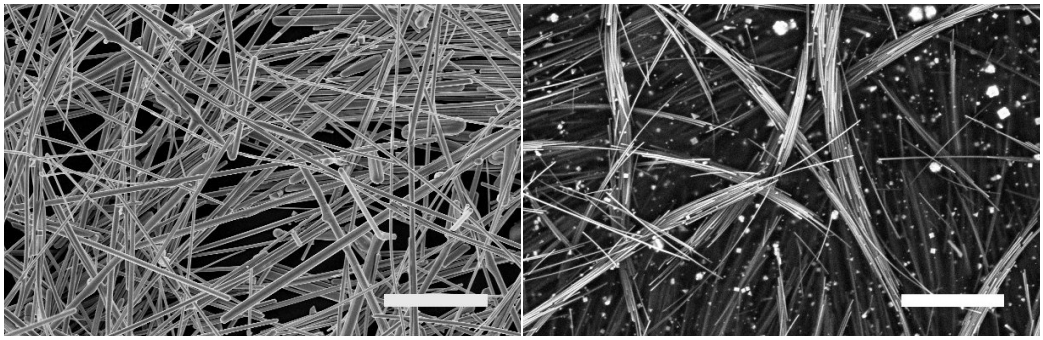


Figure 4.23 – SEM images of product obtained from constant (left) and progressively increasing (right) temperatures across four consecutive oil baths. Scale bar: 5 µm.

injected at 100 µL/min into a length of tubing immersed in four consecutive temperature-controlled oil baths. So that the reaction temperature gradually increased, the oil baths were set to 115 °C, 130 °C, 145 °C, and 160 °C. To give finer control over the temperature profile at the start of the reaction, the first three oil baths had a residence time of 4 min whereas the final oil bath had a residence time of 12 min.

Figure 4.23 shows SEM images of the product obtained from constant (160 °C, left) and progressively increasing (right) oil bath temperatures. The AgNWs produced using a constant temperature had a mean diameter of 160 nm whereas those produced using an progressively increasing temperature profile had a mean diameter of 45 nm. The standard deviation was 64 and 8 nm, respectively. This suggests that a multiple temperature zone configuration may enable control over the diameter of the AgNWs produced and also reduce polydispersity. Fouling was a significant problem, however, and led to the channel becoming completely blocked within *ca.* 1 h of operation.

Chapter 5

Experimental Methods

5.1 Reagents and materials

EG (≥99.5 %, product number 03750), PVP (average M_w 55 kDa), and iron(III) nitrate nonahydrate (≥99.95 %) were obtained from Sigma-Aldrich. NaCl (≥99.5 %) and acetone (≥99.5 %) were obtained from VWR. Deionized and ultrapure water were obtained from a Millipore Direct-Q UV 3 system.

5.2 Batch syntheses

5.2.1 General procedures

All glassware, PTFE-coated stirrer bars, and glass gas-tight syringes were scrubbed with hot soapy water and then rinsed with tap water, deionized water, concentrated nitric acid, deionized water, and lastly ultra-pure water, before being dried in an oven overnight. Glassware was allowed to cool to room temperature before use. All solids were weighed onto pergamyne weighing paper (Whatman) using single-use polypropylene spatulas (VWR).

5.2.2 Comparison of heat-up and hot-injection methods

Stock solutions of NaCl (0.2572 g, 20 mL EG, 0.22 M), $Fe(NO_3)_3$ (0.0838 g, 10 mL EG, 21 mM), and PVP (1.0479 g, 25 mL EG, 0.38 M) were prepared

by stirring at room temperature in stoppered round-bottomed flasks (RBFs) until dissolved. $AgNO_3$ solution (0.2520 g, 6 mL EG, 0.25 mM) was prepared as required by stirring at room temperature.

An oil bath on a temperature-controlled hotplate (IKA) was heated to 170 °C. Preliminary experiments showed that this oil bath temperature resulted in a flask temperature of 160 °C. To two two-neck 50 mL RBFs (each equipped with a stirrer bar, thermometer, and stopper) was added 15.84 mL EG. Both flasks were stirred at 270 revolutions per minute (rpm). One flask (hot-injection reaction) was immersed in the oil bath for preheating and the other (heat-up reaction) was stirred at room temperature. After 1 h preheating, 20 µL NaCl, 10 µL $Fe(NO_3)_3$, 2075 µL PVP, and 2075 µL $AgNO_3$ solution were added to each flask. The final concentrations were 25.6 mM $AgNO_3$, 39.1 mM PVP, 10.4 µM $Fe(NO_3)_3$, and 0.22 mM NaCl. Immediately after the addition of the $AgNO_3$ solution the cold flask was immersed in the oil bath. Aliquots (*ca.* 0.5 mL) were removed from each reaction flask using a Pasteur pipette and quenched in glass vials containing 1 mL room temperature water.

5.2.3 Modified heat-up method

Stock solutions of NaCl (25.8 mg, 50 mL EG, 8.83 mM), $Fe(NO_3)_3$ (16.2 mg, 100 mL EG, 0.401 mM), and PVP (0.4574 g, 50 mL EG, 82.3 mM) were prepared by stirring at room temperature in screw-cap glass bottles until dissolved. These larger volumes of EG were added by mass (1.11 g/mL) on a 0.01 g precision mass balance as using volumetric addition (e.g. measuring cylinders) was difficult due to the high viscosity of EG. $AgNO_3$ solution (91.6 mg, 10 mL, 53.9 mM) was prepared as required by stirring at room temperature.

To a two-neck 50 mL RBF equipped with a stirrer bar and stoppers was added 0.5 mL NaCl, 0.5 mL $Fe(NO_3)_3$, 9.51 mL PVP, and 9.51 mL $AgNO_3$ solution whilst stirring. The final concentrations were 25.6 mM $AgNO_3$, 39.1 mM PVP, 0.22 mM NaCl, and 10.0 µM $Fe(NO_3)_3$. The flask was immersed in the oil bath (170 °C, 270 rpm). Aliquots (*ca.* 0.5 mL) were removed

from each reaction flask using a Pasteur pipette and quenched in glass vials containing 1 mL room temperature water.

5.3 Flow syntheses

5.3.1 General procedures

Gas-tight syringes with glass PTFE-tipped barrels were obtained from Hamilton and SGE. Standard flangeless and super-flangeless fluidic fittings were used throughout (Upchurch). All Y-mixers were made of PEEK and obtained from Upchurch (P-512, $V = 1.7\,\mu L$). Solutions were infused using Harvard Pump 11 Plus and Harvard PHD2000 syringe pumps. PTFE tubing was obtained from Polyflon or Bohlender and was of 1 mm ID and 2 mm OD. PTFE tubing was heated by immersing it in a well-stirred silicone oil (Sigma-Aldrich) bath heated using a temperature-controlled hotplate stirrer (IKA). Metal wire (RS) was used to secure the tubing in a coil (to prevent it moving out of the oil bath) or mounted in the spiral frame shown in Figure 4.5. Galden HT270 (Solvay) PFPE carrier fluid was degassed under vacuum with vigorous stirring, and sparged with Ar for several hours before use. Unless stated otherwise, all EG was from lot BCBN5970V (Sigma Aldrich, 03750). Stock solutions were prepared by stirring overnight in capped glass bottles. Precursors were mixed in RBFs and loaded into syringes.

5.3.2 Three-in-one-out junction

Three-in-one-out junctions were fabricated in-house using a four-axis CNC mill from PEEK round stock (50 mm diameter, RS) to the design in Ref. 35. As shown in Figure 5.1, three inlets and a single outlet were drilled to a 5 mm diameter and 10 mm depth and threaded using a 1/4"-28 tap. Internal channels were drilled to a 1 mm diameter. Precursor streams met the central channel at a 60° angle.

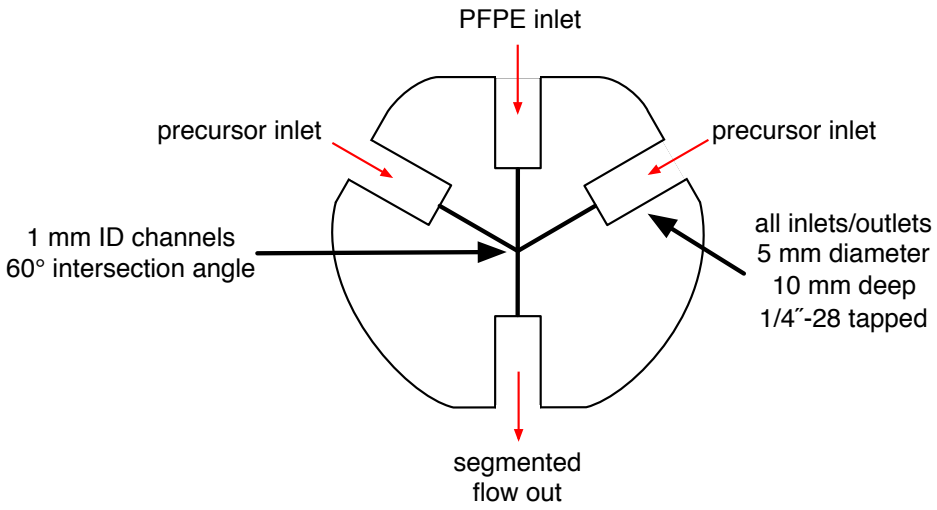


Figure 5.1 – Diagram showing the cross-section of the three-in-one-out junction. Each junction was machined from PEEK round stock (50 mm diameter) and drilled and tapped for standard fluidic fittings.

5.3.3 Single-precursor preparation

The precursor was prepared using the same method that was used to prepare the reaction mixture for the modified batch heat-up reaction (Section 5.2.3). Since $AgNO_3$ reacts with NaCl to form AgCl, which is reduced to Ag upon exposure to light, the syringe was wrapped in aluminium foil.

5.3.4 Dual-precursor preparation

Stock solutions of PVP (0.9164 g, 100 mL EG, 82.5 mM), $Fe(NO_3)_3$ (16.2 mg, 100 mL EG, 0.401 mM), and NaCl (25.7 mg, 50 mL EG, 8.80 mM) were prepared. Precursor A was $AgNO_3$ solution (91.6 mg, 10 mL EG, 53.9 mM). As a precaution the syringe was wrapped in aluminium foil to prevent exposure to light. Precursor B was 9.51 mL PVP, 0.5 mL NaCl, and 0.5 mL $Fe(NO_3)_3$. After mixing, the concentrations were 74.6 mM PVP, 0.418 mM NaCl, and 19.1 µM $Fe(NO_3)_3$. The flow rate ratio of precursor A to precursor B was constant ($Q_A/Q_B = 0.905$) so that the concentration of the reactants was equal to those used in the batch reaction in Section 5.2.3 (25.6 mM $AgNO_3$, 39.2 mM PVP, 0.220 mM NaCl, and 10.0 µM $Fe(NO_3)_3$).

5.3.5 Stability testing

Solutions in this experiment used EG from lot BCBN6058V. Precursor A was $AgNO_3$ solution (0.5663 g, 39 mL, 85.5 mM) and was wrapped in aluminium foil as a precautionary measure. Stock solutions of PVP (0.2613 g, 15 mL, 156 mM), NaCl (0.1288 g, 10 mL, 220 mM), and $Fe(NO_3)_3$ (0.2613 g, 15 mL, 157 mM) were prepared. Precursor B was 15 mL PVP, 60 µL NaCl, and 30 µL $Fe(NO_3)_3$ and, after mixing, was 156 mM PVP, 0.876 mM NaCl, and 39.8 µM $Fe(NO_3)_3$. The flow rates of precursor A and precursor B were Q_A = 39.37 µL/min and Q_B = 12.99 µL/min, respectively. Reaction concentrations were therefore 64.3 mM $AgNO_3$, 38.7 mM PVP, 0.217 mM NaCl, and 9.86 µM $Fe(NO_3)_3$.

5.3.6 Varying concentration of ionic additives

Sodium chloride

$AgNO_3$ solution and stock solutions of PVP, NaCl, and $Fe(NO_3)_3$ and were prepared as described in Section 5.3.4. An additional NaCl solution (0.129 g, 50 mL, 44.1 mM) was prepared. For each experiment, two precursors of differing NaCl concentrations, but the same concentration of PVP and $Fe(NO_3)_3$, were prepared by mixing 0.5 mL $Fe(NO_3)_3$ and 9.51 mL PVP, followed by a quantity of EG or NaCl. For pair (i): 0.5 mL 8.80 mM NaCl (precursor A) or 0.5 mL EG (precursor B). For pair (ii): 0.5 mL 44.1 mM NaCl (precursor A) or 0.5 mL 8.80 mM NaCl (precursor B).

Iron nitrate

$AgNO_3$ solution and stock solutions of PVP, NaCl, and $Fe(NO_3)_3$ were prepared as described in Section 5.3.4. An additional $Fe(NO_3)_3$ solution (0.0324 g, 100 mL EG, 0.802 mM) was prepared by stirring the solid overnight in a glass bottle. Two precursors of differing $Fe(NO_3)_3$ concentrations, but the same concentration of PVP and NaCl, were prepared by mixing 0.5 mL NaCl and 9.51 mL PVP, followed by 0.5 mL 0.802 mM $Fe(NO_3)_3$ (precursor A) or 0.5 mL EG (precursor B).

5.4 Techniques

5.4.1 Forward and reverse pipetting

Precursors were added to the reaction flasks using a piston-driven air displacement pipette (Eppendorf Research). The results of the gravimetric analysis reported in Section 3.3.1 identified significant random variation in the volume of EG and precursor added to the reactions. In Section 3.3.2 I described the modification of the pipetting procedure to reduce the error. This included switching from forward to reverse pipetting.

Figure 5.2 illustrates the forward and reverse pipetting techniques. In both techniques, a new tip is first attached to the pipette. Using the forward pipetting technique (a), the plunger is pushed to the first stop (1). The tip is then inserted into the liquid and the plunger slowly released to the ready position (2). The pipette is removed from the liquid and the tip now contains the chosen volume of liquid. The pipette is moved to the destination flask where the plunger is pressed to the first stop (3) to eject the liquid, and then to the second stop (4) to expel all liquid from the tip. Then plunger is then released (5) and the tip disposed of. Using the reverse pipetting technique (b), the plunger is first pushed to the second stop (1). The tip is inserted into the liquid and the plunger slowly released to the ready position (2). The tip is removed from the liquid and the pipette moved to the destination flask. The liquid is expelled by pushing the plunger to the first stop (3) and removed from the flask. The remaining liquid in the tip is expelled into a waste container by pushing the plunger to the second stop (4). The plunger is released to the ready position (5) and the tip disposed of.

5.4.2 Washing of crude samples

Crude product mixture (*ca.* 20 mL) was diluted by acetone (in a ratio of 1:5) and mixed using a vortex mixer, which caused the AgNWs to flocculate. The mixture was distributed equally amongst three centrifuge tubes and isolated by centrifugation (4990g for 40 min) to obtain a wet grey solid. The product was then was washed (∼30 mL per tube) and isolated by centrifuga-

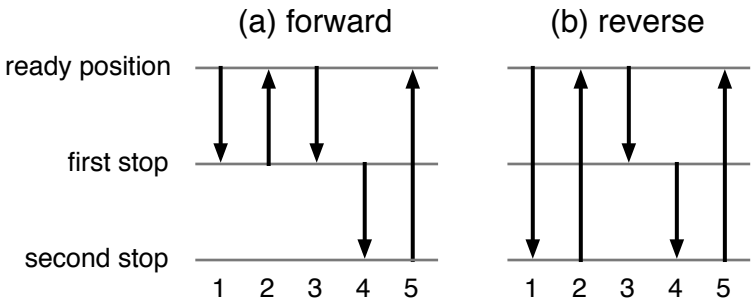


Figure 5.2 – Diagram showing the position of the pipette plunger when dispensing liquids using the forward (a) and reverse (b) pipetting techniques.

tion (4990g for 20 min) a further two times using acetone and then ultrapure water. The isolated solid was then dispersed in ultrapure water.

5.4.3 Dark field optical microscopy

An optical microscope uses visible light and lenses to magnify an image of a specimen. Bright field optical microscopy is the most common type of optical microscopy. Figure 5.3 (a) shows a diagram of the light path inside in a bright field microscope. Light from a lamp is focussed by a condenser lens onto the sample. Most of the light is transmitted through the sample and is focussed by an objective lens to form an image. The sample absorbs a fraction of the light, creating contrast in the image, due to dark objects against a bright background. Metal nanoparticles do absorb visible light, but they are too small to be resolved via this contrast mechanism.

Figure 5.3 (b) shows a diagram of the light path inside a DFOM. The configuration is the same as in a bright field optical microscope, but with the addition of two components. A stop is placed between the lamp and condenser to create a hollow cone of light that illuminates the sample. (Note that in practice the stop and condenser are a single component called a dark field condenser.) Metal nanoparticles scatter the incident light. An aperture is then inserted between the sample and objective to prevent the light from the lamp entering the objective lens, so that only light scattered by the nanoparticles is focussed by the objective lens to form an image. The nanoparticles appear as bright objects on a dark background.

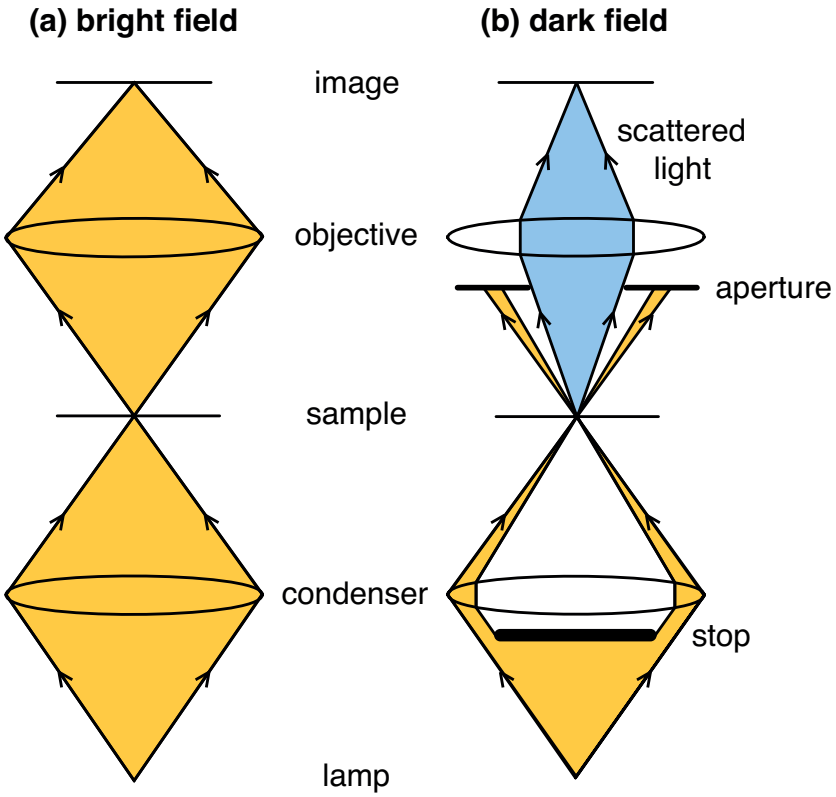


Figure 5.3 – Diagrams showing the light path through an optical microscope in (a) bright field and (b) dark field modes.

Crude samples were diluted in ultrapure water. Using a Pasteur pipette, a single drop was applied to a glass microscope slide and immediately pipetted off again, leaving nanowires and nanoparticles on the surface of the slide. These were examined using an Olympus BX51 microscope fitted with a dark field condenser (Olympus U-DCW) and 50x (NA 0.8) and 100x (NA 0.9) objectives (Olympus MPlanFL N). Grayscale images were recorded using QImaging QIClick camera.

AgNWs were measured using ImageJ software. The objectives were calibrated using a 1 mm stage micrometer with 10 µm divisions (Thorlabs). These measurements were then used to set the scale in ImageJ. Care was taken to avoid biased measurement of longer or shorter AgNWs. Starting at a corner of the image, an area was enlarged and the length of all nanoparticles with an aspect ratio greater than one in the enlarged area were measured using the line tool. AgNWs that were cut off the edge of the image or only partially visible were not measured. The image was then panned to a new part of the image immediately adjacent to measure more AgNWs (resulting in a raster-like scan across the image) until a total of 30 AgNWs had been measured. Figure 5.4 shows a graph of the mean and median AgNW length from the measurement of up to 60 AgNWs. The graph shows that the mean and median fluctuate until around 20 measurements have been made. A total of 30 AgNWs was therefore chosen as a reasonable compromise between reliably determining the length of the AgNWs and obtaining a rapid analysis.

5.4.4 Scanning electron microscopy

Samples were prepared by drop-casting solution onto a silicon substrate (Agar Scientific) and dried overnight under vacuum. Samples were analysed using a LEO Gemini 1525 field emission gun SEM (5 kV EHT and in-lens detector).

5.4.5 Nuclear magnetic resonance spectroscopy

NMR spectra were recorded using a Bruker AV-400 (400 MHz) instrument. Samples were diluted in deuterated chloroform (Merck).

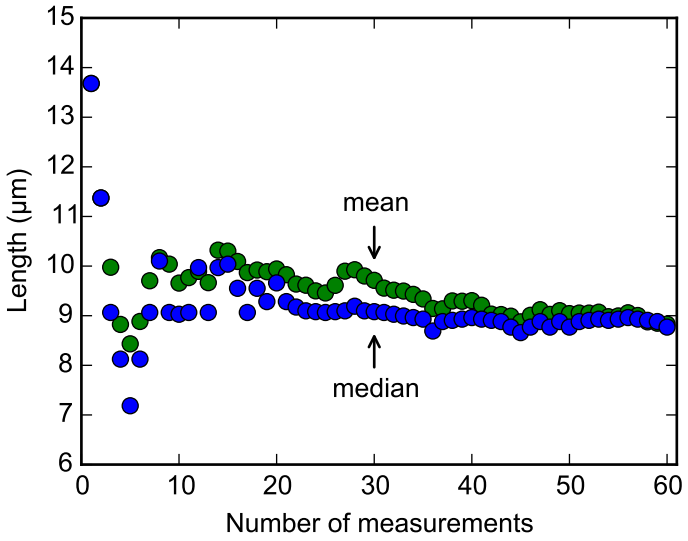


Figure 5.4 – Graph showing the mean and median length for 1 to 60 AgNW measurements. Measurements were made from an image of the sample taken at $t_R = 20\,\text{min}$ from the heat-up reaction in Section 3.2.

5.4.6 UV-visible spectroscopy

Ultraviolet-visible extinction spectra were recorded with a Jobin-Yvon Fluoromax-2 fluorimeter. A photodiode in the fluorimeter was used to monitor the transmitted light through the cuvettes to obtain extinction spectra. Samples were diluted in ultrapure water and measured using quartz cuvettes (10 mm path length, Lightpath Optical).

Chapter 6

Microscale Extraction and Phase Separation Using a Porous Capillary

6.1 Note

The work presented in this chapter was published in Ref. 93. Figures 6.13 to 6.19 have been reproduced from it under a Creative Commons Attribution 3.0 Unported Licence.[a] The data and MATLAB code to reproduce these figures is available to download from Ref. 94.

6.2 Introduction

As discussed in Chapter 2, the co-injection of two immiscible liquids into a narrow channel causes one or both components to segment into a train of discrete droplets or slugs. The resulting two-phase fluid stream offers many advantages over conventional single-phase fluid streams for both analytical and synthetic chemistry. But in many cases, it subsequently becomes necessary to separate the immiscible liquids, while keeping at least one of the liquids flowing in a stable and controlled manner. Key applications of liquid–

[a] http://creativecommons.org/licenses/by/3.0/

liquid separation include: (i) multistep chemical processing, where it may be impractical to carry out every step within the segmented flow regime and a continuous flow would be more suitable; (ii) inline analysis, where switching to continuous flow can greatly simplify detection by removing the need for sophisticated detectors synchronised to the droplet or slug flow; and (iii) separation of the phases after purification processes like washing or liquid–liquid extraction.

Methods for achieving liquid–liquid separation in a continuous inline process fall into two main categories: gravity-based methods, which use the difference in the density of the two liquids to achieve separation (*cf.* separating funnels in conventional batch chemistry); and wetting-based methods that exploit differences in surface wetting of the two liquids on hydrophobic or hydrophilic materials.

6.2.1 Gravity-based separators

In a typical gravity-based separator, the two-phase flow is introduced into a separating chamber with vertically offset outlets. The denser liquid sinks to the bottom of the chamber and exits through the lower outlet, while the lighter liquid exits through the upper outlet. For example, Hall *et al.* reported a continuous biphasic photocatalytic reaction where the photocatalyst was dissolved in a fluorous liquid.[95] To reuse the photocatalyst, they collected the organic–fluorous stream of product and photocatalyst into a glass flask, where the denser fluorous liquid sunk to the bottom and the organic product floated on top. The fluorous liquid was subsequently pumped out of the flask and recycled in a closed-loop. Nightingale *et al.* used a similar approach to recycle fluorous carrier fluid used in the large-scale droplet synthesis of semiconductor nanocrystals.[46]

These gravity-based separators are best suited to situations where large amounts of liquid (>10 mL) are collected over extended periods of time. In 2012 O'Brien *et al.* reported a lower volume gravity-based separator better-suited for synthetic flow chemistry.[96] Figure 6.1 shows a schematic of their separator (integrated within a flow reactor for the synthesis of hydrazones).

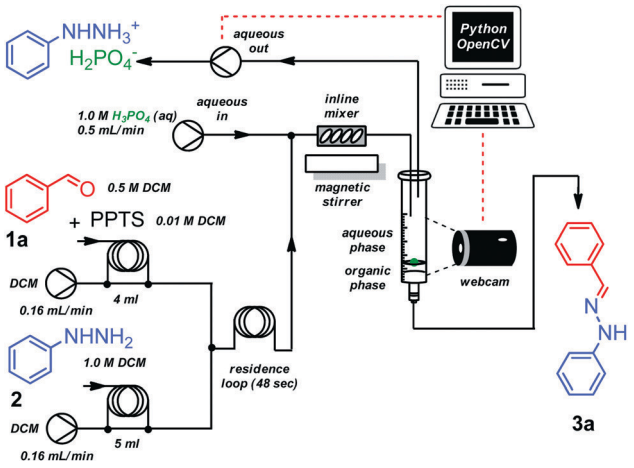


Figure 6.1 – Schematic of a flow reactor developed by O'Brien *et al.* for the synthesis of hydrazones, incorporating a gravity-based liquid-liquid separator. Streams of benzaldeyhde **1a** and phenylhydrazine **2** in dichloromethane were combined to form the hydrazone **3a**, using pyridinium toluenesulfonate as a catalyst. The organic product stream was combined with aqueous phosphoric acid to extract excess **2**, and the combined fluid stream was passed through an inline mixer to maximise mass transfer between the phases, before entering the liquid–liquid separator. Reproduced from Ref. 96 with permission from The Royal Society of Chemistry.

The separator was used after the extraction of excess reagent from the organic phase (containing the product) into water. A biphasic flow was pumped into a vertically-mounted plastic syringe barrel (2.5 mL volume) where the two liquids separated under gravity. The heavy organic phase exited through the outlet at the bottom of the syringe and the light aqueous phase was pumped from the syringe via a tube inserted into the barrel. A small ball of green plastic (chosen to have a density in-between that of the two phases) was added to the syringe barrel so that the location of the interface could be easily detected by a digital camera (plus machine vision software). The interface location was kept constant using a proportional control algorithm to adjust the flow rate of the pump used to withdraw the waste-containing light phase. The volume of the product-containing heavy phase in the separator was maintained at around 0.25 mL.

A potential drawback of this design is that the flow through the bottom

outlet is uncontrolled. In order to slow the flow of the dense phase through the outlet, preventing it from flowing straight through, the end of the tubing attached to the outlet was raised above the separator. Connecting the outlet tube to another process would be problematic without further pumping equipment due to insufficient hydraulic pressure to overcome the fluidic resistance downstream. The pressure is provided entirely by the weight of liquid accumulated in the separator. Working in the same research group, Hu *et al.* addressed this limitation by replacing the syringe barrel with a 3 mm diameter glass column and incorporating a metering pump for the phase to be processed further.[97] The separator could be operated in one of two configurations, with either the heavy or light phase being made available for further processing. Rather than pumping the unwanted phase from the column (as with the previous design), Hu *et al.* instead collected the phase required for further processing. This way they could pass the phase on to another processing step at a controlled flow rate and pressure. To demonstrate this development, they produced α-hydroxyacids by the diazotization of amino acids in water and extracted them into ethyl acetate. Around 74% of the α-hydroxyacid is extracted from the water into ethyl acetate after each extraction, so multiple extractions are required to recover all the product efficiently. To achieve this in flow three liquid-liquid separators were connected in series, adding fresh ethyl acetate at each stage and passing the metered aqueous stream on to the next separator (Figure 6.2). A similar design of separator was also used by Bourne *et al.* to acid-wash the product of a Pd-catalysed vinylation of aryl halides, enabling a subsequent Rh-catalysed hydroformylation.[98]

6.2.2 Wetting-based separators

Using binary material pairs

Whilst the separator developed by Hu *et al.* had a relatively low (0.5 mL) volume compared to most gravity separators, the volume is still quite large for microscale applications where the microreactor itself has a smaller volume. Furthermore, a pump is required to achieve separation, adding cost and

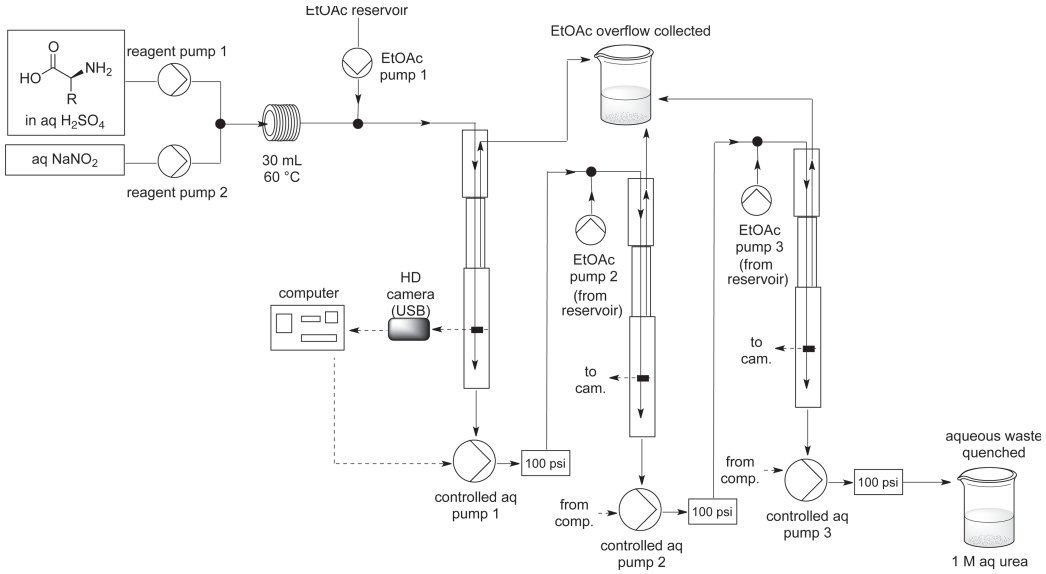


Figure 6.2 – Schematic showing an improved gravity-based liquid-liquid separator developed by Hu *et al.* for the continuous aqueous diazotization of amino acids and subsequent sequential liquid–liquid extraction of the α-hydroxyacid product into ethyl acetate. Reproduced with permission from Ref. 97. Copyright 2012 American Chemical Society.

complexity to the setup. For microscale applications involving small quantities of solvent, wetting-based methods are preferable since phase separation is induced by interfacial rather than gravitational forces. Wetting-based separators consist of a pair of hydrophobic and hydrophilic surfaces. The two phases wet the surfaces differently and this difference is used to achieve phase separation. The larger the difference in the wetting of the phases, the easier it is to induce and maintain phase separation.

One of the first examples of this approach was developed by Kashid *et al.*, who developed a wetting-based separator based around a Y-shaped junction machined from teflon.[99] A steel needle was inserted into one of the outlet channels of the Y-shaped junction, with the aqueous phase preferentially wetting the steel needle, and the organic phase preferentially wetting the teflon (see Figure 6.3). This caused the incoming biphasic flow to separate into a pure stream of the aqueous phase at the steel outlet and a pure stream of organic phase at the teflon outlet. Kashid *et al.* tested their separator with

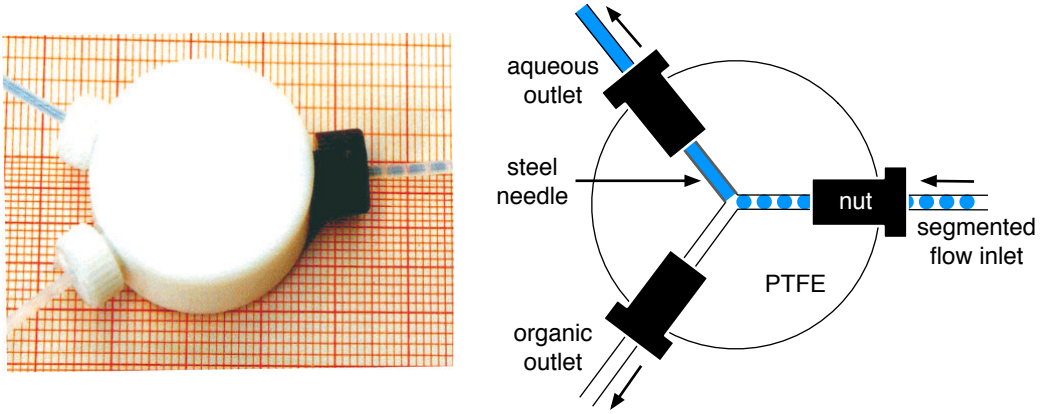


Figure 6.3 – **Left:** photograph of a wetting-based separator developed by Kashid *et al.* in which the aqueous phase has been dyed blue and the organic phase is colourless. Reproduced with permission from Ref. 99. Copyright 2007 American Chemical Society. **Right:** schematic drawn from experimental details provided in Ref. 99. The devices consists of a Y-junction made from teflon. A segmented flow enters the inlet on the right. Upon reaching the centre of the junction, the aqueous phase wets the steel needle inserted in one of the outlet channels and exits through it. The organic phase preferentially wets the teflon body and exits through the other channel. Tubing is attached using standard fluidic nuts.

water–kerosene and water–*n*-butanol segmented flows, using equal flow rates of each phase at total flow rates in the range of 5 to 60 mL/h. They also tested the performance of the separator with unbalanced flows, keeping one phase at 10 mL/h and varying the other between 5 to 60 mL/h. They found that whilst the organic phase always contaminated the aqueous outlet, the organic outlet remained pure and was never contaminated by water. Depending on the flow rate ratio of the organic to aqueous phases, water contaminated the organic phase 5 to 40 % by volume.

Kolehmainen *et al.* developed a plate-type phase separator consisting of a hydrophillic stainless steel plate and a hydrophobic PTFE plate sandwiched together (Figure 6.4).[100] They cut a shallow channel (15 mm wide, 200 mm long, and 100 µm or 200 µm deep) into the inside face of one of the plates and drilled an inlet for the biphasic flow on one plate and an outlet at the other end of each plate. They successfully separated segmented flows of water

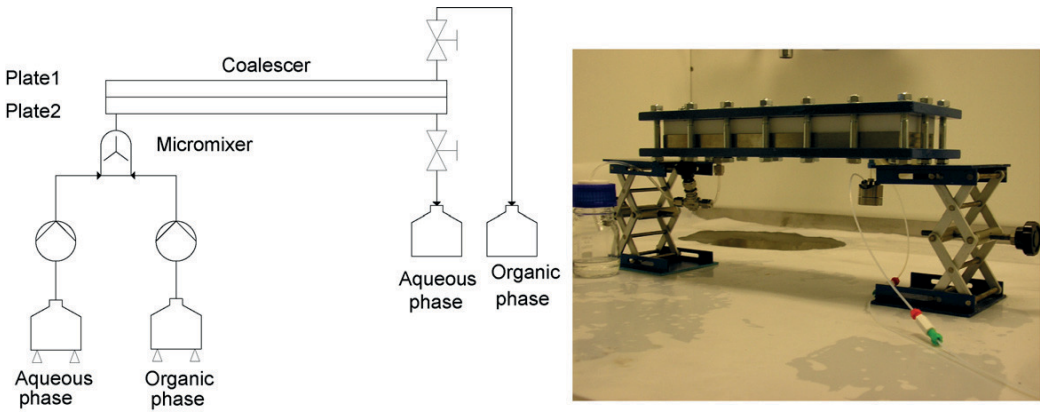


Figure 6.4 – Left: schematic of a plate-type separator developed by Kolehmainen *et al.* The aqueous and organic phases are pumped into a micromixer and then into the inlet of a coalescer made from a PTFE plate (plate 1) and a stainless steel plate (plate 2) containing a channel. The droplets coalesce, preferentially wet the stainless steel, and form a bilayer flowing through the device. The separated flows exit through back pressure regulators and are collected into separate bottles. **Right:** photograph of the separator. Reprinted from Ref. 100 with permission from Elsevier.

and Shellsol D60 (a commercially-available blend of paraffins and napthenes) mixed with tris(2-ethylhexyl)phosphate (a compound used in metal extraction) at total flow rates from 20 to 480 mL/h (1:1 ratio of each phase). The water droplets coalesced within the channel, causing the segmented flow to form a bilayer, in which the aqueous and organic layers wetted the stainless steel and PTFE respectively. Back pressure regulation was necessary on both outlets to prevent both phases exiting through the bottom outlet (due to gravity). Separation with less than 5% contamination by mass was obtained when the channel height was smaller than the diameter of the organic droplet, otherwise the droplets would not coalesce; at high flow rates the droplet diameter decreased, requiring the use of a shallower channel.

Scheiff *et al.* separated water–kerosene and water–mineral oil streams using a stainless steel needle inserted into a high-density polyethylene channel, creating what they called a "hydrophilic side-stream" (Figure 6.5).[101] As water slugs reached the needle, they wetted and flowed into it, separating the water from the organic phase. They found that the separation efficiency was

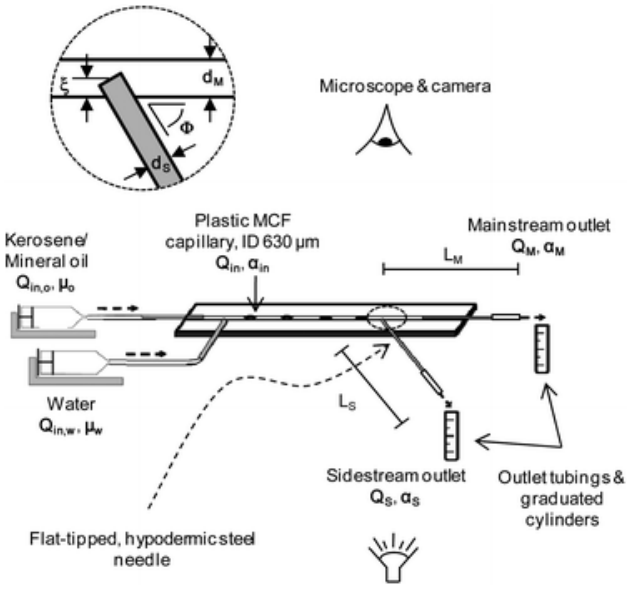


Figure 6.5 – Schematic of a phase separator developed by Scheiff *et al.* The aqueous and organic phases are pumped into a T-junction to generate a segmented flow inside a high-density polyethylene channel (ID $d_m = 0.63\,\text{mm}$). A steel needle (ID $d_s = 0.82\,\text{mm}$ or $0.51\,\text{mm}$) is inserted downstream (degree of penetration ζ and angle Φ; see inset) to create a hydrophilic sidestream. The aqueous phase wets and enters the sidestream, passing through an outlet channel (length L_s) to a graduated cylinder. The remaining organic phase exits through the mainstream outlet (length L_m) to a second graduated cylinder. Reproduced from Ref. 101 with permission of The Royal Society of Chemistry.

insensitive to the angle of the needle and its degree of penetration into the channel. Complete separation (with each phase at $10\,\text{mL/h}$) was achieved by varying the length of the tubing attached to the outlets in order to control ratio of the pressure drops for the aqueous side- and organic main-stream.

Using differences in capillary pressure

The selective wetting of a biphasic flow on a pair of hydrophobic and hydrophilic surfaces can also be used to achieve separation using one or more narrow channels. For a liquid to enter a cylindrical channel the applied pressure must exceed the *capillary pressure* ΔP_c, which is given by the Young-Laplace equation:

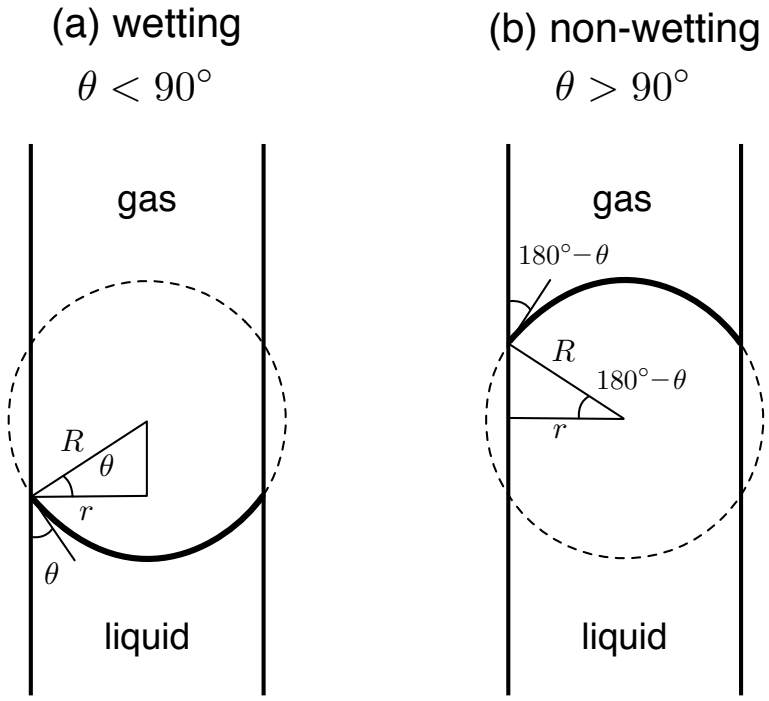


Figure 6.6 – Diagram of the liquid-gas (air) interface for (a) a wetting and (b) a non-wetting liquid in a cylindrical capillary channel of radius r. The contact angle θ is the angle (measured through the liquid) where the liquid-gas interface meets the channel wall. For (a) wetting and (b) non-wetting liquids, $\theta < 90°$ and $\theta > 90°$, respectively. The meniscus has a radius of curvature R.

$$\Delta P_c = \frac{2\gamma_{lg}}{R} \tag{6.1}$$

where γ_{lg} is the interfacial tension of the liquid-gas (air) interface and R is the radius of the curvature of the meniscus. Figure 6.6 shows the interface in a capillary for a (a) wetting and (b) non-wetting liquid, which have a contact angle $\theta < 90°$ and $\theta > 90°$, respectively.

First, consider the wetting liquid shown in Figure 6.6 (a). Equation 6.1 can be written in terms of the channel radius r and θ:

$$\Delta P_c^w = \frac{2\gamma_{lg}\cos\theta}{r} \tag{6.2}$$

Young's equation states that the interfacial tension of all three interfaces are

related such that:

$$\gamma_{lg} = \frac{\gamma_{gs} - \gamma_{sl}}{\cos\theta} \tag{6.3}$$

where γ_{gs} and γ_{sl} are the interfacial tension of the gas-solid and solid-liquid interface, respectively. Combining Equations 6.2 and 6.3 yields:

$$\Delta P_c^w = \frac{2(\gamma_{gs} - \gamma_{sl}^w)}{r} \tag{6.4}$$

from which it is clear that, since γ_{gs} is an intrinsic property of the channel material and r is constant for a cylindrical channel, ΔP_c is only a function of γ_{sl}.

Next, consider the non-wetting case shown in Figure 6.6 (b). Expressing Equation 6.1 in terms of r and θ:

$$\Delta P_c^{nw} = \frac{-2\gamma_{lg}\cos\theta}{r} \tag{6.5}$$

and again using Young's equation (Equation 6.3) gives:

$$\Delta P_c^{nw} = \frac{2(\gamma_{gs} + \gamma_{sl}^w)}{r} \tag{6.6}$$

By comparison of the capillary pressure for the wetting and non-wetting liquids (Equations 6.4 and 6.6) and noting that $\gamma > 0$, it is evident that $\Delta P_c^{nw} > \Delta P_c^w$. Therefore a non-wetting liquid requires a larger hydraulic pressure to enter a channel than a wetting liquid. Capillary force-based separators use this difference in ΔP_c to separate a biphasic flow by allowing the wetting phase to flow through a narrow channel, whilst preventing the non-wetting phase from entering.

Gaakeer *et al.* designed a separator using two adjustable slits, one made from hydrophilic glass and the other made from hydrophobic PTFE (Figure 6.7).[102] They separated water–*n*-heptane flows by adjusting the slit heights (in the range of 0.1 ± 0.2 to 2.0 ± 0.2 mm), thus changing the capillary pressure. The water and *n*-heptane exited through the glass and PTFE slits, respectively. The adjustable height of the slits allowed the same device to be used for a wide range of flow rates. For example, at high flow rates (and

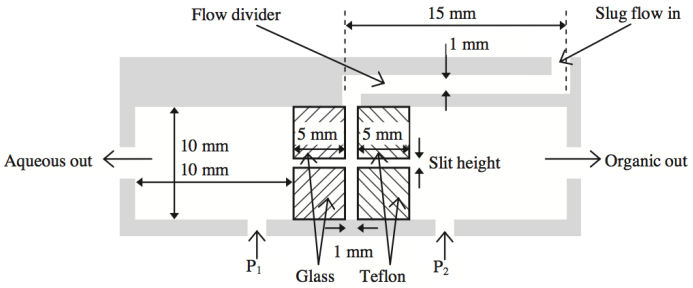


Figure 6.7 – Cross-sectional view of the slit-based separator developed by Gaakeer *et al.* The slug flow enters at the top of the device and flows through to two adjustable slits, one made of glass and the other teflon. The aqueous and organic phases selectively pass through the glass and teflon slits respectively. Reprinted from Ref. 102 with permission from Elsevier.

hence high hydraulic pressures), they found that water could break through the PTFE slit and contaminate the organic outlet because the pressure drop of the glass outlet exceeded the capillary pressure of the water through the PTFE slit. By widening the slit size from 0.1 ± 0.2 to 0.8 ± 0.2 mm they could reduce the pressure drop below the capillary pressure and achieve full separation. With the appropriate slit size, the device worked at 1:1 ratios with total flow rates of 10 to 50 mL/min and also 5:1 and 1:5 ratios at total flow rates of 15 to 35 mL/min.

Castell *et al.* designed a PTFE microfluidic chip for the separation of water–chloroform segmented flows.[103] They used laser ablation to cut an array of 140 narrow channels (36 µm wide, 130 µm deep, 5 mm long, and spaced 64 µm apart) perpendicular to the main channel containing the biphasic flow (Figure 6.8). The organic outlet was collected into a vessel at atmospheric pressure whereas the the aqueous outlet was collected into a sealed, pressure-controlled vessel. The chloroform wetted the PTFE chip material, resulting in a low ΔP_c compared to the non-wetting aqueous phase. Therefore the chloroform was able to easily enter the separator ducts, unlike the water. By controlling the pressure of the aqueous outlet collection vessel, they could obtain the exclusive passage of the organic phase through the separator ducts and achieve complete separation. The device was tested at relatively low

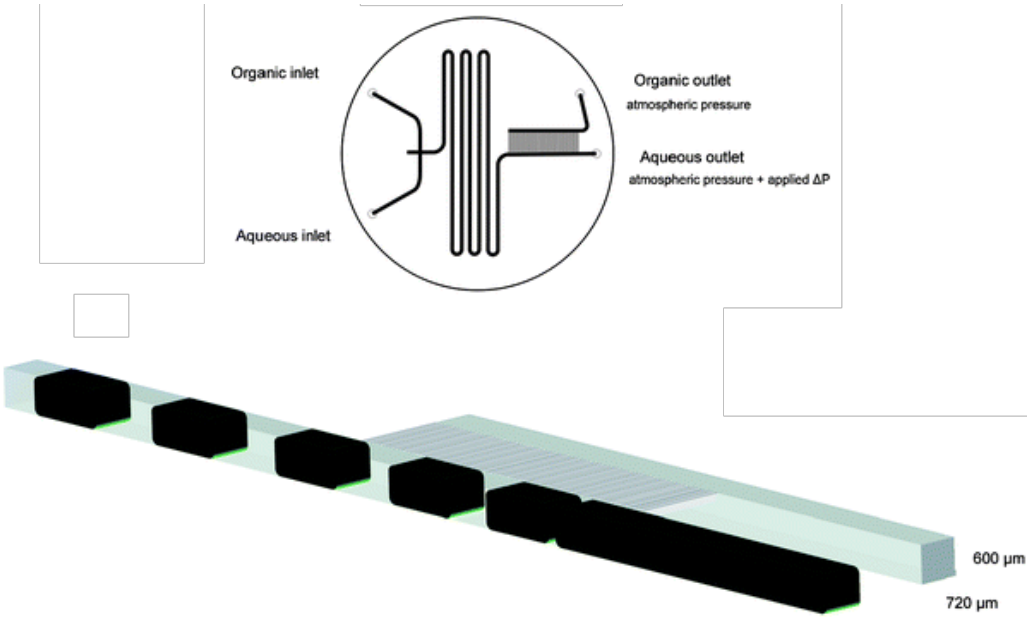


Figure 6.8 – **Top:** schematic of the microfluidic chip channel layout of the separator developed by Castell *et al.* **Bottom:** cartoon illustration of the separator in operation, showing the organic wetting phase (light) and aqueous non-wetting phase (dark). The segmented flow reaches the ducts, where the wetting organic phase enters and flows through to a separate outlet, leaving the aqueous phase flowing in the main channel. Adapted from Ref. 103 with permission of The Royal Society of Chemistry.

total flow rates of 60 to 360 µL/min (1:1 ratio of water:chloroform).

Using porous membranes

Capillary force separators can also be implemented using porous membranes, where the pores play an equivalent role to the narrow engineered channels previously mentioned. In 1970 Nord and Karlberg reported a membrane-based device for the separation of organic–aqueous segmented flows. They sandwiched a variety of different membranes between two pieces of perspex or teflon, each containing a groove facing the membrane (Figure 6.9). The most efficient separation was achieved using a PTFE membrane (0.5 or 1 µm pore size) with polyethylene backing. An organic–aqueous segmented flow was pumped into an inlet channel where it was brought into contact with the

membrane. The organic phase wetted and passed through the membrane, depleting up to 95 % of the organic phase from the segmented flow, and exited through a separate organic outlet channel. The remaining 5 % passed out of the device with the aqueous phase. The dimensions of the inlet groove containing the slug flow proved to be important. They found that the groove volume must be at least four to five times larger than the volume of a single water slug otherwise the hydraulic pressure would force water through the membrane and out the organic outlet. Furthermore, the orientation of the device was important. The device was mounted so that the outlet of the heavy phase was below the light phase. This indicates separation was not purely driven by the difference in surface wetting and capillary pressure of the two phases, but also their densities. (Mendorf *et al.* reported a similar requirement in their surface-wetting-based separator.[104]) This effect can be eliminated by reducing the channel dimensions in order to increase the importance of surface tension effects and reduce the effect of gravity.[b]

Like the device developed by Nord and Karlberg, Atallah *et al.* in 1987 constructed a separator by cutting a 10 cm long teflon rod (3 cm diameter) in half along its length.[106] The exposed surfaces were smoothed and a groove was cut into each face (50 mm long, 3 mm wide, and 1.5 mm deep). 2 holes, spaced 5 cm apart, were drilled on one half and a single hole on the other half for the segmented flow inlet and outlets of the separated phases. A membrane was sandwiched between the semi-cylinders and clamped together with hose clamps. They tested teflon plumbing tape, Gore-Tex (0.2 µm), and polypropylene-packed Gore-Tex (0.5 µm).[c] The segmented flow entered the device and the organic phase passed through the membrane and to the outlet on the other half of the device. The aqueous phase did not permeate

[b]The degree to which a system is affected by surface tension can be quantified by the Eötvös number $\mathrm{Eo} = \Delta P g L^2/\gamma$, where ΔP is the difference in density of the two phases, g is acceleration due to gravity, L is the characteristic length, and γ is the interfacial tension between the two phases. A large value for Eo indicates that interfacial forces dominate.

[c]Gore-Tex is a proprietary fabric membrane with a porous microstructure. In 1969 Robert W. Gore serendipitously discovered it by heating PTFE rods to approximately 300 °C, then quickly stretching them with a hard pull, rather than stretching them slowly. The PTFE stretched about 800 %, forming a porous microstructure that is about 70 % air.[107]

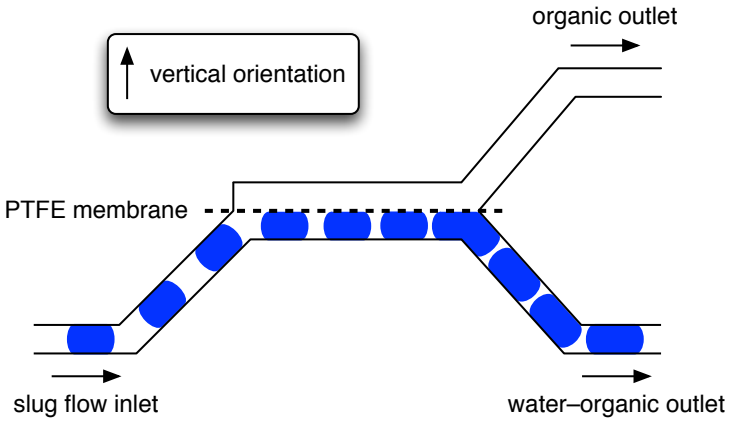


Figure 6.9 – Schematic of the membrane separator developed by Nord and Karlberg. An aqueous–organic flow is pumped into the inlet and brought into contact with a PTFE membrane. The organic phase selectively wets and permeates the membrane (up to 95 % by volume) and exits through the upper outlet. The remaining segmented flow exits through the lower outlet. Here the organic phase (colourless) is denser than the aqueous phase (blue), so the separator is orientated with the organic outlet above the aqueous outlet. Schematic drawn from details in Ref. 105.

the membrane and flowed out through the outlet on the same half as the inlet. Separating aqueous–chloroform segmented flows, the plumbing tape and Gore-Tex membrane worked for >10 h with no obvious performance differences observed between the two. However, at flow rates greater than 8 mL/min, those membranes ruptured, requiring the use of the more robust and larger pore size polypropylene-packed Gore-Tex membrane. For effective separation sufficient hydrodynamic pressure needed to be applied to the segmented flow for the organic phase to overcome the capillary pressure and pass through the membrane. Atallah ensured this was the case by connecting a flow restriction—a knotted 1 m length of 0.5 mm ID tubing—to the aqueous outlet.

More recently, Snead and Jamison described a similar device as part of a set-up for the continuous flow synthesis and purification of diphenhydramine hydrochloride (an active pharmaceutical ingredient for alleviating symptoms of the common cold), sandwiching a PTFE membrane (1 µm pore size) between two stainless steel plates to separate water–hexane flows.[108] Similarly,

Maurya *et al.* sandwiched a PTFE membrane (0.45 µm pore size) between two sheets of polyimide, into which they had cut (using laser ablation) microchannels.[109] In both reports, effective separation was obtained by adjusting the length of the tubing coupled to the outlets.

Kralj *et al.* developed two membrane-based separators.[110] The first was a proof of principle device in which a PTFE membrane (pore sizes in the 0.1 to 1.0 µm range) was sandwiched between two pieces of polycarbonate (Figure 6.10, top row). The second was a fully integrated silicon microfluidic chip for a reaction in continuous flow, followed by liquid–liquid extraction and phase separation (bottom row). Complete separation was obtained at flow rates of organic and aqueous solutions between 10 and 2000 µL/min. They were able to separate aqueous–organic (hexane) and aqueous–fluorous (perfluorohexane) flows, but they could not find a membrane material suitable for separating organic–fluorous flows. Materials studied included PTFE, cellulose, and ethyl acetate.

Sahoo *et al.* used the same devices to perform a multistep microfluidic synthesis of carbamates. They used the silicon microreactor for a phase-transfer reaction and separation, and the polycarbonate device for a gas–liquid separation.[24] Li *et al.* used the polycarbonate device in a flow reactor for the continuous hydroxylation of aryl halides with a catalyst-recycling loop.[111] An organic–aqueous segmented flow was used to extract the water-soluble product from the organic reaction solvent, leaving the costly Pd catalyst in the organic phase for further reactions.

Adamo *et al.* reported a second generation design that incorporated a pressure control section after the membrane to ensure reliable separation over a wider range of flow rates and back pressures.[112] The section consisted of a diaphragm stretched over the aqueous outlet stream with organic outlet flowing on the reverse side, and thus maintained a higher pressure on the aqueous side of the membrane than on the organic side. It worked at flow rates between 2 to 8 mL (1:1 ratio of hexane–water or ethyl acetate–water). They did not report separation of aqueous–fluorous or organic–fluorous phases.

Adamo's device is commercially available from Zaiput Flow Technologies.[113] Another separator is available from Syrris Ltd, called the Asia FLLEX

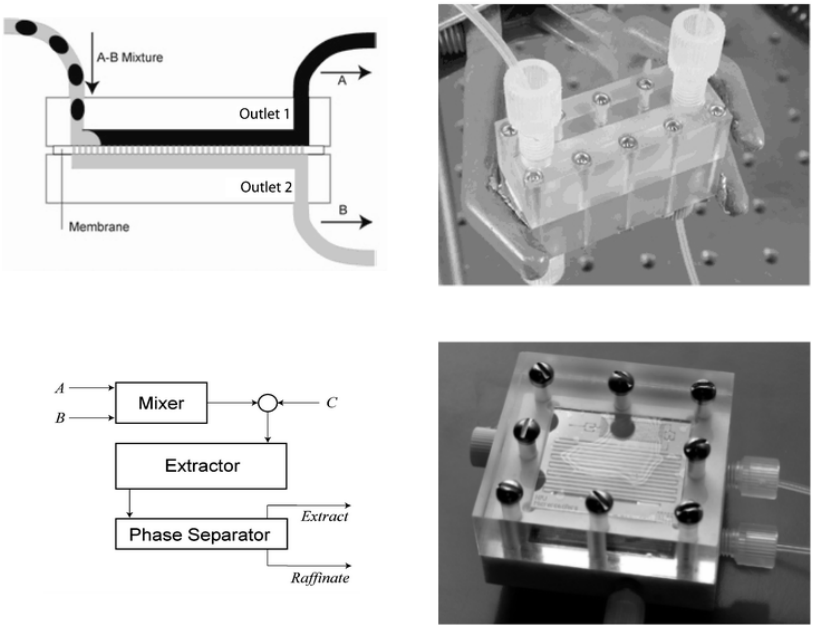


Figure 6.10 – **Top row:** schematic (left) and photograph (right) of the standalone separator developed by Kralj *et al.* A flat membrane is sandwiched between two pieces of machined polycarbonate. **Bottom row:** schematic (left) and photograph (right) of their intergrated silicon microfluidic device. The chip consists of two inlets **A** and **B**, a mixer, a third inlet **C** for an immiscible phase, an extractor consisting of winding serpentine channels for mass transfer between the phases, and lastly the separator. Adapted from Ref. 110 with permission of The Royal Society of Chemistry.

(flow liquid–liquid extraction), which uses a membrane for aqueous–organic separation over a relatively limited flow rate range of 250 to 500 µL/min.[114] Little information regarding its operation is available, but it most likely operates is the same manner as other membrane separators.

6.3 Development of a versatile liquid–liquid separator

There is a continuing need for versatile separation techniques that can work reliably with multiple liquid–liquid combinations—especially organic–fluorous flows—across a broad range of flow rates. In particular there is a need for simple methods that can be readily integrated with both chip- and capillary-based microfluidic systems without the need for extra equipment. In conjunction with my colleague, James Bannock, we reported in 2012 an effective method for inline separation of immiscible liquids using commercially sourced porous PTFE capillaries.[115] Using water dispersed in a fluorous oil as a test system, quantitative recovery of the water from the oil was achieved over a wide range of flow conditions. The was no contamination of the water by the fluorous component even when the latter was present in large (ten-fold) excess. The exiting water stream could be readily re-dispersed by injecting additional oil downstream, allowing for repeated switching between the segmented and continuous flow regimes—a key requirement for multistep chemical processing.

The use of porous capillaries for phase separation has some precedence in mass and atomic emission spectroscopy. In 1988 Barnes and Wang used Gore-Tex tubing (2.0 µm or 3.5 µm pore size) for gas–liquid separation in Inductively Coupled Plasma Atomic Emission Spectroscopy (ICP-AES)[116] and later Inductively Coupled Plasma Mass Spectrometry (ICP-MS).[117] Yamamoto *et al.* reported a similar device in 1988 for aqueous–organic extraction and separation, also for use in ICP-AES, shown in Figure 6.11.[118] They found that if they maintained the aqueous flow rate at 6.2 mL/min, separation could be achieved for organic flow rates in the range 0.2 to 6.2 mL/min.

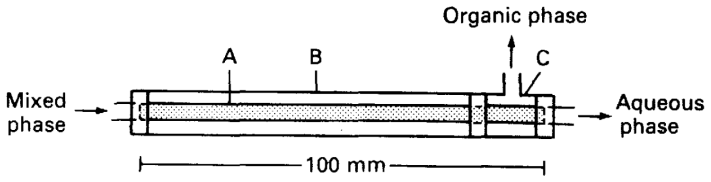


Figure 6.11 – Drawing of the phase separator developed by Yamamoto *et al.* It consists of an inner microporous Gore-Tex tube **A** (1 mm ID, 2 mm OD, and 3.5 µm pore size), outer solid PTFE tube **B**, and glass T-piece **C**. Reproduced from Ref. 118 with permission of The Royal Society of Chemistry.

However, there are very few reports of their use outside these fields and, prior to our previous report, porous capillaries had not been integrated with microfluidic componentry.

In the aforementioned publication, we applied porous PTFE capillaries to the separation of aqueous–fluorous fluid streams. It is the purpose of this chapter to demonstrate their wider applicability to aqueous–organic and organic–fluorous segmented flows. The separation of organic–fluorous fluid streams is of particular interest because the favourable properties of fluorous liquids (high boiling points, good chemical stability, and immiscibility with most organic solvents) has led to their use as carrier liquids in a variety of flow syntheses.[35,89,119] To my knowledge there have been no previous reports describing the successful inline separation of organic–fluorous mixtures, with Kralj *et al.* explicitly noting the difficulty of doing so due to the small difference in interfacial tension.[110] I also describe here a straightforward method for tuning the porous capillary separators to provide efficient liquid–liquid separation over a broad range of flow rates, and further present a simple demonstration of their application to the inline extraction of an analyte from an aqueous phase to an organic phase.

6.4 Results and Discussion

6.4.1 Operating principle

For convenience I refer to the two liquids in the segmented flow as the solvent and the carrier. The carrier is the phase that preferentially wets the walls of the separator. The solvent is typically understood to contain the reagents, products or analytes of interest, with the carrier acting merely as an inert liquid whose sole purpose is to maintain the segmented flow. However, this is not always so and in many cases—e.g. biphasic reactions or liquid–liquid extractions—both phases participate in the chemical procedure.

The principle of the separator is straightforward (Figure 6.12). The two-phase stream enters the inlet of the porous capillary. The carrier liquid preferentially wets and subsequently permeates the porous wall. The incoming flow pushes the carrier liquid through the porous wall, causing it to accumulate on the exterior until it is of sufficient weight to drip from the capillary into a collection vial. This process repeats, with new carrier liquid collecting on the exterior of the porous capillary until the next drip occurs, thereby allowing carrier liquid to be extracted indefinitely from the channel without any drop in separation efficiency. A continuous (single-phase) stream of solvent is left flowing through the porous tubing and emerges at the outlet. The outflowing solvent may then be transferred to a vial for collection or passed into the next stage of a multistep chemical process as required.

The separators are formed from short (6 cm) lengths of commercially sourced porous PTFE tubing of 1.8 mm ID and 2.5 mm OD. The porous PTFE has a stringy microstructure, with pores of up to a few microns in width and up to 30 µm in length, as can be seen from the scanning electron micrograph in Figure 6.13. In consequence porous PTFE has a soft rubbery consistency that prevents its direct connection to standard microfluidic fittings. To overcome this limitation short (6 cm) lengths of conventional rigid PTFE are inserted into each end of the porous tubing and fixed in place with a small amount of adhesive (see inset to Figure 6.14 and Section 6.6). By ensuring the adhesive is applied locally at the extremities of the porous

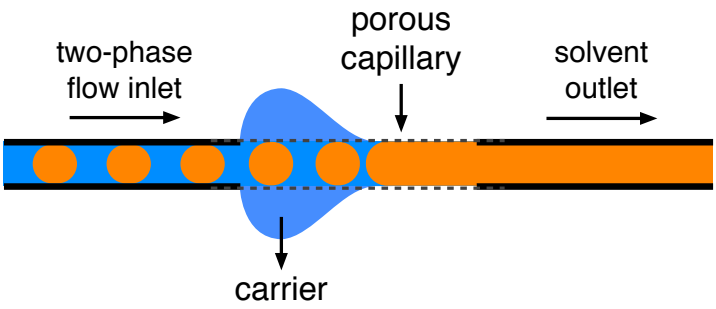


Figure 6.12 – Cartoon showing operation of the separator. A two-phase flow enters the inlet of the porous capillary. The carrier liquid (blue) preferentially wets and subsequently permeates the porous wall. The solvent (orange) is left flowing through the porous capillary and exits as a continuous stream at the outlet.

tubing, contact between the flowing liquids and the glue is avoided, allowing the bond to remain intact regardless of the choice of solvent or carrier liquid. With the rigid PTFE tubing in place, the separators can be readily attached to other chip- or capillary-based microreactors.

The separator relies on the difference in the capillary pressure of the carrier and solvent to induce and maintain separation (see Section 6.2.2). Treating the pores of the separator walls as cylinders (for simplicity), the Young-Laplace equation (Equation 6.7) can be used to calculate the capillary pressure ΔP_c that must be overcome for a liquid to penetrate a pore:

$$\Delta P_c = \frac{2\gamma_{lg}}{R} \tag{6.7}$$

where γ_{lg} is the interfacial tension of the liquid-gas (air) interface and R is the radius of curvature of the interface. For successful separation, the solvent (the non-wetting phase) must flow through the channel of the separator without penetrating the separator walls and so exit unhindered into the outlet channel. Hence, the pressure drop across the outlet channel ΔP_{outlet} must be lower than the capillary pressure for the solvent $\Delta P_c^{\text{solvent}}$:

$$\Delta P_{\text{outlet}} < \Delta P_c^{\text{solvent}} \tag{6.8}$$

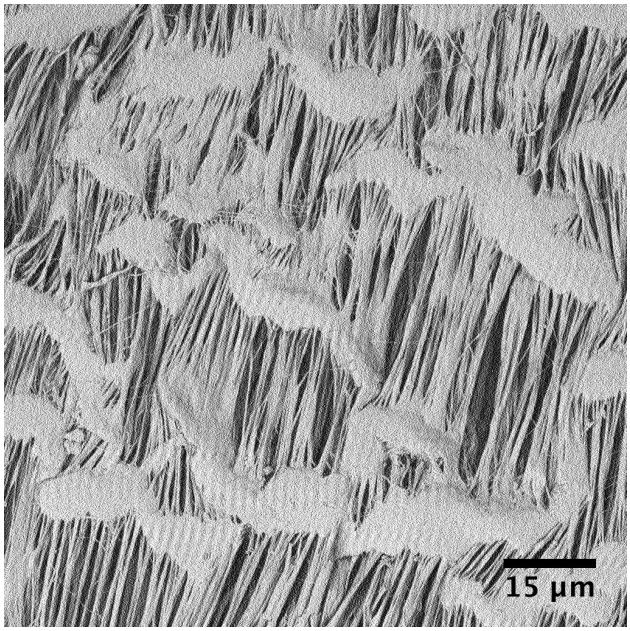


Figure 6.13 – SEM image of the porous PTFE capillary. The material has a stringy microstructure, with pores of up to a few microns in width and up to 30 µm long.

If this is not the case, a fraction of the solvent will be forced through the capillary walls, leading to its incomplete recovery at the outlet. At the same time the carrier (the wetting phase) must completely penetrate the walls so that none of it reaches the outlet channel. Hence ΔP_{outlet} must be greater than the capillary pressure for the carrier $\Delta P_c^{\text{carrier}}$:

$$\Delta P_{\text{outlet}} > \Delta P_c^{\text{carrier}} \tag{6.9}$$

If this is not the case, a fraction of the carrier will pass through the entire length of the porous tubing without being depleted through the walls, causing a mixture of carrier and solvent to emerge at the outlet. It follows that to achieve perfect phase separation ΔP_{outlet} must lie in the range:

$$\Delta P_c^{\text{solvent}} > \Delta P_{\text{outlet}} > \Delta P_c^{\text{carrier}} \tag{6.10}$$

Since $\Delta P_c^{\text{solvent}}$ and $\Delta P_c^{\text{carrier}}$ are determined by the intrinsic properties of the two liquids and the pore size distribution of the porous capillary (which

is hard to control and fixed for a given sample of tubing), perfect separation is most readily achieved by tuning ΔP_{outlet} until it satisfies the inequality in Equation 6.10.

When passing segmented flows of common laboratory solvents of low to moderate viscosity through the porous capillary, the outlet pressure is typically too low to achieve perfect separation, causing carrier liquid to leak through the outlet. The outlet pressure drop ΔP_{outlet} is related to the length l and diameter d of the outlet channel by the Hagen-Poiseuille equation:

$$\Delta P_{\text{outlet}} = \frac{128 \mu l Q}{\pi d^4} \tag{6.11}$$

where Q is the volumetric flow rate and μ is the dynamic viscosity of the liquid. Thus to bring ΔP_{outlet} into the required range it is necessary to increase the effective length and/or reduce the effective diameter of the separator, which can readily be achieved by coupling a narrow flow restriction to the outlet of the separator. Since the pore size distribution is poorly defined (see Figure 6.13), optimum dimensions of the flow restriction cannot be determined *ab initio* and must instead be found empirically (which as shown in the next section is a straightforward undertaking).

6.4.2 Inline liquid–liquid separation

Figure 6.14 shows the experimental set up used to study the behaviour of the porous capillary separator. A segmented flow was generated by separately pumping two immiscible liquids into the two inlets of a machined two-in-one-out PTFE junction (see Section 6.6). The outlet of the junction was in turn connected to the inlet of the separator. To increase the outlet pressure beyond that provided by the separator alone, pieces of narrow tubing of varying diameter and length were coupled to the end of the separator using standard fluidic fittings. The liquid emerging from the outlet of the separator (plus flow restriction) was collected into a vial sitting on a mass balance, while liquid emerging from the walls of the porous tubing was collected into a second vial. The volumetric collection rate of liquid at the outlet of the

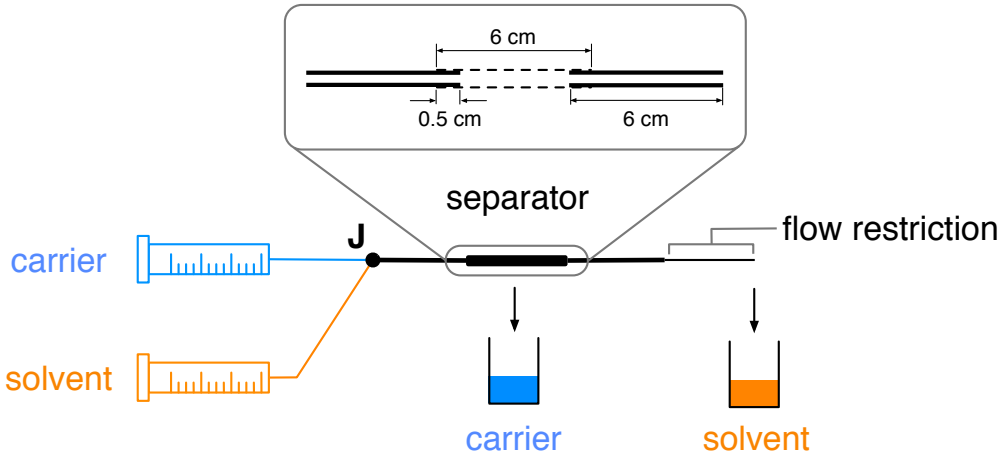


Figure 6.14 – Schematic of the separator in use. Carrier and solvent are pumped into a two-in-one-out junction **J** to generate a segmented flow, which is passed directly to the inlet of the separator. The outlet of the separator is coupled to a flow restriction of length l and ID d. Separated carrier and solvent are collected into vials through the porous walls of the PTFE capillary and the outlet of the flow restriction, respectively. The solvent vial is seated on a balance to allow calculation of the volumetric collection rate at the outlet (see Section 6.6).

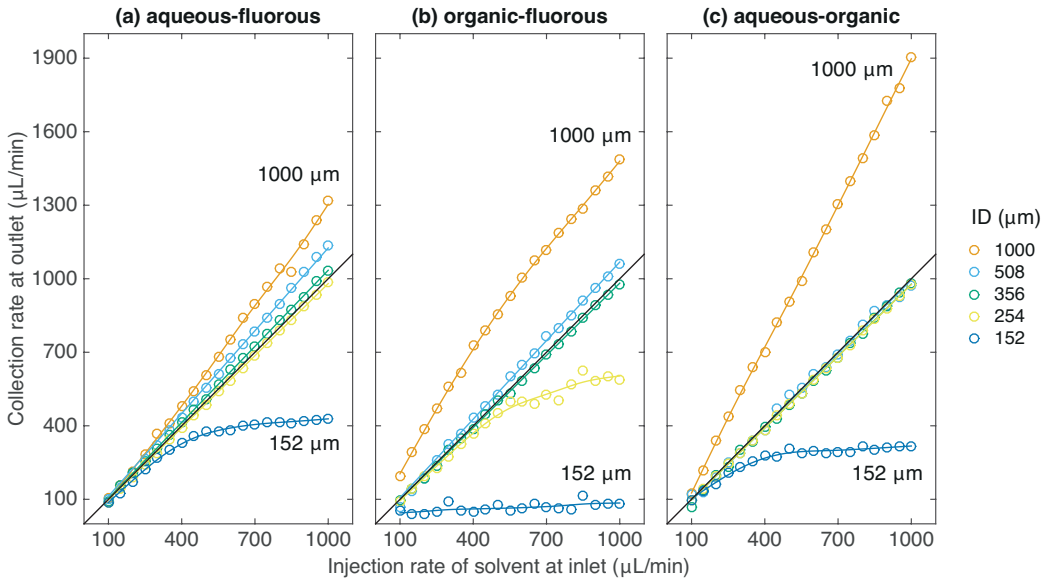


Figure 6.15 – Graphs showing the volumetric collection rate at the outlet versus volumetric injection rate of solvent at the inlet for (a) aqueous–fluorous, (b) organic–fluorous, and (c) aqueous–organic systems. Results are shown for flow restrictions of common length $l = 5\,\text{cm}$ and IDs ranging from 152 to 1000 µm. The black lines denote perfect separation in which the collection rate at the outlet is equal to the injection rate of solvent at the inlet. The maximum error in the volumetric collection rate at the outlet is $\pm 6\,\mu\text{L/min}$.

separator was determined using the procedure outlined in Section 6.6. For the measurements reported here the carrier and solvent were injected at equal volumetric flow rates—a common situation for two-phase systems—but the porous capillary has previously been found to provide efficient separation even when the carrier liquid is in large (ten-fold) excess.[115]

Figure 6.15 (a) shows for an aqueous–fluorous segmented flow the measured volumetric collection rate of liquid at the outlet versus the volumetric injection rate of solvent at the inlet, using various diameters d of flow restriction between 152 and 1000 µm (length $l = 5\,\text{cm}$ in all cases). The (non-experimental) black line denotes ideal behavior, i.e. 100 % separation efficiency, in which the collection rate of solvent at the outlet is equal to the injection rate of solvent at the inlet. Experimental separation curves that lie above this line correspond to incomplete depletion of the carrier liquid, caus-

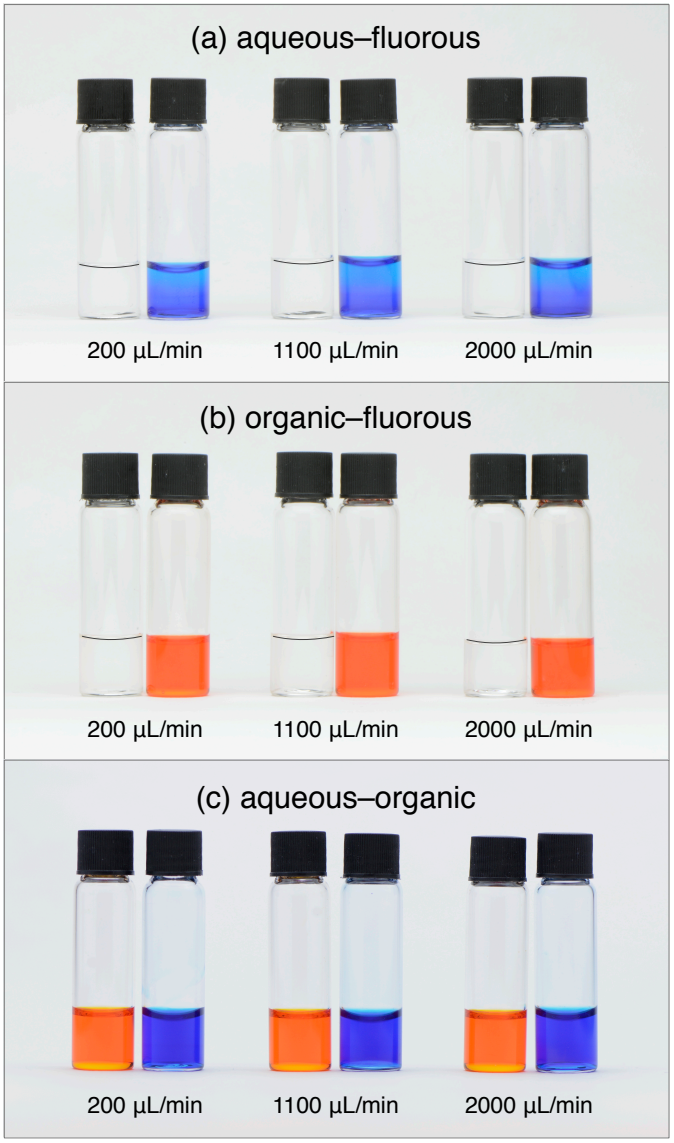


Figure 6.16 – Photographs showing vials containing liquid collected through the separator walls (left vial) and from the outlet of the separator (right vial) at total flow rates of 200 µL/min, 1100 µL/min, and 2000 µL/min for (a) aqueous–fluorous ($d = 254\,\mu m$), (b) organic–fluorous ($d = 356\,\mu m$), and (c) aqueous–organic ($d = 254\,\mu m$) liquid–liquid mixtures ($l = 5\,cm$ in all cases). Aqueous and organic phases were dyed blue and orange respectively. For clarity, lines have been drawn to indicate the menisci of the colourless fluorous phase. 1 mL of solvent and carrier liquid was collected in each case.

ing the volume of collected liquid to exceed the volume of injected solvent. Separation curves that lie below this line correspond to incomplete recovery of the solvent due to loss through the walls of the porous capillary.

The aqueous–fluorous separation curves obtained using the three widest flow restrictions all lay above the ideal line, indicating incomplete removal of the carrier liquid through the capillary walls. The slope of the curves decreased as the diameter was reduced from 1000 to 508 to 356 µm, consistent with the increasing pressure drop ΔP_{outlet} forcing more of the carrier liquid to deplete through the porous walls of the capillary. Visual inspection of the collection vials confirmed this to be the case: substantial contamination of the solvent by the carrier liquid was evident in the outlet vial in each case, with the amount of carrier liquid falling as the diameter of the flow restriction was reduced. (The other vial contained carrier liquid only, indicating no loss of solvent through the capillary walls).

Reducing the diameter of the flow restriction further to 254 µm yielded a straight-line response of slope $m = 0.980 \pm 0.004$, corresponding closely to the ideal line for perfect separation. Visual inspection of the two vials confirmed this to be the case, with no cross contamination evident in either vial for any of the flow rates tested, see Figure 6.16 (a). Reducing the diameter still further to 152 µm yielded a separation curve below the ideal line, indicating incomplete recovery of the solvent (as a result of its partial depletion through the porous walls of the capillary). Visual inspection of the two vials confirmed this to be the case: while the outlet vial contained only solvent, there was substantial contamination of the carrier liquid by the solvent in the other vial. (Note, although the separation under these conditions is imperfect, it could nonetheless be acceptable for some analytical applications where complete removal of the carrier liquid—as opposed to full recovery of the analyte—is the key requirement).

Figure 6.15 (b) shows equivalent curves for an organic–fluorous fluid stream. The same general behavior was observed as before, with the widest flow restrictions leading to separation curves that lay above the ideal line, and the narrowest flow restrictions leading to separation curves that lay below the ideal line. A 356 µm diameter flow restriction was found to yield

the optimum behavior with a slope $m = 0.982 \pm 0.005$, corresponding to near-perfect separation. For this choice of flow restriction, visual inspection confirmed the complete separation of the two liquids at each of the flow rates tested, with no cross contamination visible in either vial, see Figure 6.16 (b).

Figure 6.15 (c) shows equivalent curves for an aqueous–organic fluid stream. With the widest flow restriction of 1000 µm a linear response of slope $m = 1.86 \pm 0.03$ was obtained, consistent with over 75 % of the carrier exiting through the outlet. Flow restrictions of 508 µm, 356 µm, and 254 µm all yielded close to ideal behavior with slopes of $m = 1.00 \pm 0.01$, 0.978 ± 0.008, and 0.976 ± 0.003 respectively, signifying near-perfect separation in each case. Figure 6.16 (c) shows complete separation of the aqueous and organic phases, with no cross-contamination, for the case of a 254 µm diameter flow restriction. The narrowest 152 µm flow restriction yielded a sub-linear response due to significant depletion of water through the porous walls of the capillary.

It is evident from Figure 6.15 that near-perfect liquid–liquid separation can be achieved for aqueous–fluorous, organic–fluorous and aqueous–organic fluid streams by carefully tuning the diameter of the flow restriction. However, since the outlet pressure is inversely proportional to the fourth power of the diameter ($\Delta P_{\text{outlet}} \propto d^{-4}$, see Equation 6.11), varying the diameter of the flow restriction may sometimes provide an overly coarse means of controlling the outlet pressure drop. A better approach in these circumstances is to vary the length of the outlet channel, exploiting the linear relationship between ΔP_{outlet} and l. In this way, d and l can be used as coarse and fine controls over the separation efficiency, enabling the widest possible operating window to be achieved for the liquid–liquid system under study.

Figure 6.17 shows for an organic–fluorous segmented flow the volumetric collection rate at the outlet versus the volumetric injection rate of solvent at the inlet, using three different flow restrictions of common diameter $d =$ 254 µm and lengths $l = 2.5$ cm, 5 cm, and 10 cm. For $l = 10$ cm, the separation curve followed the ideal line up to solvent injection rates of approximately 300 µL/min, denoting near-perfect separation. At higher injection rates of solvent, however, the increasing outlet pressure (see Equation 6.11) caused

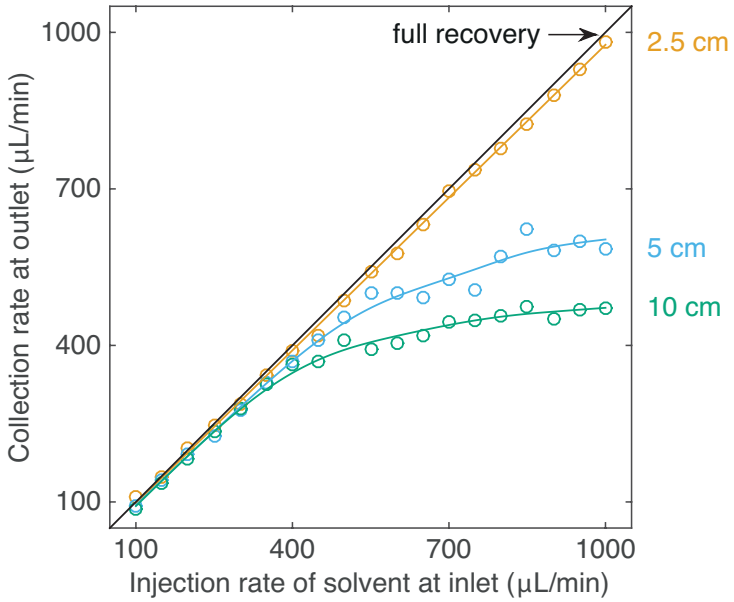


Figure 6.17 – Graph showing the volumetric collection rate at the outlet versus the volumetric injection rate of solvent at the inlet for organic–fluorous separation, using flow restrictions of common ID $d = 254\,\mu\text{m}$ and lengths of 2.5 cm, 5 cm, and 10 cm. The maximum error in the volumetric collection rate at the outlet is $\pm 4\,\mu\text{L/min}$.

the solvent to permeate the separator walls, causing the separation curve to fall below the ideal line. At the highest solvent injection rate of 1000 µL/min, less than half (47 %) of the solvent was recovered at the outlet.

Halving the length of the flow restriction to 5 cm brought the separation curve closer to the black line, with the reduced outlet pressure causing less solvent to permeate the separator walls. Shortening the outlet channel still further to $l = 2.5$ cm resulted in a linear separation curve ($m = 0.976 \pm 0.006$) close to the black line, indicating near-perfect separation over the range of injection rates tested. Hence, it is evident that l as well as d may be tuned to achieve complete separation of the two liquids.

6.4.3 Inline liquid–liquid extraction

To demonstrate the suitability of the separator for inline flow processing, we implemented a liquid–liquid extraction using the pH indicator 2,6-dichloroindophenol, referred to here as HA. Since HA is a weak acid ($pK_a = 5.9$[120]) it is neutrally charged, and readily dissolves in organic solvents to form orange-coloured solutions. When deprotonated with a strong base such as NaOH it forms the negatively-charged conjugate base A^-, rendering it soluble in water as a blue solution.

Figure 6.18 shows a schematic of the set-up for the aqueous–organic extraction. Aqueous solutions of conjugate base NaA (blue) and HCl (colourless) were pumped from separate syringe pumps at 10 µL/min each into a Y-mixer, producing HA (pink). To extract HA from the aqueous feed, a water–chloroform segmented flow was generated by connecting the outlet of the Y-mixer to one inlet of a two-in-one-out junction, while chloroform was pumped at 10 µL/min into the other inlet. Chloroform preferentially wetted the PTFE walls of the channel and so acted as the carrier phase. As the segmented flow passed along the 60 cm channel, the aqueous phase gradually changed from pink to colourless, while the chloroform changed from colourless to orange, indicating successful extraction of HA from water into chloroform. Finally, the aqueous–organic segmented flow was separated using a porous PTFE separator (with $d = 254$ µm, $l = 5$ cm flow restriction). The orange

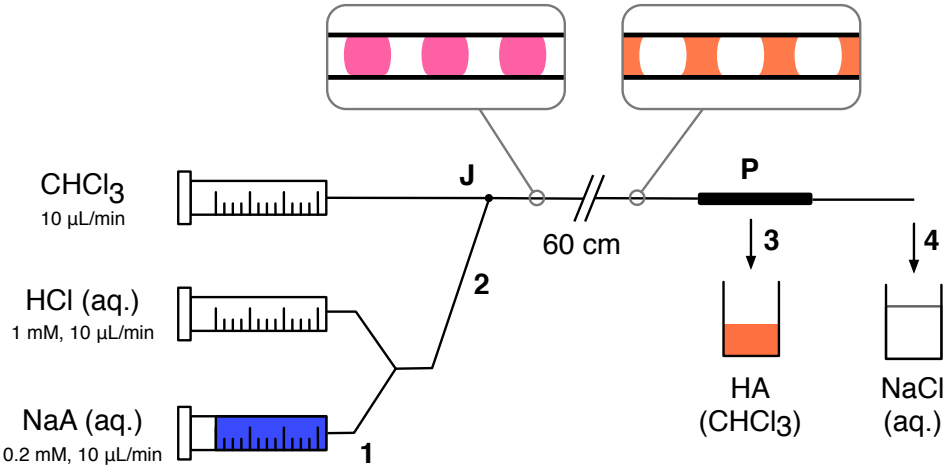


Figure 6.18 – Schematic of experimental set-up used for aqueous–organic extraction followed by inline separation. Aqueous solutions of 2,6-dichloroindophenol sodium salt (NaA, **1**) and HCl are pumped into a Y-mixer to produce 2,6-dichloroindophenol (HA, **2**). An aqueous–organic segmented flow is generated by the two-in-one-out junction **J**. HA is extracted from the aqueous phase into the organic phase in a 60 cm length of PTFE tubing. The two phases (**3** and **4**) are then separated using a porous capillary **P** (outlet channel $d = 254\,\mu\text{m}$ and $l = 5\,\text{cm}$) and collected into vials.

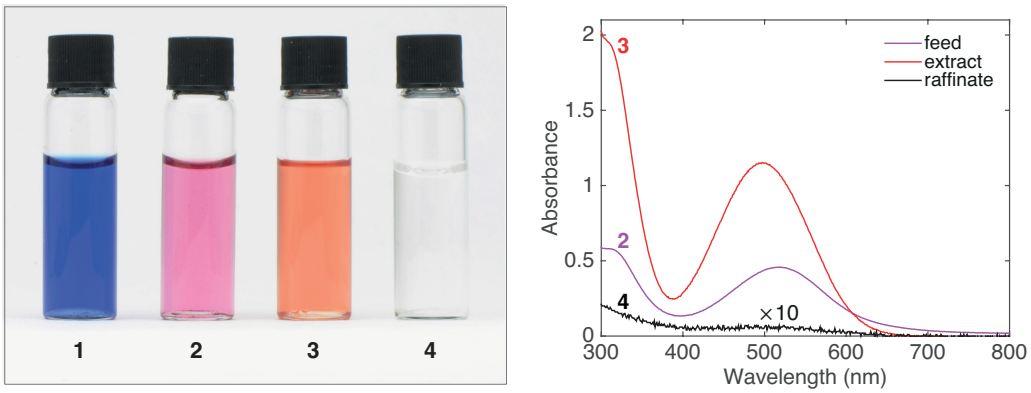


Figure 6.19 – **Left:** Photographs of NaA (aq.) (**1**), HA (aq.) (**2**), extract HA ($CHCl_3$) (**3**), and raffinate NaCl (aq.) (**4**) obtained using the set-up in Figure 6.18. **Right:** UV-visible absorption spectra of the feed (**2**), extract (**3**), and raffinate (**4**).

organic phase containing HA permeated the walls of the separator and was collected into a vial. The aqueous phase was collected from the outlet of the separator into a separate vial (colourless).

Figure 6.19 shows a photograph of the liquids at each stage of the process and the UV-visible absorption spectra of the aqueous feed **2**, the organic extract **3** and the aqueous raffinate **4**. Comparing the absorption spectra of the feed and the raffinate, it is evident that the aqueous phase has been virtually depleted of HA, while solution **3** now shows a strong absorption spectrum characteristic of HA in chloroform. Comparing the peak absorbances of solutions **2** and **4** at 519 nm (0.458 and 0.005 respectively), it is evident that there is an approximate 100-fold reduction in HA concentration after chloroform extraction.

6.5 Conclusions

In conclusion the work described in this chapter has demonstrated the use of a porous PTFE capillary for the inline separation of aqueous–fluorous, organic–fluorous, and aqueous–organic segmented flows. When a suitable back pressure is established (e.g. by adding a flow restriction of appropriate

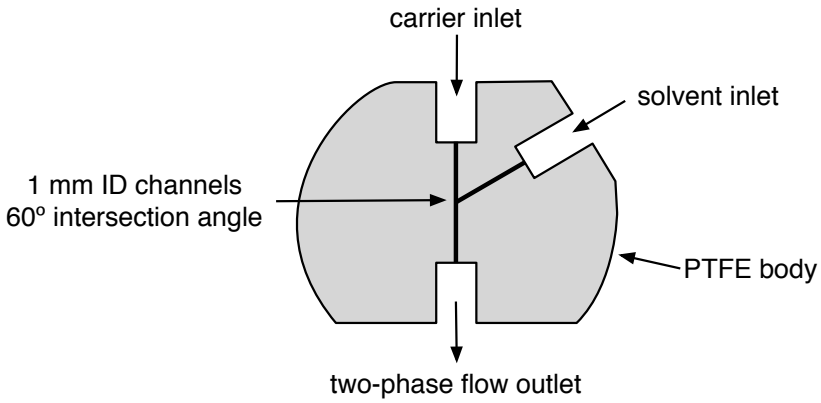


Figure 6.20 – Diagram of a two-in-one-out junction machined from PTFE round stock.

diameter and length), separation of the two phases can be reliably achieved over a wide range of flow rates.

As a practical demonstration of the utility of the separator a simple in-line aqueous–organic extraction was carried out using the pH indicator 2,6-dichloroindophenol. Extraction of the indicator from an aqueous solution into chloroform using a segmented flow, followed by liquid–liquid separation in a porous capillary, resulted in a continuous aqueous exit stream that had been almost completely depleted of indicator.

6.6 Experimental Methods

6.6.1 Two-in-one-out junction

A two-in-one-out junction was machined from PTFE round stock (RS Components) on a 4-axis computer numerical control (CNC) mill to the design in Ref. 46 and shown in Figure 6.20. A channel was drilled for the inlet of the carrier and the outlet of the two-phase flow. A second channel for the solvent inlet was drilled to create a junction of the two channels with an intersection angle of 60°. Holes were drilled and tapped (1/4”-28) to allow connection of tubing using Upchurch flangeless fittings.

6.6.2 Fabrication of separator

Loctite 770 primer was applied to the outer surface of the last 5 mm of two 6 cm lengths of non-porous PTFE tubing (Polyflon Technology Ltd, 1 mm ID, 2 mm OD). The primed ends were inserted 5 mm into each end of a 6 cm length of porous PTFE capillary (Aeos, Zeus Industrial Products, 1.8 mm ID, 2.5 mm OD, 15 to 25 µm internodal distance) to give a 5 cm length of exposed porous tubing. To secure the rigid PTFE in place, Loctite 406 adhesive was applied to the outside of the porous PTFE where the ends of the tubing overlapped.

6.6.3 Testing of separator

Toluene (>99.5 %, VWR) and Galden HT230 (Solvay Solexis) were used as the organic and fluorous phases respectively. Deionized water was obtained from a Millipore Direct-Q UV 3 system. Water and toluene were dyed with methylene blue and Sudan II, respectively (Sigma-Aldrich). Fluorinated ethylene propylene tubing (Upchurch) was used for the flow restrictions, with the exception of the 1000 µm ID flow restriction, which was PTFE. Unless specified otherwise, all other tubing was PTFE with 1 mm ID and 2 mm OD.

A Syrris Asia syringe pump was used to control the volumetric injection rates of the solvent and carrier liquid into the inlets of the two-in-one-out junction. The volumetric collection rate of liquid at the separator outlet was determined by collecting the liquid into a vial on a mass balance and recording the change in mass over a fixed period of time as described below.

The solvent and carrier liquid were pumped at equal volumetric flow rates to give a total flow rate (TFR) in the range 200 to 2000 µL/min. TFRs were tested in a randomized order. For each TFR, the liquids were infused for two minutes to allow the separator to reach steady state. The pumps were briefly stopped to record the mass of liquid m_i on the mass balance. The pumps were then restarted and run for a collection time Δt of four minutes, before stopping and again recording the mass m_f. The collected mass Δm of liquid over the four minute duration was determined from $\Delta m = m_f - m_i$.

In the case of perfect separation, pure solvent was collected at the outlet

and pure carrier liquid was collected through the walls of the separator. For imperfect separation, a mixture of the two liquids was only observed in one of the two vials: either a mixture of the two liquids was collected at the outlet, while pure carrier liquid was extracted through the walls of the separator; or pure solvent was collected at the outlet, while a mixture of the two liquids was collected through the walls of the separator. Liquid–liquid mixtures were never observed in the two collection vials simultaneously.

The injected mass Δm^* of solvent is given by $\Delta m^* = Q_{\text{in}} \rho_s \Delta t$ where Q_{in} and ρ_s are the volumetric injection rate and the density of the solvent respectively. For the case where pure solvent was collected at the outlet, $\Delta m \leq \Delta m^*$, and the volumetric collection rate of liquid was calculated as:

$$Q_{\text{out}} = \frac{\Delta m}{\rho_s \Delta t} \tag{6.12}$$

where ρ_s is the density of the solvent. For the case where a mixture of solvent and carrier liquid was collected at the outlet, $\Delta m > \Delta m^*$, and the volumetric collection rate of liquid was calculated as:

$$Q_{\text{out}} = Q_{\text{in}} + \frac{\Delta m - \Delta m^*}{\rho_c \Delta t} \tag{6.13}$$

The maximum error in the volumetric collection rate of liquid at the outlet was determined to be $\pm 6\,\mu\text{L/ min}$ on the basis of the 10 mg precision of the balance, a 10 ms uncertainty in the collection time, a 1 % error in the volumetric injection rate of the solvent, and maximum 0.1 % fluctuations in the densities of the carrier liquid and solvent (due to changes in temperature).

6.6.4 Inline extraction

2,6-dichloroindophenol sodium salt hydrate (NaA, 5.5 mg, ≥90 %, Sigma-Aldrich) was dissolved in 100 mL deionized water to produce 0.19 mM (anhydrous basis) solution. HCl (37 %, VWR) was diluted to give a 1 mM solution. Liquids were pumped from gas-tight syringes (Hamilton) using Harvard Pump 11 Plus syringe pumps. NaA (aq.) and HCl (aq.) were injected at 10 µL/min each into a Y-mixer (Upchurch). The outlet of the mixer was con-

nected to a two-in-one-out junction where the aqueous phase was combined with chloroform (99.0–99.6 %, VWR, 10 µL/min) to generate a segmented flow. The segmented flow was passed through 60 cm of PTFE tubing, and into the inlet of a porous capillary separator with a $d = 254$ µm and $l = 5$ cm flow restriction. The chloroform emerging through the walls of the capillary and the aqueous phase emerging from the separator outlet were collected in separate vials. UV-visible absorption spectra were recorded with a Unicam UV 500 spectrometer, using quartz cuvettes (10 mm path length, Lightpath Optical (UK) Ltd).

6.6.5 Scanning electron microscopy

A small piece of porous PTFE capillary was attached to a sample stub using carbon tape, sputtered with 5 nm chromium, and then examined using an FEI Phenom scanning electron microscope.

Bibliography

[1] T. W. Phillips, I. G. Lignos, R. M. Maceiczyk, A. J. deMello and J. C. deMello, *Lab Chip*, 2014, **14**, 3172–3180, DOI: 10.1039/C4LC00429A.

[2] D. V. Talapin, J.-S. Lee, M. V. Kovalenko and E. V. Shevchenko, *Chem. Rev.*, 2010, **110**, 389–458, DOI: 10.1021/cr900137k.

[3] L. L. Chng, N. Erathodiyil and J. Y. Ying, *Acc. Chem. Res.*, 2013, **46**, 1825–1837, DOI: 10.1021/ar300197s.

[4] J. A. Webb and R. Bardhan, *Nanoscale*, 2014, **6**, 2502, DOI: 10.1039/c3nr05112a.

[5] Royal Institution, *Michael Faraday's gold colloids*, `http://www.rigb.org/our-history/iconic-objects/iconic-objects-list/faraday-gold-colloids`, accessed 14th August 2016.

[6] V. K. LaMer and R. H. Dinegar, *J. Am. Chem. Soc.*, 1950, **72**, 4847–4854, DOI: 10.1021/ja01167a001.

[7] V. K. LaMer, *Ind. Eng. Chem.*, 1952, **44**, 1270–1277, DOI: 10.1021/ie50510a027.

[8] H. M. Chen and R.-S. Liu, *J. Phys. Chem. C*, 2011, **115**, 3513–3527.

[9] T. K. Sau and A. L. Rogach, *Adv. Mater.*, 2010, **22**, 1781–1804, DOI: 10.1002/adma.200901271.

[10] X. Peng, *Nano Res.*, 2009, **2**, 425–447, DOI: 10.1007/s12274-009-9047-2.

[11] S. Kumar, M. Jones, S. Lo and G. Scholes, *Small*, 2007, **3**, 1633–1639, DOI: 10.1002/smll.200700155.

[12] J. I. Park, A. Saffari, S. Kumar, A. Günther and E. Kumacheva, *Annu. Rev. Mater. Res.*, 2010, **40**, 415–443, DOI: 10.1146/annurev-matsci-070909-104514.

[13] L. Zhang and Y. Xia, *Adv. Mater.*, 2014, **26**, 2600–2606, DOI: 10.1002/adma.201304897.

[14] R. Ottewill and R. Woodbridge, *J. Colloid. Sci.*, 1961, **16**, 581–594, DOI: 10.1016/0095-8522(61)90045-9.

[15] L. Zhang, Y. Wang, L. Tong and Y. Xia, *Nano Lett.*, 2014, **14**, 4189–4194, DOI: 10.1021/nl501994q.

[16] J. B. Edel, R. Fortt, J. C. deMello and A. J. deMello, *Chem. Commun.*, 2002, 1136–1137, DOI: 10.1039/b202998g.

[17] A. J. deMello, *Nature*, 2006, **442**, 394–402, DOI: 10.1038/nature05062.

[18] E. J. Shaughnessy Jr., I. M. Katz and J. P. Schaffer, *Introduction to Fluid Mechanics*, Oxford University Press, 2005.

[19] N.-T. Nguyen and Z. Wu, *J. Micromech. Microeng.*, 2005, **15**, R1–R16, DOI: 10.1088/0960-1317/15/2/R01.

[20] K. Jähnisch, V. Hessel, H. Löwe and M. Baerns, *Angew. Chem. Int. Ed.*, 2004, **43**, 406–446, DOI: 10.1002/anie.200300577.

[21] L. Ducry and D. M. Roberge, *Angew. Chem.*, 2005, **117**, 8186–8189, DOI: 10.1002/ange.200502387.

[22] J. Pelleter and F. Renaud, *Org. Proc. Res. Dev.*, 2009, **13**, 698–705, DOI: 10.1021/op8002695.

[23] T. Razzaq and C. Kappe, *Chem. Asian J.*, 2010, **5**, 1274–1289, DOI: 10.1002/asia.201000010.

[24] H. Sahoo, J. Kralj and K. Jensen, *Angew. Chem. Int. Ed.*, 2007, **46**, 5704–5708, DOI: 10.1002/anie.200701434.

[25] S. Duraiswamy and S. A. Khan, *Small*, 2009, **5**, 2828–2834, DOI: 10.1002/smll.200901453.

[26] Z. Wan, W. Luan and S.-t. Tu, *J. Phys. Chem. C*, 2011, **115**, 1569–1575, DOI: 10.1021/jp108901z.

[27] A. M. Nightingale, S. H. Krishnadasan, D. Berhanu, X. Niu, C. Drury, R. McIntyre, E. Valsami-Jones and J. C. deMello, *Lab Chip*, 2011, **11**, 1221–1227, DOI: 10.1039/C0LC00507J.

[28] V. Sebastian Cabeza, S. Kuhn, A. A. Kulkarni and K. F. Jensen, *Langmuir*, 2012, **28**, 7007–7013, DOI: 10.1021/la205131e.

[29] Y. H. Kim, L. Zhang, T. Yu, M. Jin, D. Qin and Y. Xia, *Small*, 2013, **9**, 3462–3467, DOI: 10.1002/smll.201203132.

[30] A. M. Nightingale and J. C. de Mello, *J. Mater. Chem.*, 2010, **20**, 8454, DOI: 10.1039/c0jm01221a.

[31] A. M. Nightingale and J. C. deMello, *Adv. Mater.*, 2013, **25**, 1813–1821, DOI: 10.1002/adma.201203252.

[32] B. Zheng and R. F. Ismagilov, *Angew. Chem. Int. Ed.*, 2005, **44**, 2520–2523, DOI: 10.1002/anie.200462857.

[33] D. L. Chen, L. Li, S. Reyes, D. N. Adamson and R. F. Ismagilov, *Langmuir*, 2007, **23**, 2255–2260, DOI: 10.1021/la062152z.

[34] S. Duraiswamy and S. A. Khan, *Nano Lett.*, 2010, **10**, 3757–3763, DOI: 10.1021/nl102478q.

[35] A. M. Nightingale, T. W. Phillips, J. H. Bannock and J. C. de Mello, *Nat. Commun.*, 2014, **5**, 3777, DOI: 10.1038/ncomms4777.

[36] H. Yang, W. Luan, Z. Wan, S.-t. Tu, W.-K. Yuan and Z. M. Wang, *Cryst. Growth Des.*, 2009, **9**, 4807–4813, DOI: 10.1021/cg900652y.

[37] S. Krishnadasan, J. Tovilla, R. Vilar, A. J. deMello and J. C. deMello, *J. Mater. Chem.*, 2004, **14**, 2655, DOI: 10.1039/b401559b.

[38] A. M. L. C. Nightingale, *Ph.D. thesis*, Imperial College London, 2010.

[39] B. K. H. Yen, A. Günther, M. A. Schmidt, K. F. Jensen and M. G. Bawendi, *Angew. Chem. Int. Ed.*, 2005, **44**, 5447–5451, DOI: 10.1002/anie.200500792.

[40] I. Shestopalov, J. D. Tice and R. F. Ismagilov, *Lab Chip*, 2004, **4**, 316, DOI: 10.1039/b403378g.

[41] E. M. Chan, A. P. Alivisatos and R. A. Mathies, *J. Am. Chem. Soc.*, 2005, **127**, 13854–13861, DOI: 10.1021/ja051381p.

[42] K. Kumar, A. M. Nightingale, S. H. Krishnadasan, N. Kamaly, M. Wylenzinska-Arridge, K. Zeissler, W. R. Branford, E. Ware, A. J. deMello and J. C. deMello, *J. Mater. Chem.*, 2012, **22**, 4704, DOI: 10.1039/c2jm30257h.

[43] J. Yue, J. C. Schouten and T. A. Nijhuis, *Ind. Eng. Chem. Res.*, 2012, **51**, 14583–14609, DOI: 10.1021/ie301258j.

[44] S. Krishnadasan, R. J. C. Brown, A. J. deMello and J. C. deMello, *Lab Chip*, 2007, **7**, 1434, DOI: 10.1039/b711412e.

[45] A. Toyota, H. Nakamura, H. Ozono, K. Yamashita, M. Uehara and H. Maeda, *J. Phys. Chem. C*, 2010, **114**, 7527–7534, DOI: 10.1021/jp911876s.

[46] A. M. Nightingale, J. H. Bannock, S. H. Krishnadasan, F. T. F. O'Mahony, S. A. Haque, J. Sloan, C. Drury, R. McIntyre and J. C. deMello, *J. Mater. Chem. A*, 2013, **1**, 4067–4076, DOI: 10.1039/C3TA10458C.

[47] R. D. Chambers, M. A. Fox, D. Holling, T. Nakano, T. Okazoe and G. Sandford, *Lab Chip*, 2005, **5**, 191–198, DOI: 10.1039/B416400H.

[48] H. Yang, W. Luan, S.-t. Tu and Z. M. Wang, *Lab Chip*, 2008, **8**, 451, DOI: 10.1039/b715540a.

[49] E. Y. Erdem, J. C. Cheng, F. M. Doyle and A. P. Pisano, *Small*, 2014, **10**, 1076–1080, DOI: 10.1002/smll.201302379.

[50] S. Marre, J. Park, J. Rempel, J. Guan, M. G. Bawendi and K. F. Jensen, *Adv. Mater.*, 2008, **20**, 4830–4834, DOI: 10.1002/adma.200801579.

[51] Y. Sun, B. Gates, B. Mayers and Y. Xia, *Nano Lett.*, 2002, **2**, 165–168, DOI: 10.1021/nl010093y.

[52] F. Fievet, J. Lagier and M. Figlarz, *MRS Bull.*, 1989, **14**, 29–34, DOI: 10.1557/S0883769400060930.

[53] Y. Sun and Y. Xia, *Adv. Mater.*, 2002, **14**, 833, DOI: 10.1002/1521-4095(20020605)14:11¡833::AID-ADMA833¿3.0.CO;2-K.

[54] Y. Sun, Y. Yin, B. T. Mayers, T. Herricks and Y. Xia, *Chem. Mater*, 2002, **14**, 4736–4745, DOI: 10.1021/cm020587b.

[55] Y. Sun, B. Mayers, T. Herricks and Y. Xia, *Nano Lett.*, 2003, **3**, 955–960, DOI: 10.1021/nl034312m.

[56] C. Hammond, *The Basics of Crystallography and Diffraction*, Oxford University Press, 3rd edn., 2009.

[57] N. M. Rosengaard and H. L. Skriver, *Phys. Rev. B*, 1993, **47**, 12865–12873, DOI: 10.1103/PhysRevB.47.12865.

[58] Y. Xia, Y. Xiong, B. Lim and S. Skrabalak, *Angew. Chem. Int. Ed.*, 2009, **48**, 60–103, DOI: 10.1002/anie.200802248.

[59] Y. Gao, P. Jiang, D. F. Liu, H. J. Yuan, X. Q. Yan, Z. P. Zhou, J. X. Wang, L. Song, L. F. Liu, W. Y. Zhou, G. Wang, C. Y. Wang and S. S. Xie, *Chem. Phys. Lett.*, 2003, **380**, 146–149, DOI: 10.1016/j.cplett.2003.08.074.

[60] B. Wiley, Y. Sun and Y. Xia, *Langmuir*, 2005, **21**, 8077–8080, DOI: 10.1021/la050887i.

[61] B. Wiley, T. Herricks, Y. Sun and Y. Xia, *Nano Lett.*, 2004, **4**, 1733–1739, DOI: 10.1021/nl048912c.

[62] B. A. Sexton and R. J. Madix, *Chem. Phys. Lett.*, 1980, **76**, 294–297, DOI: 10.1016/0009-2614(80)87024-2.

[63] C. T. Campbell, *Surf. Sci.*, 1985, **157**, 43–60, DOI: 10.1016/0039-6028(85)90634-X.

[64] F. B. de Mongeot, A. Cupolillo, U. Valbusa and M. Rocca, *Chem. Phys. Lett.*, 1997, **270**, 345–350, DOI: 10.1016/S0009-2614(97)00381-3.

[65] K. E. Korte, S. E. Skrabalak and Y. Xia, *J. Mater. Chem.*, 2008, **18**, 437–441, DOI: 10.1039/B714072J.

[66] C. Yang, H. Gu, W. Lin, M. M. Yuen, C. P. Wong, M. Xiong and B. Gao, *Adv. Mater.*, 2011, **23**, 3052–3056, DOI: 10.1002/adma.201100530.

[67] C. Jia, P. Yang and A. Zhang, *Mater. Chem. Phys.*, 2014, **143**, 794–800, DOI: 10.1016/j.matchemphys.2013.10.015.

[68] S. Coskun, B. Aksoy and H. E. Unalan, *Cryst. Growth Des.*, 2011, **11**, 4963–4969, DOI: 10.1021/cg200874g.

[69] J. Jiu, T. Araki, J. Wang, M. Nogi, T. Sugahara, S. Nagao, H. Koga, K. Suganuma, E. Nakazawa, M. Hara, H. Uchida and K. Shinozaki, *J. Mater. Chem. A*, 2014, **2**, 6326–6330, DOI: 10.1039/C4TA00502C.

[70] L. Gou, M. Chipara and J. M. Zaleski, *Chem. Mater*, 2007, **19**, 1755–1760, DOI: 10.1021/cm070160a.

[71] W. M. Schuette and W. E. Buhro, *ACS Nano*, 2013, **7**, 3844–3853, DOI: 10.1021/nn400414h.

[72] W. M. Schuette and W. E. Buhro, *Chem. Mater*, 2014, **26**, 6410–6417, DOI: 10.1021/cm502827b.

[73] J. H. Lee, P. Lee, D. Lee, S. S. Lee and S. H. Ko, *Cryst. Growth Des.*, 2012, **12**, 5598–5605, DOI: 10.1021/cg301119d.

[74] S. M. Bergin, Y.-H. Chen, A. R. Rathmell, P. Charbonneau, Z.-Y. Li and B. J. Wiley, *Nanoscale*, 2012, **4**, 1996–2004, DOI: 10.1039/C2NR30126A.

[75] G.-H. Lim, S. J. Lee, I. Han, S. Bok, J. H. Lee, J. Nam, J. H. Cho and B. Lim, *Chem. Phys. Lett.*, 2014, **602**, 10–15, DOI: 10.1016/j.cplett.2014.04.012.

[76] B. Li, S. Ye, I. E. Stewart, S. Alvarez and B. J. Wiley, *Nano Lett.*, 2015, **15**, 6722–6726, DOI: 10.1021/acs.nanolett.5b02582.

[77] R. Gottesman, A. Tangy, I. Oussadon and D. Zitoun, *New J. Chem.*, 2012, **36**, 2456–2459, DOI: 10.1039/C2NJ40763A.

[78] K.-S. Chou, C.-Y. Hsu and B.-T. Liu, *RSC Adv.*, 2015, **5**, 29872–29877, DOI: 10.1039/C5RA00320B.

[79] S. E. Skrabalak, B. J. Wiley, M. Kim, E. V. Formo and Y. Xia, *Nano Lett.*, 2008, **8**, 2077–2081, DOI: 10.1021/nl800910d.

[80] R. A. Basson and T. A. d. Plessis, *Analyst*, 1967, **92**, 463–465, DOI: 10.1039/AN9679200463.

[81] A. Tao, P. Sinsermsuksakul and P. Yang, *Angew. Chem. Int. Ed.*, 2006, **45**, 4597–4601, DOI: 10.1002/anie.200601277.

[82] K. C. Pradel, K. Sohn and J. Huang, *Angew. Chem. Int. Ed.*, 2011, **50**, 3412–3416, DOI: 10.1002/anie.201100087.

[83] Y. Xiong, I. Washio, J. Chen, H. Cai, Z.-Y. Li and Y. Xia, *Langmuir*, 2006, **22**, 8563–8570, DOI: 10.1021/la061323x.

[84] J. C. Miller and J. N. Miller, *Analyst*, 1988, **113**, 1351–1356.

[86] D. C. Montgomery, *Introduction to Statistical Quality Control*, Wiley, 5th edn., 2005.

[87] D. Bohne, S. Fischer and E. Obermeier, *Berichte der Bunsengesellschaft für physikalische Chemie*, 1984, **88**, 739–742, DOI: 10.1002/bbpc.19840880813.

[88] H. E. Gottlieb, V. Kotlyar and A. Nudelman, *J. Org. Chem.*, 1997, **62**, 7512–7515, DOI: 10.1021/jo971176v.

[89] J. H. Bannock, S. H. Krishnadasan, A. M. Nightingale, C. P. Yau, K. Khaw, D. Burkitt, J. J. M. Halls, M. Heeney and J. C. de Mello, *Adv. Funct. Mater.*, 2013, **23**, 2123–2129, DOI: 10.1002/adfm.201203014.

[90] G. James, D. Witten, T. Hastie and R. Tibshirani, *An Introduction to Statistical Learning*, Springer, 2013.

[91] Y. Ran, W. He, K. Wang, S. Ji and C. Ye, *Chem. Commun.*, 2014, **50**, 14877–14880, DOI: 10.1039/C4CC04698F.

[92] W. H. Binder, *Angew. Chem. Int. Ed.*, 2005, **44**, 5172–5175, DOI: 10.1002/anie.200501220.

[93] T. W. Phillips, J. H. Bannock and J. C. deMello, *Lab Chip*, 2015, **15**, 2960–2967, DOI: 10.1039/C5LC00430F.

[94] T. W. Phillips, J. H. Bannock and J. C. de Mello, *Figshare*, 2015, DOI: 10.6084/m9.figshare.1447208.

[95] J. F. B. Hall, X. Han, M. Poliakoff, R. A. Bourne and M. W. George, *Chem. Commun.*, 2012, **48**, 3073–3075, DOI: 10.1039/C2CC17429D.

[96] M. O'Brien, P. Koos, D. L. Browne and S. V. Ley, *Org. Biomol. Chem.*, 2012, **10**, 7031–7036, DOI: 10.1039/C2OB25912E.

[97] D. X. Hu, M. O'Brien and S. V. Ley, *Org. Lett.*, 2012, **14**, 4246–4249, DOI: 10.1021/ol301930h.

[98] S. L. Bourne, M. O'Brien, S. Kasinathan, P. Koos, P. Tolstoy, D. X. Hu, R. W. Bates, B. Martin, B. Schenkel and S. V. Ley, *ChemCatChem*, 2013, **5**, 159–172, DOI: 10.1002/cctc.201200778.

[99] M. N. Kashid, Y. M. Harshe and D. W. Agar, *Ind. Eng. Chem. Res.*, 2007, **46**, 8420–8430, DOI: 10.1021/ie070077x.

[100] E. Kolehmainen and I. Turunen, *Chem. Eng. Process.*, 2007, **46**, 834–839, DOI: 10.1016/j.cep.2007.05.027.

[101] F. Scheiff, M. Mendorf, D. Agar, N. Reis and M. Mackley, *Lab Chip*, 2011, **11**, 1022, DOI: 10.1039/c0lc00442a.

[102] W. Gaakeer, M. de Croon, J. van der Schaaf and J. Schouten, *Chem. Eng. J.*, 2012, **207-208**, 440–444, DOI: 10.1016/j.cej.2012.06.148.

[103] O. K. Castell, C. J. Allender and D. A. Barrow, *Lab Chip*, 2009, **9**, 388–396, DOI: 10.1039/B806946H.

[104] M. Mendorf, H. Nachtrodt, A. Mescher, A. Ghaini and D. W. Agar, *Ind. Eng. Chem. Res.*, 2010, **49**, 10908–10916, DOI: 10.1021/ie100473d.

[105] L. Nord and B. Karlberg, *Anal. Chim. Acta*, 1980, **118**, 285–292, DOI: 10.1016/S0003-2670(01)93604-9.

[106] R. H. Atallah, J. Ruzicka and G. D. Christian, *Anal. Chem.*, 1987, **59**, 2909–2914.

[107] Chemical Heritage Foundation, *Scientists You Must Know: Robert Gore*, `https://vimeo.com/103516807`, accessed 14th August 2016.

[108] D. R. Snead and T. F. Jamison, *Chem. Sci.*, 2013, **4**, 2822, DOI: 10.1039/c3sc50859e.

[109] R. A. Maurya, K.-I. Min and D.-P. Kim, *Green Chem.*, 2014, **16**, 116–120, DOI: 10.1039/C3GC41226A.

[110] J. G. Kralj, H. R. Sahoo and K. F. Jensen, *Lab Chip*, 2007, **7**, 256–263, DOI: 10.1039/B610888A.

[111] P. Li, J. S. Moore and K. F. Jensen, *ChemCatChem*, 2013, **5**, 1729–1733, DOI: 10.1002/cctc.201300054.

[112] A. Adamo, P. L. Heider, N. Weeranoppanant and K. F. Jensen, *Ind. Eng. Chem. Res.*, 2013, **52**, 10802–10808, DOI: 10.1021/ie401180t.

[113] Zaiput Flow Technologies, *Liquid-Liquid Separators*, `https://www.zaiput.com/liquid-liquid-separators`, accessed 14th August 2016.

[114] Syrris Ltd, *Asia FLLEX*, `http://syrris.com/flow-products/asia-modules/asia-fllex`, accessed 14th August 2016.

[115] J. H. Bannock, T. W. Phillips, A. M. Nightingale and J. C. deMello, *Anal. Methods*, 2013, **5**, 4991–4998, DOI: 10.1039/C3AY41251B.

[116] R. M. Barnes and X. Wang, *J. Anal. At. Spectrom.*, 1988, **3**, 1083–1089, DOI: 10.1039/JA9880301083.

[117] X. Wang, M. Viczian, A. Lasztity and R. M. Barnes, *J. Anal. At. Spectrom.*, 1988, **3**, 821–827, DOI: 10.1039/JA9880300821.

[118] M. Yamamoto, Y. Obata, Y. Nitta, F. Nakata and T. Kumamaru, *J. Anal. At. Spectrom.*, 1988, **3**, 441–445, DOI: 10.1039/JA9880300441.

[119] J. H. Bannock, M. Al-Hashimi, S. H. Krishnadasan, J. J. M. Halls, M. Heeney and J. C. de Mello, *Mater. Horiz.*, 2014, **1**, 214–218, DOI: 10.1039/C3MH00066D.

[120] J. M. Armstrong, *Biochim. Biophys. Acta*, 1964, **86**, 194–197, DOI: 10.1016/0304-4165(64)90180-1.

Appendix A

Silver nanowires

A.1 Box and whisker plots

Box and whisker plots are used throughout this work. They are a convenient method for visualising the distribution of numerical values for multiple sets of data. Figure A.1 shows the probability density function for a normal distribution with mean $\mu = 1$ and standard deviation $\sigma = 1$ (red line). It also shows a histogram and box and whisker plot of 35 values randomly drawn from the distribution. The "box" extends from the first quartile to the third quartile. Its width is equal to the interquartile range (IQR), which is a measure of the variability or spread of the values. The line across the box indicates the median. The "whiskers" are the lines that extend from the box. There is no convention for the values to which the whiskers extend, but in this work they extend to $\mathrm{Q1} - 1.5 \times \mathrm{IQR}$ and $\mathrm{Q3} + 1.5 \times \mathrm{IQR}$. Values that exceed the whiskers are marked as outliers by a + symbol.

Box and whisker plots make no assumptions about the underlying distribution. In contrast, the appearance of a histogram can be heavily influenced by the choice of the number of bins and bin width.

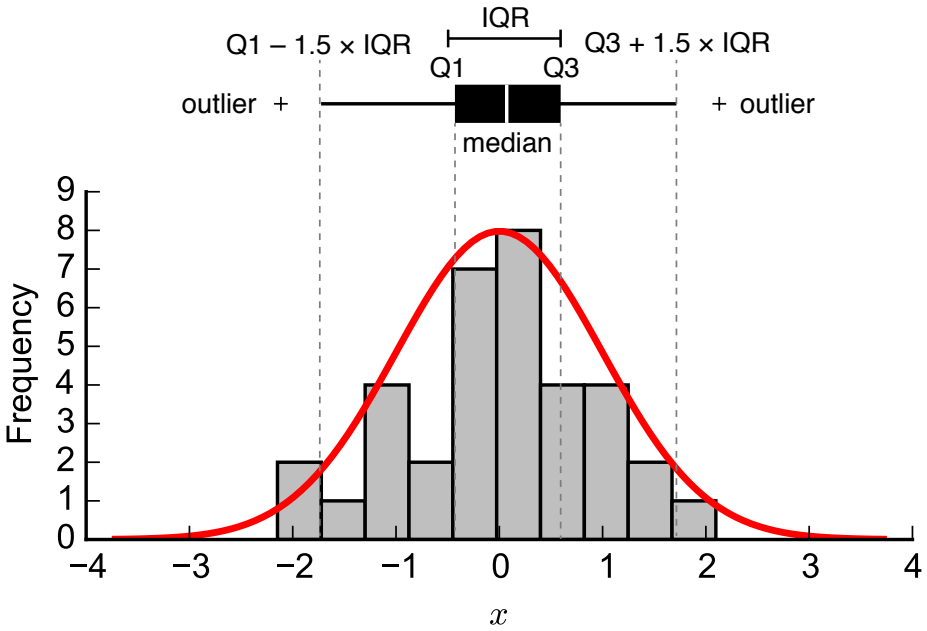


Figure A.1 – Plot showing the probability density function for a normal distribution with mean $\mu = 0$ and standard deviation $\sigma = 0$ (red). The histogram shows the frequency of 35 randomly sampled values $x \sim N(0, 1)$. The same values are plotted as a box and whisker plot above the histogram. Q1 and Q3 denote the first and third quartile.

A.2 Certificates of analysis for ethylene glycol

Supplier lot numbers BCBN5970V and BCBN592V correspond to lot A and B, respectively.

SIGMA-ALDRICH®

3050 Spruce Street, Saint Louis, MO 63103 USA
Email USA: techserv@sial.com Outside USA: eurtechserv@sial.com

Certificate of Analysis

Product Name:	ETHYLENE GLYCOL puriss. p.a., Reag. Ph. Eur.
Product Number:	03750
Batch Number:	BCBN5970V
Brand:	Fluka
CAS Number:	107-21-1
Formula:	$HOCH_2CH_2OH$
Formula Weight:	62.07
Quality Release Date:	20 AUG 2014
Recommended Retest Date:	JAN 2018

TEST	SPECIFICATION	RESULT
APPEARANCE (COLOR)	COLORLESS	COLORLESS
APPEARANCE (FORM)	CLEAR TO CLEAR VISCOUS LIQUID	CLEAR VISCOUS LIQUID
COLOR (IN APHA)	≤ 25 APHA	5 APHA
FREE CARBOXYLIC ACID (T)	≤ 0.001 % (AS CH3COOH)	0.0010 % (AS CH3COOH)
PURITY (GC AREA %)	≥ 99.5 %	100.0 %
REFRACTIVE INDEX N20/D	1.430 - 1.432	1.432
WATER (COULOMETR.)	≤ 0.1 %	0.025 %
SULFATED ASH	≤ 0.005 %	0.003 %
INFRARED SPECTRUM	CONFORMS TO STRUCTURE	CONFORMS
MISCELLANEOUS TESTS	KMNO4 RED.MATTER (AS O) ≤ 0.0003 %	KMNO4 RED.MATTER (AS O) < 0.0003 %
TRACES FORMALDEHYDE (AS HCHO)	≤ 50 MG/KG	< 50 MG/KG
METAL TRACE ANALYSIS (ICP)	CORRESPONDS TO REQUIREMENTS	PASSED
ALUMINIUM (ICP)	≤ 0.5 MG/KG	< 0.5 MG/KG
BARIUM (ICP)	≤ 0.1 MG/KG	< 0.1 MG/KG
BISMUTH (ICP)	≤ 0.1 MG/KG	< 0.1 MG/KG
CALCIUM (ICP)	≤ 0.5 MG/KG	< 0.5 MG/KG
CADMIUM (ICP)	≤ 0.05 MG/KG	< 0.05 MG/KG
COBALT (ICP)	≤ 0.02 MG/KG	< 0.02 MG/KG
CHROMIUM (ICP)	≤ 0.02 MG/KG	< 0.02 MG/KG
COPPER (ICP)	≤ 0.02 MG/KG	< 0.02 MG/KG
IRON (ICP)	≤ 0.2 MG/KG	< 0.2 MG/KG
POTASSIUM (ICP)	≤ 0.5 MG/KG	< 0.5 MG/KG
LITHIUM (ICP)	≤ 0.1 MG/KG	< 0.1 MG/KG

SIGMA-ALDRICH®

3050 Spruce Street, Saint Louis, MO 63103 USA
Email USA: techserv@sial.com Outside USA: eurtechserv@sial.com

Certificate of Analysis

MAGNESIUM (ICP)	≤ 0.1 MG/KG	< 0.1 MG/KG
MANGANESE (ICP)	≤ 0.05 MG/KG	< 0.05 MG/KG
MOLYBDENUM (ICP)	≤ 0.1 MG/KG	< 0.1 MG/KG
SODIUM (ICP)	≤ 1 MG/KG	< 1 MG/KG
NICKEL (ICP)	≤ 0.02 MG/KG	< 0.02 MG/KG
LEAD (ICP)	≤ 0.1 MG/KG	< 0.1 MG/KG
STRONTIUM (ICP)	≤ 0.1 MG/KG	< 0.1 MG/KG
ZINC (ICP)	≤ 0.2 MG/KG	< 0.2 MG/KG
SULFATE (SO4)	≤ 10 MG/KG	< 10 MG/KG
ION CHROMATOGRAPHY (CHLORIDE)	≤ 0.2 MG/KG	< 0.2 MG/KG



Dr. Claudia Geitner
Manager Quality Control
Buchs, Switzerland

Sigma-Aldrich warrants that at the time of the quality release or subsequent retest date this product conformed to the information contained in this publication. The current specification sheet may be available at Sigma-Aldrich.com. For further inquiries, please contact Technical Service. Purchaser must determine the suitability of the product for its particular use. See reverse side of invoice or packing slip for additional terms and conditions of sale.

SIGMA-ALDRICH®

3050 Spruce Street, Saint Louis, MO 63103 USA
Email USA: techserv@sial.com Outside USA: eurtechserv@sial.com

Certificate of Analysis

Product Name:	ETHYLENE GLYCOL puriss. p.a., Reag. Ph. Eur.
Product Number:	03750
Batch Number:	BCBN2592V
Brand:	Fluka
CAS Number:	107-21-1
Formula:	$HOCH_2CH_2OH$
Formula Weight:	62.07
Quality Release Date:	18 JUN 2014
Recommended Retest Date:	NOV 2017

TEST	SPECIFICATION	RESULT
APPEARANCE (COLOR)	COLORLESS	COLORLESS
APPEARANCE (FORM)	CLEAR TO CLEAR VISCOUS LIQUID	CLEAR VISCOUS LIQUID
COLOR (IN APHA)	≤ 25 APHA	5 APHA
FREE CARBOXYLIC ACID (T)	≤ 0.001 % (AS CH3COOH)	0.00090 % (AS CH3COOH)
PURITY (GC AREA %)	≥ 99.5 %	99.9 %
REFRACTIVE INDEX N20/D	1.430 - 1.432	1.432
WATER (COULOMETR.)	≤ 0.1 %	0.041 %
SULFATED ASH	≤ 0.005 %	0.003 %
INFRARED SPECTRUM	CONFORMS TO STRUCTURE	CONFORMS
MISCELLANEOUS TESTS	KMNO4 RED.MATTER (AS O) ≤ 0.0003 %	KMNO4 RED.MATTER (AS O) < 0.0003 %
TRACES FORMALDEHYDE (AS HCHO)	≤ 50 MG/KG	< 50 MG/KG
METAL TRACE ANALYSIS (ICP)	CORRESPONDS TO REQUIREMENTS	PASSED
ALUMINIUM (ICP)	≤ 0.5 MG/KG	< 0.5 MG/KG
BARIUM (ICP)	≤ 0.1 MG/KG	< 0.1 MG/KG
BISMUTH (ICP)	≤ 0.1 MG/KG	< 0.1 MG/KG
CALCIUM (ICP)	≤ 0.5 MG/KG	< 0.5 MG/KG
CADMIUM (ICP)	≤ 0.05 MG/KG	< 0.05 MG/KG
COBALT (ICP)	≤ 0.02 MG/KG	< 0.02 MG/KG
CHROMIUM (ICP)	≤ 0.02 MG/KG	< 0.02 MG/KG
COPPER (ICP)	≤ 0.02 MG/KG	< 0.02 MG/KG
IRON (ICP)	≤ 0.2 MG/KG	< 0.2 MG/KG
POTASSIUM (ICP)	≤ 0.5 MG/KG	< 0.5 MG/KG
LITHIUM (ICP)	≤ 0.1 MG/KG	< 0.1 MG/KG

3050 Spruce Street, Saint Louis, MO 63103 USA
Email USA: techserv@sial.com Outside USA: eurtechserv@sial.com

Certificate of Analysis

MAGNESIUM (ICP)	≤ 0.1 MG/KG	< 0.1 MG/KG
MANGANESE (ICP)	≤ 0.05 MG/KG	< 0.05 MG/KG
MOLYBDENUM (ICP)	≤ 0.1 MG/KG	< 0.1 MG/KG
SODIUM (ICP)	≤ 1 MG/KG	< 1 MG/KG
NICKEL (ICP)	≤ 0.02 MG/KG	< 0.02 MG/KG
LEAD (ICP)	≤ 0.1 MG/KG	< 0.1 MG/KG
STRONTIUM (ICP)	≤ 0.1 MG/KG	< 0.1 MG/KG
ZINC (ICP)	≤ 0.2 MG/KG	< 0.2 MG/KG
SULFATE (SO4)	≤ 10 MG/KG	< 10 MG/KG
ION CHROMATOGRAPHY (CHLORIDE)	≤ 0.2 MG/KG	< 0.2 MG/KG



Dr. Claudia Geitner
Manager Quality Control
Buchs, Switzerland

Sigma-Aldrich warrants that at the time of the quality release or subsequent retest date this product conformed to the information contained in this publication. The current specification sheet may be available at Sigma-Aldrich.com. For further inquiries, please contact Technical Service. Purchaser must determine the suitability of the product for its particular use. See reverse side of invoice or packing slip for additional terms and conditions of sale.

A.3 COSY NMR

Figure A.2 shows the COSY spectra for EG lot A and lot B. The peaks on the diagonal correspond to the peaks in a one-dimensional NMR spectrum. The cross peaks, located off of the diagonal and highlighted with a dashed line, indicate that the proton environments giving rise to the multiplets at 4.46 ppm and 3.94 ppm, labelled **a** and **b** respectively, are coupled to one another. Therefore both of these environments are in the same molecule, and within a distance of three or fewer bonds. There is also an additional cross peak that was not visible in the one-dimensional NMR spectrum, at 7.75 ppm in (a) and 7.49 ppm in (b), which was unassigned.

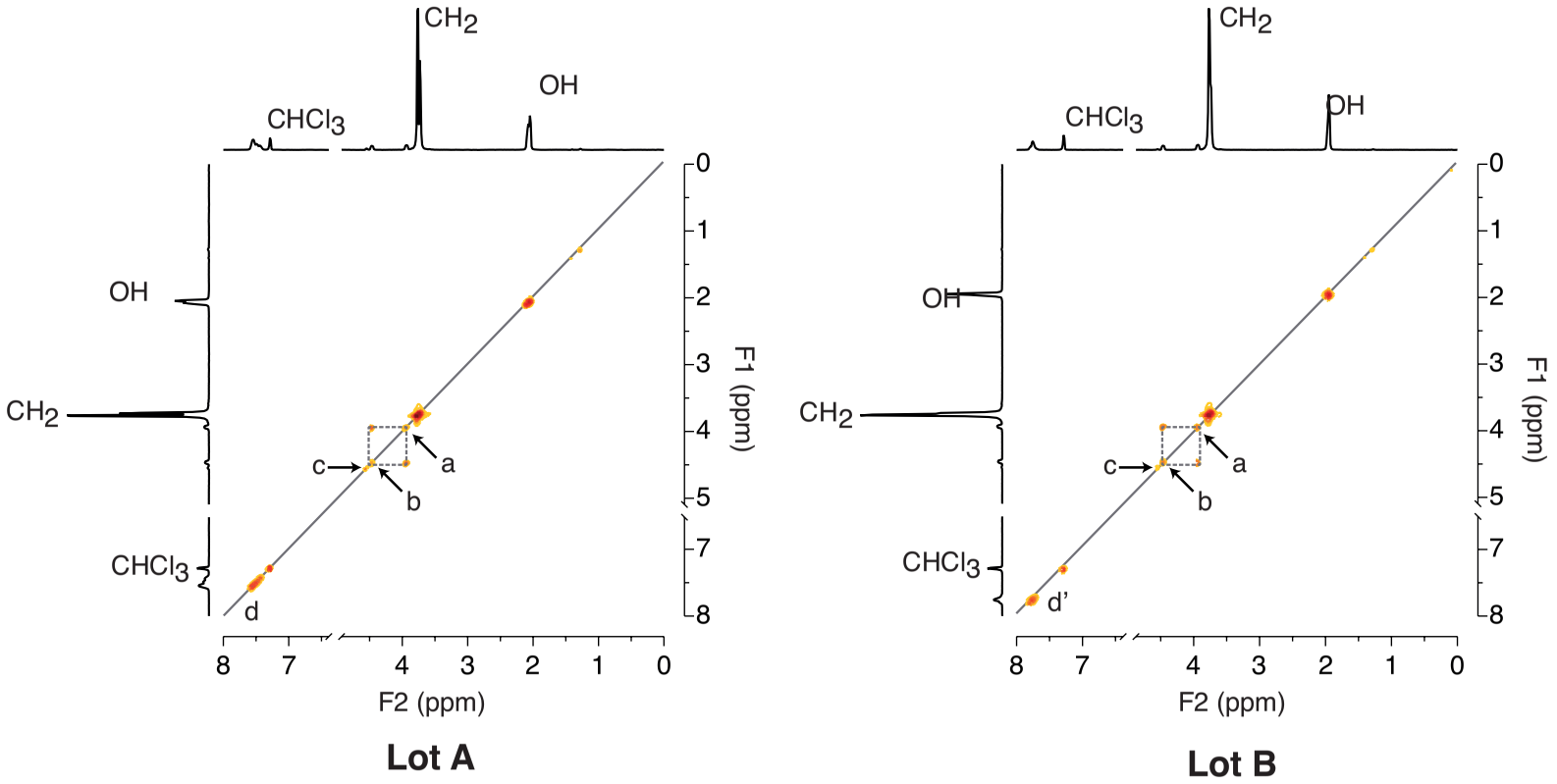


Figure A.2 – COSY NMR spectra of EG from (left) lot A and (right) lot B.

Appendix B

Reproduction permissions

Permission was obtained to reproduce all third party copyrighted works in this thesis. Copies of all permission documents can be downloaded from https://dx.doi.org/10.6084/m9.figshare.3840192.